ROBOTIC-ASSISTED
BEATING HEART SURGERY

by

ÖZKAN BEBEK

Submitted in partial fulfillment of the requirements

for the degree of Doctor of Philosophy

Dissertation Advisor: M. Cenk Çavuşoğlu, Ph.D.

Department of Electrical Engineering and Computer Science

CASE WESTERN RESERVE UNIVERSITY

May 18, 2008

CASE WESTERN RESERVE UNIVERSITY

SCHOOL OF GRADUATE STUDIES

We hereby approve the thesis/dissertation of

Özkan Bebek

candidate for the Doctor of Philosophy degree *.

(signed) M. Cenk Çavuşoğlu
(chair of the committee)

Wyatt Newman

Wei Lin

Kenneth A. Loparo

Roger Quinn

(date) January 23, 2008

*We also certify that written approval has been obtained for any proprietary material contained therein.

To my family

Contents

List of Tables

List of Figures

List of Symbols

y	Output vector	36
y_{err}	Offset error between the past cycle and current cycle	25
y_{est}	Estimate output vector	25
y_{hrt}	Measured heart motion	25
$y_{hrt,pr}$	Measured heart motion of the previous cycle	25
y_i	Cartesian coordinate of i	78
$\mathbf{A}$	State Matrix	109
$\mathbf{B}$	Input Matrix	109
$\mathbf{C}$	Output Matrix	109
$\mathbf{C}_p$	PHANToM Coriolis Matrix	51
E	Young's modulus	71
$\mathbf{F}$	Auxiliary System State Matrix	36
$\mathbf{G}$	Auxiliary System Output Matrix	36
GF	Gauge Factor	69
$\mathbf{H}$	Output Matrix	36
$\mathbf{H}_i$	Covariance Matrix of x_i	129
$\mathbf{I}$	Identity Matrix	36
I	Second moment of the cross sectional area	71
$\mathbf{J}_i$	Jacobian Matrix	125
J	Performance index	37
J^*	Optimal performance index	37
$\mathbf{K}$	Optimal Gain Matrix	39
$\mathbf{L}$	Pseudoinverse of Output Matrix	37
$\mathbf{L}_p$	Feedback Gain Matrix	108
L	Beam length	71
$\mathbf{M}$	Parameter Matrix	44
M	Bending Moment	71

List of Abbreviations

ARMC	Active Relative Motion Canceling
CABG	Coronary artery bypass graft
CAD	Coronary artery disease
CDC	Centers for Disease Control and Prevention
CHD	Coronary heart disease
CPB	Cardiopulmonary bypass
DAC	Data Acquisition and Control
DAQ	Data Acquisition
DOF	Degree(s) of freedom
DVRT	Differential Variable Reluctance Transducer
ECG	Electrocardiogram
FEA	Finite Element Analysis
FEM	Finite Element Model
LAD	Left Anterior Descending Artery
LVDT	Linear Variable Displacement Transducer
MIDCAB	Minimally invasive direct visualization coronary artery bypass
MPC	Model Predictive Control
OPCABG	Off-pump Coronary Artery Bypass Graft Surgery
PD	Position-plus-Derivative
PortCAB	Port-access coronary artery bypass

PP	Pole Placement
POI	Point of Interest
PSD	Power Spectral Density
RHMPC	Receding Horizon Model Predictive Control
RMS	Root Mean Square

Acknowledgements

I am indebted to my advisor Cenk Çavuşoğlu for letting me involved in this research in the first place; and very thankful for his guidance and support through the years. I appreciate his considerate, encouraging, and understanding personality as a mentor, who set realistic goals that always kept me motivated for this research. He always gave positive feedback and had a good sense of humor while dealing with disappointments or unforeseen circumstances. I am thankful for his encouragement and help which enabled me to complete this dissertation.

I am also grateful to the other members of my committee, Wyatt Newman, Wei Lin, Kenneth Loparo and Roger Quinn. As individuals, they offered encouragement and constructive criticism for this dissertation to take its current shape.

I would like to thank my labmates for their friendship and for sharing days and nights with me in the research lab although we worked in a windowless existence and could not tell the time. Also many thanks to those who gave me the possibility to complete this dissertation.

I am grateful to my parents for their support throughout my long education life.

Especially, I would like to give my sincere thanks to my wife Ebru whose patience and love enabled me to complete this work.

This research was done in the Medical Robotics and Computer Integrated Surgery

Laboratory at Case Western Reserve University; with partial support by the National Science Foundation Grants CISE IIS-0222743, EIA-0329811, and CNS-0423253, and by the Department of Commerce grant TOP-39-60-04003.

Robotic-Assisted Beating Heart Surgery

Abstract

by

ÖZKAN BEBEK

Coronary heart disease is a leading cause of death in the USA. A promising treatment option for this disease is off-pump coronary artery bypass graft (CABG) surgery as the artery grafting is done without stopping the heart. In the robotic assisted-surgery concept the surgeon views the surgical scene on a video display and operates on the heart as if it were stationary while the robotic system actively compensates for the motion of the heart. With the proposed system concept, the CABG surgery will be possible without using passive stabilizers, and the hospitalization time and cost of the operation will be decreased.

In this dissertation intelligent robotic tools for assisting off-pump (beating heart) CABG surgery are presented. Most important aspects of such a robotic system are accurately measuring and predicting the heart motion as they are instrumental in canceling the relative motion between the heart surface and surgical tools attached to the robotic manipulators. The proposed control algorithm contributes to the field by using biological signals in the estimation of heart's future motion for active relative motion canceling. Also a novel contact position sensor is developed to measure the position of the beating heart and a preliminary noise characterization for the future sensor system implementation is presented.

Chapter 1

Introduction

Improving the treatment for coronary heart disease (CHD) should be a priority in terms of developing relevant treatment options as the statistics of the Centers for Disease Control and Prevention (CDC) indicate heart disease as a leading cause of death [1, Table 7]. In the medical field, intelligent robotic tools reshape the surgical procedures by providing shorter operation times and lower costs. This technology also promises an enhanced way of performing off-pump coronary artery bypass graft (CABG) surgery. In the robotic-assisted off-pump CABG surgery, the surgeon operates on the beating heart using intelligent robotic instruments. Robotic tools actively cancel the relative motion between the surgical instruments and the point of interest (POI) on the beating heart, dynamically stabilizing the heart for the operation. This algorithm is called Active Relative Motion Canceling (ARMC).

Although off-pump CABG surgery is in a nascent stage and only applicable to limited cases, it is preferred over on-pump CABG surgery because of the significant complications resulting from the use of cardio-pulmonary bypass machine, which include long term cognitive loss [2], and increased hospitalization time and cost [3]. On the other hand off-pump grafting technology is crude and only applicable to a small portion of the cases because of the technological limitations: inadequacy with all but the largest diameter target vessels, ineffectiveness with the coronary arteries on the side and the back of the heart, and its limitation to small number of bypasses. Off-pump procedures represent only 15-20% of all CABG surgeries, at best [4]. Manual tracking of the complex heartbeat motion cannot be achieved by a human without phase and amplitude errors [5]. Use of robotics technology will overcome limitations as it promises an alternative and superior way of performing off-pump CABG surgery.

In this study, it is aimed to develop telerobotic tools to actively track and cancel the relative motion between the surgical instruments and the heart by Active Relative Motion Canceling (ARMC) algorithms, which will allow CABG surgeries to be performed on a stabilized view of the beating heart with the technical convenience of on-pump procedures.

Towards this direction, electrocardiogram (ECG) is utilized as a biological signal in the estimation of the heart motion for an effective motion canceling in the model-based intelligent ARMC algorithm.

1.1 System Concept for Robotic Telesurgical System for Off-Pump CABG Surgery

Robotic-assisted surgery concept replaces conventional surgical tools with robotic instruments which are under direct control of the surgeon through teleoperation, as shown in Figure 1.1. The surgeon views the surgical scene on a video display with images provided by a camera mounted on a robotic arm that follows the heart motion, showing a stabilized view. The robotic surgical instruments also track the heart motion, canceling the relative motion between the surgical site on the heart and the surgical instruments. As a result, the surgeon operates on the heart as if it were stationary, while the robotic system actively compensates for the relative motion of the heart. This is in contrast to traditional off-pump CABG surgery where the

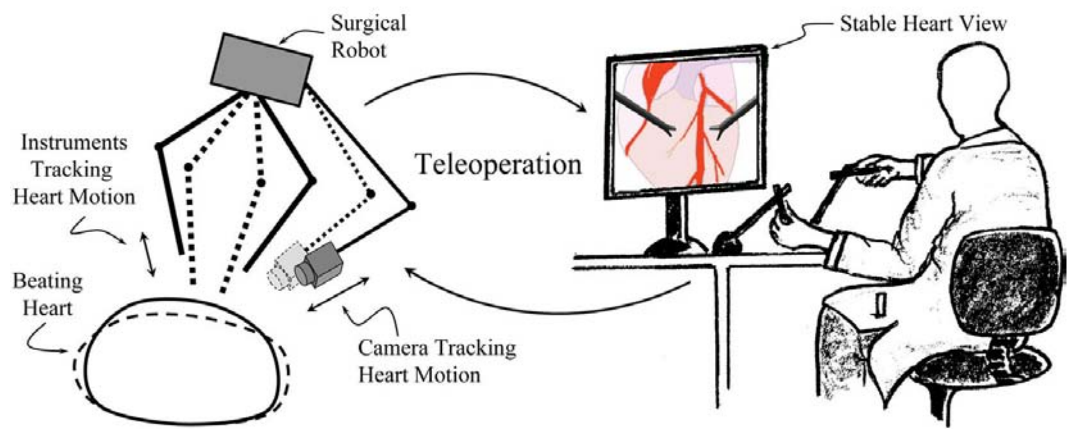

Figure 1.1: System concept for Robotic Telesurgical System for Off-Pump CABG Surgery with Active Relative Motion Canceling (ARMC). Left: Surgical instruments and camera mounted on a robot actively tracking heart motion. Right: Surgeon operating on a stabilized view of the heart, and teleoperatively controlling robotic surgical instruments to perform the surgery.

heart is passively constrained to dampen the beating motion. The proposed control algorithm is called "Active Relative Motion Canceling (ARMC)" to emphasize this difference. Since this method does not rely on passively constraining the heart, it is possible to operate on the side and back surfaces of the heart as well as the front surface using millimeter scale robotic manipulators that can fit into spaces the surgeon cannot reach.

1.2 Coronary Heart Disease

Coronary heart disease (CHD) [*or* coronary artery disease (CAD)] occurs when the arteries that supply blood to the heart muscle (the coronary arteries) become hardened and narrowed due to plaque buildup on their inner walls [6]. As the plaque increases in size, the insides of the coronary arteries get narrower and less blood can flow through them. Eventually, blood flow to the heart muscle is reduced, and, because blood carries much-needed oxygen, the heart muscle is not able to receive the amount of oxygen it needs. Reduced or cutoff blood flow and oxygen supply to the heart muscle can result in an angina or even a heart attack.

Angina is chest pain or discomfort that occurs when the heart does not get enough blood. However if there is no blockage, enough blood eventually flow to recover making the pain mild and temporary. A heart attack, on the other hand, happens when a blood clot develops at the site of plaque in a coronary artery and suddenly cuts off most or all blood supply to that part of the heart muscle. Cells in the heart muscle begin to die if they do not receive enough oxygen-rich blood. This can cause permanent damage to the heart muscle. Over time, CHD can weaken the heart muscle and contribute to arrhythmias (changes in the normal beating rhythm) and even heart failure. Heart failure does not mean that the heart has stopped or is about to stop. Instead, it means that the heart is failing to pump blood the way that it should.

About 13 million people in the United States have CHD. It is the leading cause of death in both men and women. Each year, more than half a million Americans die from CHD. In United States, estimated direct cost[1] of coronary heart disease in 2007 is 164.9 Billion Dollars [7].

Treatment for CHD may include lifestyle changes, medicines, and special procedures like angioplasty and coronary artery bypass surgery. The goals of treatment are to relieve symptoms, slow or stop plaque buildup by controlling or reducing the risk factors, lower the risk of having blood clots form, which can cause a heart attack, and widen or bypass clogged arteries.

Angioplasty opens blocked or narrowed coronary arteries. It can improve blood flow to the heart, relieve chest pain, and possibly prevent a heart attack. Sometimes a device called a stent is placed in the artery to keep the artery propped open after the procedure.

In CABG surgery, arteries or veins from other areas in the body are used to bypass

[1] Cost of hospitals, nursing homes, physicians and other professions, drugs, and medical durables.

the narrowed coronary arteries. Bypass surgery can improve blood flow to the heart, relieve chest pain, and possibly prevent a heart attack.

1.3 Medical Approaches to Coronary Artery Bypass Graft Surgery

Coronary artery bypass graft surgery (CABG) reroutes, or bypasses, blood around clogged arteries to improve blood flow and oxygen to the heart.

The arteries that bring blood to the heart muscle (coronary arteries) can become clogged by plaque (a buildup of fat, cholesterol and other substances). This can slow or stop blood flow through the heart's blood vessels, leading to chest pain or a heart attack. Increasing blood flow to the heart muscle can relieve chest pain and reduce the risk of heart attack.

In CABG surgery, surgeons take a segment of a healthy blood vessel from another part of the body and make a detour around the blocked part of the coronary artery. After the surgery, full recovery may take a few months or more.

Open Chest On-pump Coronary Artery Bypass Graft Surgery

Open-heart surgery (Figure 1.2) is done while the bloodstream is diverted through a pump oxygenator (heart-lung machine). In most coronary bypass graft operations, cardiopulmonary bypass (CPB) with a heart-lung machine is used. This means that besides the surgeon, a cardiac anesthesiologist, a surgical nurse, and a competent perfusionist (blood flow specialist) are required.

CPB has some deleterious effects that are primarily related to a systemic inflammatory response, which results when blood comes into contact with the surface of the extracorporeal circuit of the heart-lung machine [9].

In 2004, 646,000 open-heart procedures were performed in the United States.

Figure 1.2: Open chest on-pump coronary artery bypass graft surgery. Close-up shot of the patient's heart and chest cavity. In this shot one can see a tube leading into the heart as well as the chest spreaders used to keep the chest cavity open [8].

Among these were 427,000 bypass surgeries performed on 249,000 patients [10].

Off-Pump Coronary Artery Bypass Graft Surgery Using Stabilizers

During the past several years, more surgeons have started performing off-pump coronary artery bypass graft surgery (OPCABG), where the heart continues beating while the bypass graft is sewn in place.

In these operations, a region of the heart is stabilized to provide a (almost) still work area using passive mechanical stabilizers. Motion of the target tissues is inhibited sufficiently so that operator can treat the area. Application of the stabilizer is limited to the front surface of the heart and significant residual motion is observed during stabilization [11]. Three different mechanical stabilizers were tested by Lemma *et al.* and average residual motion of left anterior descending artery (LAD) between

1.5-2.1 mm was reported. Without mechanical stabilizers, LAD exhibit an excursion of 12.5 mm, whereas its diameter is about 0.5-2.0 mm and the accuracy needed for suturing these coronary arteries is in the order of 0.1 mm.

This approach results in fewer post-operative complications since cardiopulmonary bypass (CPB) machine is avoided.

Minimally Invasive Heart Surgery

Minimally invasive coronary artery surgery is also called limited access coronary artery surgery. It is being evaluated in several medical centers as an alternative to the standard methods for CABG. Like CABG, the surgery is done to reroute, or bypass, blood around coronary arteries clogged by fatty buildups of plaque and improve the supply of blood and oxygen to the heart.

Port-access coronary artery bypass (PortCAB) or minimally invasive direct visualization coronary artery bypass (MIDCAB) are commonly used.

In PortCAB, heart is stopped and blood is pumped through a heart-lung machine to receive oxygen during the surgery. Then small incisions (ports) are made in the chest. Chest arteries or veins from a leg are attached to the heart to bypass the clogged coronary artery or arteries. The surgical team passes instruments through the ports to perform the bypasses. In the meantime, the heart surgeon views these operations on the video monitors.

MIDCAB is used to avoid the heart-lung machine. It is done while the heart is still beating and is intended for use when only one or two arteries will be bypassed. MIDCAB uses a combination of small holes or ports in the chest and a small incision made directly over the coronary artery to be bypassed. The surgeon usually detaches an artery from inside the chest wall and re-attaches it to the clogged coronary artery farthest from the occlusion. The surgeon views and performs the attachment directly-rather than using a video monitor-so the artery must be right under the incision.

1.4 Contributions

This thesis discusses the design and implementation of model-based intelligent ARMC algorithms, and a sensing system formulation for robust measurement of the heart motion.

With the proposed system, off-pump beating heart surgery will be possible without using passive stabilizers, and the surgery can be performed with the technical convenience of on-pump procedures. Establishing this will decrease the hospitalization time and the cost of the operations. The proposed control algorithm uses ECG as the biological signal to provide a better estimate of the heart motion during tracking.

In this work a novel contact-type position sensor is developed to measure the beating heart position. Using complementary and redundant sensors with the proposed control loop for active tracking of the heart will provide superior performance and safety during the beating heart bypass surgery. A preliminary noise characterization for the future sensor system implementation and optimal placement of the sensors to decrease the measurement uncertainty is given.

Although, some of the system concepts in the literature are similar to the proposed scheme in this study, there are significant differences including their lack of intelligent model-based predictive control using biological signals, and multi-sensor fusion with complementary and redundant sensors, which form the core of the proposed architecture.

With the architecture proposed in this thesis, the degree of awareness is increased by utilizing a heart motion model in reference signal estimation. Inclusion of biological signals in a model-based predictive control algorithm increases the estimation quality, and such a scheme will provide better safety with more precise detection of anomalies and switching to a safer mode of tracking.

1.5 Thesis Outline

In Chapter 2, related work in the literature and analysis of the experimental heart motion data used in this work are given. Control architecture for ARMC is proposed in Chapter 3. Chapter 4 describes the control algorithms used in the tracking problem, and discusses the importance of the ECG signal and ECG wave forms' detection. In Chapter 5, simulation and experimental results of the control algorithms are presented. The whisker position sensor system developed for measuring heart motion is described in Chapter 6. An analytical formulation for the fusion of sensing systems to be used in the future systems is given in Chapter 7. Finally, the conclusions are presented and future directions are proposed.

Chapter 2

Related Work in the Literature

2.1 Motion Canceling in Medical Interventions

The earlier studies in the literature on canceling biological motion in robotic-assisted medical interventions focus on canceling respiratory motion. Sharma *et al.* [12] and Schweikard *et al.* [13] studied the compensation of the breathing motion in order to reduce the applied radiation dose to irradiate tumors. Both studies concluded that motion compensation was achievable. Riviere *et al.* [14] looked at the cancelation of respiratory motion during percutaneous needle insertion. Their results showed that an adaptive controller was able to model and predict the breathing motion. Trejos *et al.* [15] conducted a feasibility study on the ability to perform tasks on motion-canceled targets, and demonstrated that tasks could be performed better using motion canceling.

Madhani and Salisbury [16] developed a 6-DOF telesurgical robot design for general minimally invasive surgery, which was later adapted by Intuitive Surgical Inc., Palo Alto, CA, for their commercial system, called daVinci. Computer Motion Inc., Goleta, CA[2], developed a 5-DOF telesurgical robotic system, called Zeus, with scaled motions for microsurgery and cardiac surgery. Both of these systems are currently

[2]Computer Motion Inc. was acquired by Intuitive Surgical Inc., and does not exist anymore

in use for cardiothoracic surgery applications. These systems are designed to enable dexterous minimally invasive cardiac surgery, and they are neither intended nor suitable for off-pump CABG surgery with active relative motion canceling, due to their size, bandwidth, and lack of motion tracking capabilities. These systems can only perform on-pump or off-pump CABG surgery using passive stabilizers, therefore have the same limitations as conventional tools described above.

Gilhuly *et al.* [17] tested suturing on a beating heart model using optical stabilization through strobing. They found that participants' reaction times were too slow to adjust to the changing light conditions, and concluded that stabilization methods should not rely on surgeons' reaction times.

Nakamura *et al.* [18] performed experiments to track the heart motion with a 4-DOF robot using a vision system to measure heart motion. The tracking error due to the camera feedback system was relatively large (error on the order of few millimeters in the normal direction) to perform beating heart surgery. There are also other studies in the literature on measuring heart motion. Thakor *et al.* [19] used a laser range finder system to measure one-dimensional motion of a rat's heart. Groeger *et al.* [20] used a two-camera computer vision system to measure local motion of heart and performed analysis of measured trajectories, and Koransky *et al.* [21] studied the stabilization of coronary artery motion afforded by passive cardiac stabilizers using 3-D digital sonomicrometer.

Ortmaier *et al.* [22, 23] used ECG signal in visual measurement of heart motion using a camera system for estimation of the motion when the surgical tools occluded the view. They reported significant correlations between heart surface trajectory and ECG signals, which implies these inputs can be used interchangeably. Therefore, these two independent components were considered as inputs to the estimation algorithm. In their study, heart motion estimation was not based on a heart motion model and it was completely dependent on previously recorded position data. Actual tracking of the heart motion using a robotic system was planned as future work.

More recently, in a pair of independent parallel studies by Ginhoux *et al.* [24] and Rotella [25], motion canceling through prediction of future heart motion was demonstrated. In both studies, model predictive controllers were used to get higher precision tracking. In the former, a high-speed camera was used to measure heart motion. Their results indicated a tracking error variance on the order of 6-7 pixels (approximately 1.50-1.75 mm calculated from the 40 pixel/cm resolution reported in [24]) in each direction of a 3-DOF tracking task. Although it yielded better results than earlier studies using vision systems, the error was still too large to perform heart surgery, as operation targets to be manipulated using the robotic systems in a CABG surgery are blood vessels with 2 mm or less in diameter. In Rotella's study [25], using a 1-DOF test bed system, accuracy very close to the desired error specifications for heart surgery was achieved, and it was concluded that there still was a need for better prediction of heart motion.

A heart model was proposed by Cuvillon *et al.* [26], based on the extraction of the respiration motion from the heartbeat motion using the QRS wave form of the ECG and lung airflow information as sensory inputs. They concluded that heartbeat motion is not the product of two independent components, rather the heartbeat motion is modulated by the lung volume.

Duindam and Sastry [27] proposed a method to separate 3-D quasiperiodic heart motion data into its two periodic components using ECG and respiratory information. Future heart surface motion was estimated using the separated periodic components; and an explicit model based controller was proposed to asymptotically cancel the relative motion between surgical tools and a region on the heart surface.

2.2 Analysis of Heart Data

In this section, the experimentally collected heart motion data used in this study are described. The data were collected from an animal model (an adult porcine), and all study was done based on this prerecorded data. Here, first the collection of heart motion data will be explained. The requirements for the tracking will be calculated in the data analysis section. Then, ECG, the biological signal employed, and its use in this research will be explained. Finally, a short description of the real-time ECG wave form detection will be given.

Experimental Setup for Measurement of Heart Motion

A sonomicrometry system manufactured by Sonometrics Inc. (London, Ontario, Canada) was used to collect the heart motion data used in this study. The collection was carried out by M. Cenk Cavusoglu. A sonomicrometer measures the distances within the soft tissue via ultrasound signals. A set of small piezoelectric crystals embedded, sutured, or otherwise fixed to the tissue are used to transmit and receive short pulses of ultrasound signal (Figure 2.1), and the "time of flight" of the sound wave as it travels between the transmitting and receiving crystals are measured. Using these data, the 3-D configuration of all the crystals can be calculated [28]. No analog conversion process is involved in these measurements, which eliminates the need to calibrate the system. Crystal operation frequency of 64 MHz provides resolution of 24 μm in the measurement of intertransducer distances [29]. Absolute accuracy of the sonomicrometry system is 250 μm (approximately $1/4$ wavelength of the ultrasound) [30].

The sonomicrometry system has an important advantage over using a vision system-which is the sensor of choice in the earlier works in the literature-for measuring heart motion for robotic ARMC. A stand-alone vision system is not suitable

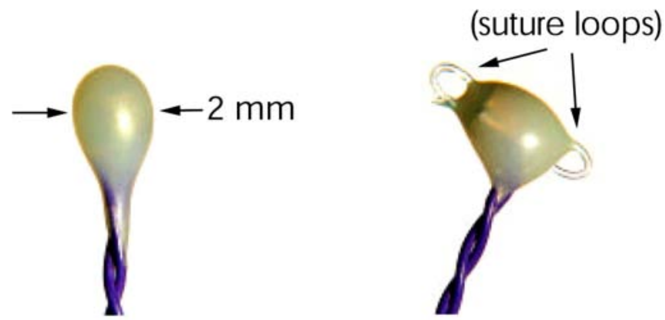

Figure 2.1: Piezoelectric crystals (courtesy of Sonometrics Corporation). Left: Standard piezoelectric crystal in 2 mm diameter that were used on the base plate. Right: Piezoelectric crystal with suture loops embedded to the crystal head. Loops are used to suture the crystal onto muscle.

for use during surgical manipulation because the surgical instruments (including the robotic tools) will occlude the point of interest (POI) rendering the vision system practically useless, whereas the sonomicrometry system does not have this shortcoming. Although an algorithm was developed by Ortmaier [22] to estimate the heart motion when the view is occluded, it is only applicable to brief occlusions.

In the experimental set-up one crystal of the sonomicrometric system was sutured next to the left anterior descending artery (LAD) located on the front surface of the left ventricle of the animal heart, at a point one third of the way from the starting point of the LAD. Six other crystals were asymmetrically mounted on a rigid plastic base of 56 mm in diameter, on a circle of diameter 50 mm, forming a reference coordinate frame. This rigid plastic sensor base was inserted behind the heart, inside the pericardial sac, and the motion of the POI on the LAD was measured relative to this coordinate frame. The pericardial sac had been filled with a saline solution, completely immersing the sensor base, which enabled the continuous contact of sonomicrometric sensor system with the heart and proper operation. Data were processed offline using the proprietary software provided with the system to calculate the 3-D motion of the POI. The only filtering performed on the data produced by the sonomicrometry system was the (very limited) removal of the outliers, which occasionally occur as a result of ultrasound echoing effects. Although the sonomicrometry system can operate at 2 kHz sampling rate for measuring the location of the POI crystal relative to the fixed base, in the test experiments, data were collected at a sampling rate of 257 Hz collecting redundant measurements.

Analysis of Heart Motion Data

During the 60 seconds data collection period, the average heart rate of the animal model was 120 beats per minute, as calculated from the ECG signal recorded simultaneously with the motion data. The peak displacement of the POI from its mean location was 12.1 mm, with a root-mean-square (RMS) value of 5.1 mm. Figure 2.2 shows the Power Spectral Density (PSD) of the motion of the POI in the y and z directions at different scales.

Two observable dominant modes of motion are visible in Figure 2.2. The first mode is at 0.37 Hz which corresponds to the breathing motion. The second dominant mode is at 2.0 Hz which corresponds to the main mode of motion due to heart beating, as it matches the frequency observed from the ECG signal. The peak at the 4.0 Hz is the first harmonic of the heartbeat motion. The component of motion data corresponding to breathing motion, which is estimated by filter has a RMS magnitude of 2.86 mm. The remainder of motion, which is due to the beating of the heart, has a RMS magnitude of 4.18 mm. The POI motion can be approximated with an error less than 273 μm RMS with frequency components up to 26 Hz. This gives the specifications for the robotic mechanism and ARMC control algorithm design. These results are consistent with the heart motion measurements reported by Groeger [20]. The data in that study were collected using a stereo vision system. The results of our study confirm the reported results by an experimental setup using an alternate sensory modality, i.e., the sonomicrometry system.

The proposed control algorithm (details in Section 3.2) is based on the premise

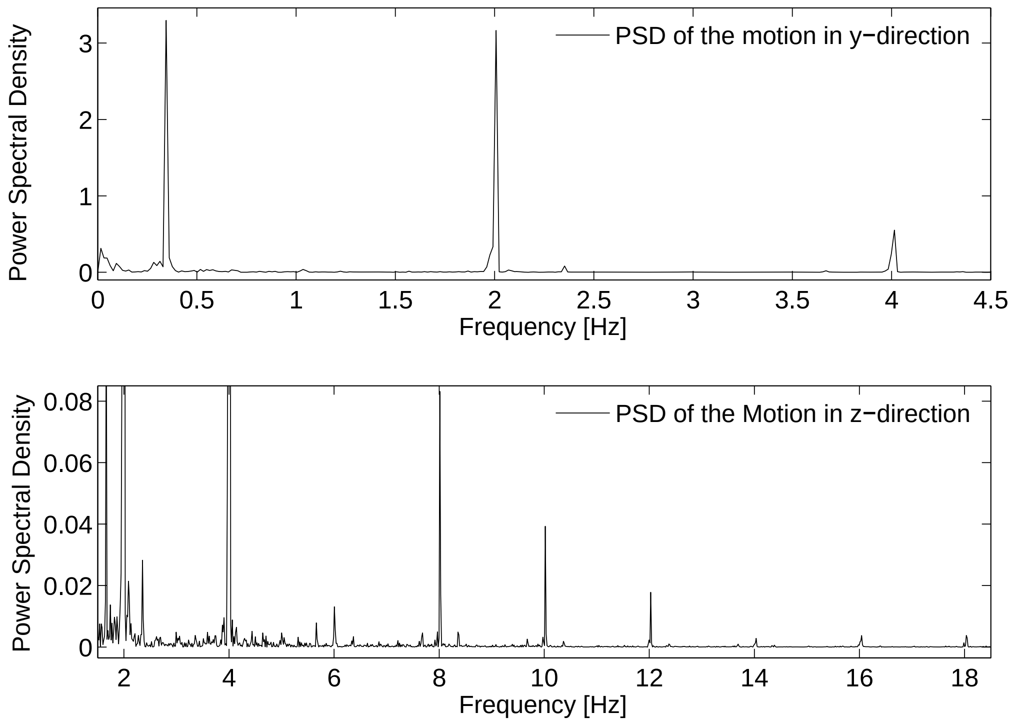

Figure 2.2: Power Spectral Density (PSD) of the motion of the point of interest (POI) is shown in two different scales. Observable dominant modes are at 0.37 Hz and 2.0 Hz, which correspond to breathing and heartbeat motions respectively. Peak at the 4.0 Hz is the first harmonic of the heartbeat motion.

that the heart motion is quasiperiodic and the motion during the previous beats can be used, to some extent, as a feedforward signal during the control of the robotic tool for ARMC. Here, our main concern is with the moderate-to-high frequency components of the motion since they are the most demanding for the mechanism and the ARMC control algorithm. As described above, the low frequency components of motion typically results from breathing (bandwidth of 1.0 Hz including the main mode of the breathing frequency), and can easily be canceled using a feedback controller. The feedforward controller is needed to cancel the high frequency components of motion. After the breathing motion is filtered out, the PSD of the motion signal is composed of very narrow peaks at the harmonics of the heartbeat frequency (Figure 2.3). This shows that the moderate-to-high frequency component of the motion is

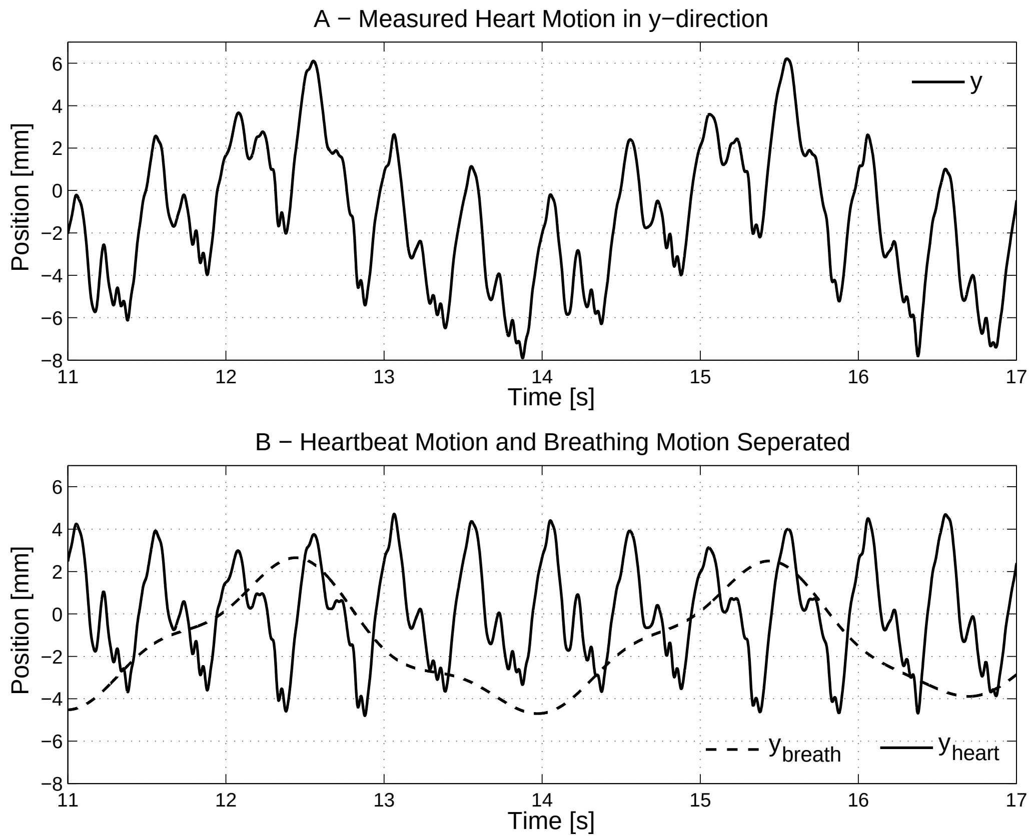

Figure 2.3: Separation of Breathing Motion and Heartbeat Motion using a low-pass filter with cutoff frequency 1.0 Hz. (**A**) Motion of the measured point of interest (POI) on the heart in y-direction. (**B**) Heartbeat Motion and Breathing Motion separated using a low-pass-filter.

quasiperiodic, with frequency equal to heartbeat rate, supporting the feasibility of the ARMC algorithm.

Chapter 3

Model-Based Active Relative Motion Cancelation

3.1 Motivation and Methodology

The control algorithm is the core of the robotic tools for tracking heart motion during coronary artery bypass graft (CABG) surgery. The tools need to track and manipulate a fast moving target with very high precision. During free beating, individual points on the heart move as much as 7-10 mm. Although the dominant mode of heart motion is on the order of 1-2 Hz, measured motion of individual points on the heart during normal beating exhibit significant energy at frequencies up to 26 Hz. The coronary arteries that are operated on during CABG surgery range from 2 mm in diameter down to smaller than 0.5 mm, which means the system needs to have a tracking precision in the order of 100 μm. This corresponds to a less than 1% dynamic tracking error up to a bandwidth of about 20 to 30 Hz.

The specifications for tracking heart motion are very demanding. These stringent requirements could not be achieved using traditional algorithms in earlier attempts reported in the literature [18,19], as they rely solely on feedback signal from measurement of heart motion using external sensors, and do not use any physiological model of the heart motion.

Using a basic model of heart motion can significantly improve tracking performance since heart motion is quasiperiodic [24]. It is also possible to use the information from the biological signals, such as ECG activity, and aortic, atrial and ventricular blood pressures, to control the robotic tools tracking the heart motion.

The proposed control architecture is shown in Figure 3.1. In this architecture, the control algorithm utilizes the biological signals in a model-based predictive control fashion. Using biological signals in the control algorithm improves the performance of the system since these signals are products of physiological processes which causally precede the heart motion. Therefore a heart motion model can be formed by combining motion data and biological signal data.

In this study, ECG signal is used in the heart model. ECG contains records for the electrical activity of the heart. Electrical signals, which stimulate the contraction of the heart muscles, precede the actual contraction by about 150-200 ms, and these signals can be observed in the ECG measurements. Because of this, ECG signal is very suitable for period-to-period synchronization with sufficient lead time for feedforward control, and identification of arrhythmias.

3.2 Intelligent Control Algorithms for Model-Based ARMC

In the Model-Based ARMC Algorithm architecture, shown in Figure 3.1, the control algorithm uses information from multiple sources: mechanical motion sensors which measure the heart motion, and sensors measuring biological signals. The control algorithm identifies the salient features of the biological signals and uses this information to predict the feedforward reference signal.

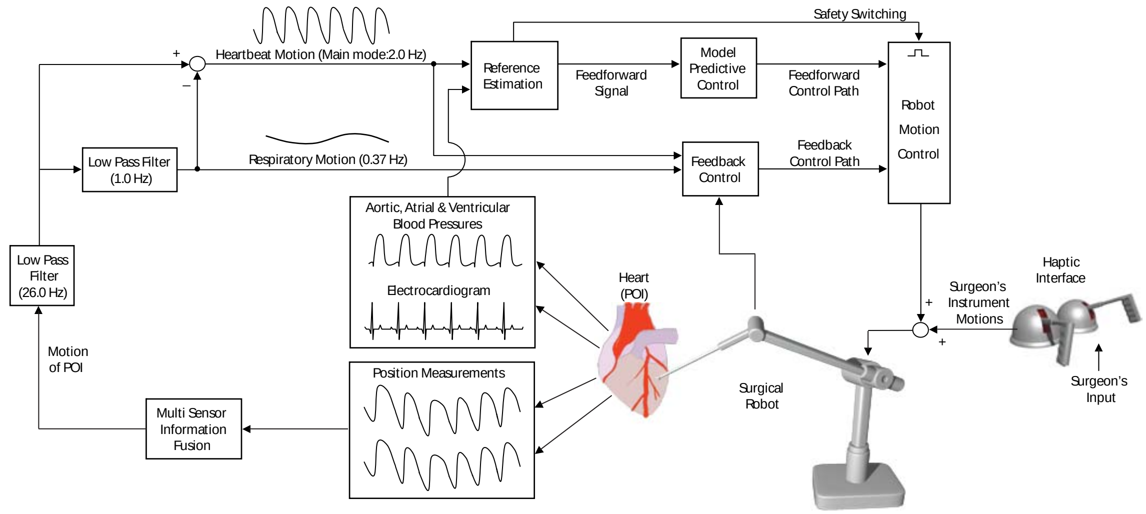

Figure 3.1: Proposed control architecture for designing Intelligent Control Algorithms for Active Relative Motion Canceling on the beating heart surgery.

The control algorithm also handles the changes in the heart motion, including adapting to slow variations in heart rhythm during the course of the surgery, as well as handling occasional arrhythmias which may have natural causes or may be due to the manipulation of the heart during surgery.

The two dominant modes of the motion of POI are separated by using a pair of complementary filters (Section 2.2). The control path for tracking of the heartbeat component of the motion has significantly more demanding requirements in terms of the bandwidth of the motion that needs to be tracked. That is why a more sophisticated feedforward algorithm is employed for this part. Respiratory motion has significantly lower frequency, and it is canceled by a purely feedback based controller. In the proposed architecture (Figure 3.1), the robot motion control signal is computed by combining these two parts. The feedforward part is calculated with the signal provided by the heart motion model, and the feedback signal is calculated with the direct measurements of heartbeat and respiratory motions. The feedforward controller was designed using the model predictive control [31] and optimal control [32, 33] methodology of modern control theory, as described in Chapter 4.

The confidence level reported by the heart motion model is used as a safety switch-

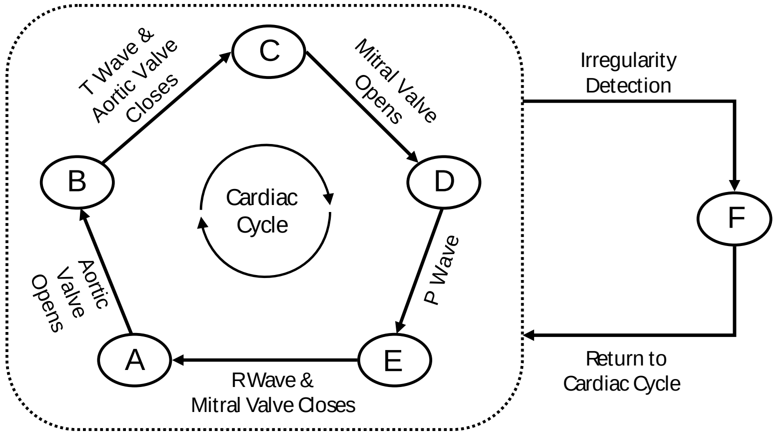

Figure 3.2: State model of the beating heart. Transition between the states are depicted using ECG waves and the motion of the heart valves, which can be inferred from blood pressure measurements. States forming the cardiac cycle are: (**A**) Isovolumic contraction; (**B**) Ejection; (**C**) Isovolumic relaxation; (**D**) Ventricular filling; (**E**) Atrial Systole; (**F**) Irregularity in the Cardiac Cycle.

ing signal to turn off the feedforward component of the controller if an arrhythmia is detected, and switch to a further fail-safe mode if necessary. This confidence level will also be used to adaptively weigh the amount of feedforward and feedback components used in the final control signal. These safety features will be an important component of the final system. Therefore, the best design strategies for developing feedforward motion control was aimed.

In Figure 3.2, a finite-state model for the cardiac cycle is shown. The model involves primary states of the heart's physiological activity. Transitions between the states are depicted using the states of the mitral and aortic valves of heart and P, R and T waves of the ECG. During the ECG wave form detection process, QRS complex is detected and used in substitute to R wave. Any out of sequence or abnormal states in the cycle can be identified as irregularity. Using this model, rhythm abnormalities and arrhythmias can be spotted and system can be switched to a safer mode of operation.

Although, some of the system concepts in the literature are similar to this scheme at the most basic level, there are significant differences including their lack of intelligent model-based predictive control using biological signals, and multi-sensor fusion with complementary and redundant sensors, which form the core of our proposed architecture. The system by Nakamura *et al.* [18] used purely position feedback obtained from a two-camera computer vision system. Neither biological signals were used in the system, nor was a feedforward control component present. The system by Ginhoux *et al.* [24] utilized a feedforward control algorithm based on model predictive control and adaptive observers; however, it did not utilize any biological signals. Ortmaier *et al.* [23] utilized ECG using a "model free" method, i.e., without using a heart model in the process.

With the architecture proposed, the degree of awareness is increased by utilizing a heart motion model in reference signal estimation. Inclusion of biological signals in a model-based predictive control algorithm increases the estimation quality, and such a scheme provides better safety with more precise detection of anomalies and switching to a safer mode of tracking.

Chapter 4

Control Algorithms

The control algorithm is the core of the robotic tools for tracking heart motion during coronary artery bypass graft (CABG) surgery. The robotic tools should have high precision to satisfy the tracking requirements [more than 97% motion cancelation (details in Section 3.2)]. During free beating, individual points on the heart move as much as 10 mm. Although the dominant mode of heart motion is in the order of 1-2 Hz, measured motion of individual points on the heart during normal beating exhibit significant energy at frequencies up to 26 Hz.

As mentioned earlier, the heart motion is quasiperiodic and previous beats can be used as a feedforward signal during the control of the robotic tool for ARMC. Rotella [25] compared a model-based predictive controller, using the estimation of the heart motion, with feedback based controllers on a 1-DOF robotic test-bed system. The model-based predictive controller outperformed the feedback based controllers both in terms of the RMS error and the control action applied. In Appendix A, the comparison of model-based predictive controller and feedback based controllers is extended to 3-D case with a 3-DOF robotic test-bed system. The results show that model-based predictive controller is more robust and effective than the traditional controllers in tracking the heart motion. Therefore, in this thesis, the focus will be

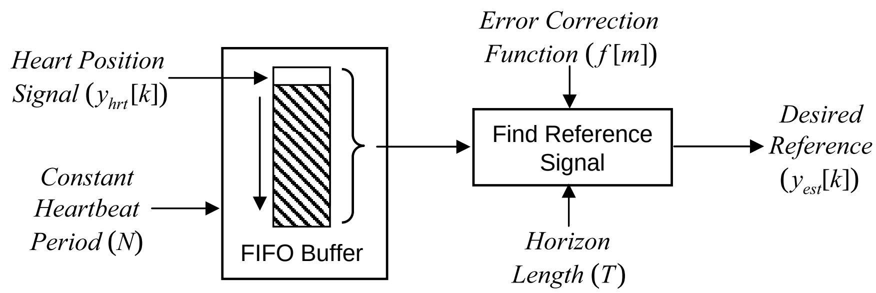

Figure 4.1: Reference Signal Estimation Block Diagram: Buffered *Past Heart Position Data* were used for estimation with approximated constant heartbeat period.

on the model-based predictive controllers.

A key component of the ARMC algorithm, when a predictive controller is used, is estimation of the reference motion of the heart which is provided to the feedforward path. If the feedforward controller has high enough precision to perform the necessary tracking, the tracking problem can be reduced to predicting the estimated reference signal effectively.

Ginhoux *et al.* [24] used an adaptive observer, which identifies the Fourier components of the past motion at the base heart rate frequency and its several harmonics to estimate the future motion. This approach assumes that the heartbeat rate stays constant. Ortmaier *et al.* [23] estimated the heart motion by matching the current heart position and ECG signals of sufficient length with recorded past signals, assuming that with similar inputs, heart would create outputs similar to the ones detected in the past.

In Sections 4.1 and 4.4, reference signal estimation schemes used for the ARMC algorithm are described. Sections 4.2 and 4.3 explain the Electrocardiogram (ECG) and ECG wave form detection methodology used in this study. Finally, the control problem and its solution are given in Sections 4.5 and 4.6 respectively.

4.1 Reference Signal Estimation

A simple prediction scheme that assumes constant heartbeat rate can be used for reference signal estimation. Heartbeat is a quasiperiodic motion with small variations in every beating cycle. If the past heartbeat motion cycle is known, it can be used as an estimate reference signal for the next cycle. Any measured heart position value can be approximated forward one cycle as long as the heartbeat period for that cycle is known. In this case, a constant heartbeat period (0.5 s) was used to store one period length of the heartbeat signal. The motion of the heart from the previous cycle was used as a prediction of the next cycle (Figure 4.1). The stored beating cycle was used as the approximate future reference beating signal in the ARMC algorithm.

Using the last heartbeat cycle exactly as the future reference would result in large errors due to the quasiperiodic characteristics of the heart motion and other irregularities of the signal. Therefore, instead of using the past beating cycle directly, the reference signal was processed online. To achieve this, any position offset between the starting point of the past cycle, $y_{hrt,pr}$, and the starting point of the next cycle (i.e., current position in time), y_{hrt}, were lined up by subtracting the difference, y_{err} (4.1). But the added offset was gradually decreased over a constant length of time (hereafter this length will be referred to as *horizon*, T) using a high order error correction function defined by (4.2). Error correction functions of different orders are shown in Figure 4.2. This calculation was carried out T steps ahead (4.3). So, only some percentage of the current error was added to the future signals, and no error was added to the signals T steps ahead (Figure 4.3). This maintained the continuity of

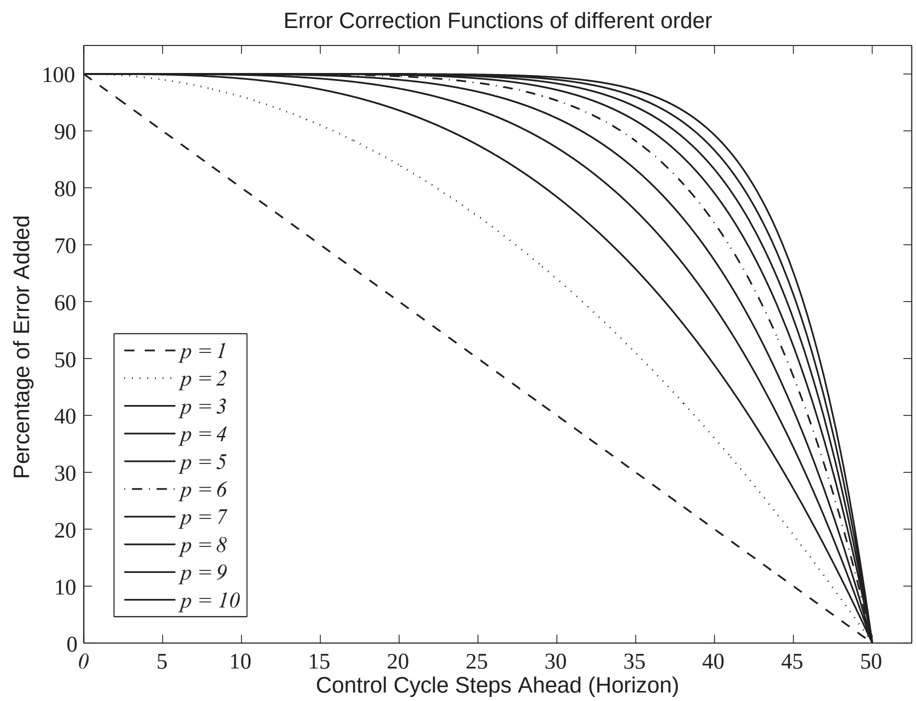

Figure 4.2: Error correction functions, f, of different orders with a $T = 50$ step horizon value.

the signal estimate and converges it onto the actual signal within the horizon ahead.

$$
\begin{aligned}
y_{err}[k] &= y_{hrt}[k] - y_{hrt,pr}[k] && (4.1)\\
f[m] &= 1 - \left(\frac{m}{T}\right)^{p} && (4.2)\\
y_{est}[k+m] &= y_{hrt,pr}[k+m] + f(m)\, y_{err}[k] && (4.3)\\
\big(m &= 0, 1, \ldots, T\big)
\end{aligned}
$$

where y_{hrt} is the measured motion of the POI on the heart, $y_{hrt,pr}$ is the measured motion of the previous cycle ($y_{hrt,pr}[k] = y_{hrt}[k - N]$, with N being the heartbeat period), y_{est} is the desired reference estimate, k is the current time step, m is the number of steps ahead that the signal is calculated, p is the order of the error correction function, and $f[m]$ is the polynomial weighting function used. In Figure 4.3, the actual and the estimated motions can be seen as the control executes.

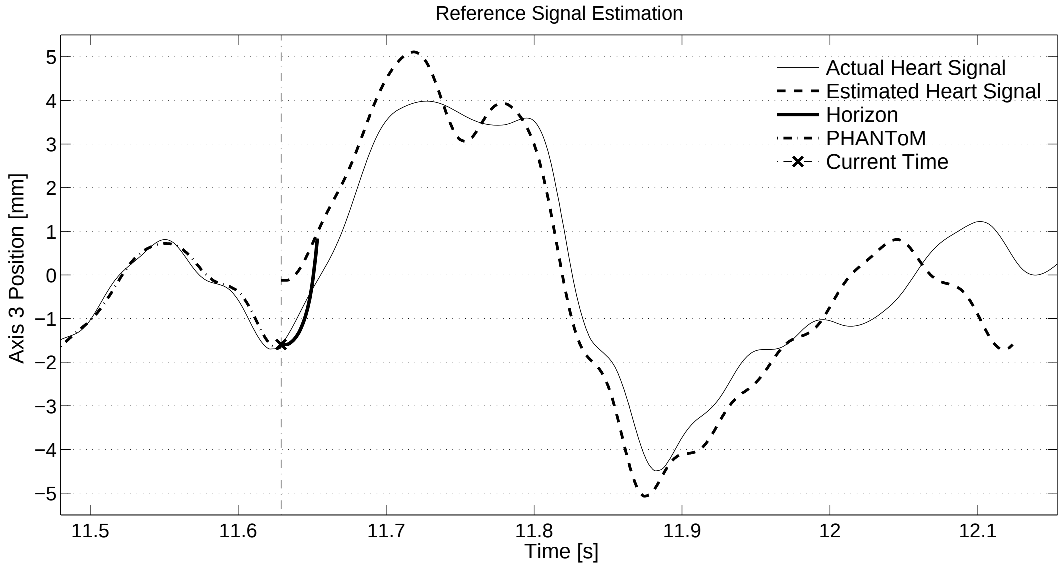

Figure 4.3: Reference Signal Estimation during control action. Observe the horizon signal where the offset between the current position and estimated signal is added gradually starting from current time to horizon steps ahead.

4.2 Electrocardiogram as the biological signal

The human body acts as a giant conductor of electrical currents. Connecting electrical *leads* to any two points on the body may be used to register an electrocardiogram (ECG). Thus, ECG contains records for the electrical activity of the heart. The ECG of heart forms a series of waves and complexes that have been labeled in alphabetical order, the P wave, the QRS complex, the T wave and the U wave (Figure 4.4) [10]. Depolarization of the atria produces the P wave; depolarization of the ventricles produces the QRS complex; and repolarization of the ventricles causes the T wave. The significance of the U wave is uncertain [34]. Each of these electrical stimulations results in a mechanical muscle twitch. This is called the electrical excitation-mechanical contraction coupling of the heart. Thus, the identification of such waves and complexes can help determine the timing of the heart muscle contractions. Using ECG in the control algorithm can improve the performance of the position estimation because these wave forms are results of physiological processes that causally precede the heart motion and also because ECG is significantly correlated with heartbeat

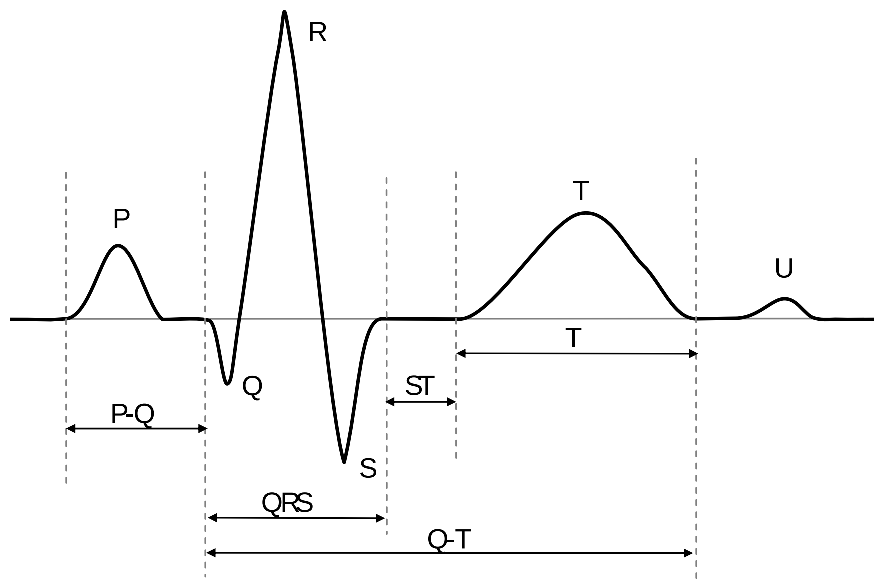

Figure 4.4: Typical scalar electrocardiogram (ECG), showing significant intervals and deflections.

motion [23]. The time relationship between action potential and mechanical force developed by ventricular muscle is shown in Figure 4.5 [35, 36]. Rapid depolarization of a cardiac muscle fiber is followed by force development in the muscle. The completion of repolarization coincides approximately with the peak force, and the duration of contraction parallels the duration of the action potential, which is about 150 to 200 ms long. The lag between these two formations enables the prediction of future heart activity. Although this time lag is about 200 ms, it is sufficient for real-time detection of the waves and complexes of the ECG. Average detection time for the test data was 174 ms (see Section 4.3 for test database details).

The ECG signal employed in this research was collected with the analog data acquisition part of the sonomicrometry system used. The ECG data were recorded simultaneously with the collection of the heart motion data at the same sampling rate of 257 Hz.

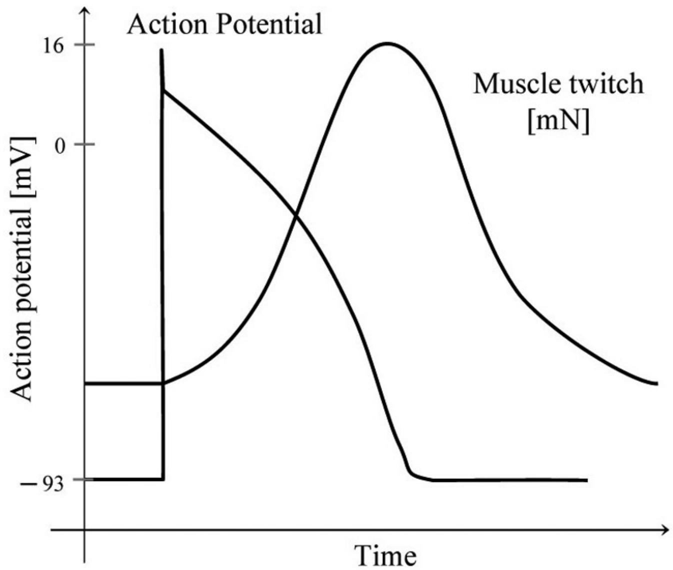

Figure 4.5: Time relationship between action potential and mechanical force developed by ventricular muscle. Rapid depolarization of a cardiac muscle fiber is followed by force development in the muscle. The lag between the excitation and the peak force is about 200 ms long.

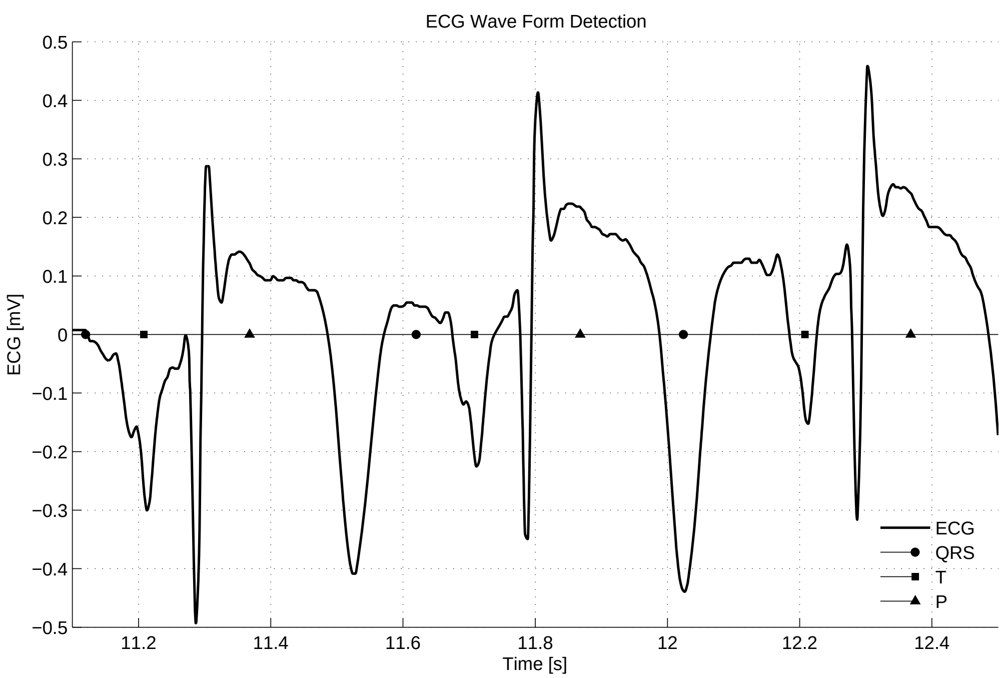

Figure 4.6: Detection of ECG Wave Forms: Detected ● QRS Complex, ■ T Wave, and ▲ P Wave are shown. Note that the marked times correspond to when features are detected, which is delayed from the actual temporal location of the waveform about 170 ms due to the time taken by the detection algorithm.

4.3 ECG Wave Form Detection

There is substantial literature on detecting the ECG characteristic points with high detection accuracies (e.g. [37–40]). However most of these algorithms are designed for offline processing of ECG signals and only a few of them are for real-time detection of ECG signal complexes [41, 42]. The difficulty in detection arises from the diversity of complex wave forms and the noise and artifacts accompanying the ECG signals. In this work, the significant ECG wave forms and points, such as P, QRS and T, were detected in hard real time[3] by an algorithm adapted from Bahoura *et al.* [42]. This one was selected among other available algorithms because it employs signal localization both in time and frequency using wavelet analysis, characterization of the local regularity of the signal and separation of the ECG waves from serious noise, artifacts, and baseline drifts in real time.

A short explanation of the ECG wave form detection algorithm is as follows. Wavelet transform of the ECG data at the sampling frequency was calculated at scales 2^j, $j = 1 ... 5$. These energy levels cover the power spectra of ECG signal: The energy of the QRS complex is typically placed in the levels 2^3 and 2^4, whereas the energies of P and T waves are located at levels 2^4 and 2^5. To detect peaks, threshold filters and decision making rules were used in every energy level. First, QRS complexes were detected by locating any peak pairs on the wavelet transforms. Since both QRS and T peak pairs can appear on the same energy levels, unmarked peaks on levels 2^4 and 2^5 were marked as T waves after the possible QRS complexes were identified. P wave detection was done similarly by detecting peak pairs at the energy scale 2^4 which corresponded to neither a QRS complex nor a T wave.

Bahoura *et al.* [42] evaluated the original algorithm in real time with the MIT-BIH Arrythmia Database [43]. This database contains 48 half-hour excerpts of two-

[3] In hard real time no corrections are allowed to be performed to the past data after the operation deadline expires.

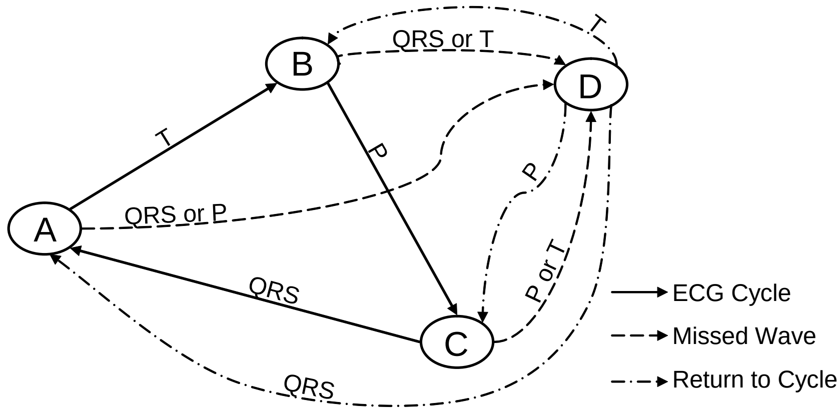

Figure 4.7: Finite-state model for the ECG Wave form detection.

channel ambulatory ECG recordings. The recordings were digitized at 360 samples per second per channel with 11-bit resolution over a 10 mV range. Two or more cardiologists independently annotated each record; disagreements were resolved to obtain the computer-readable reference annotations for each beat included with the database. Using the database, Bahoura *et al.* [42] reported a 0.29% false detection rate (135 false positive beats and 184 false negative beats out of 109,809 beats), showing the algorithms capability in detecting QRS complexes. Constant detection parameters rather than adaptive ones were used, and this produced a 1.49% false detection rate using the same database (408 false positive beats and 709 false negative beats out of 75,010 healthy beats). Table 4.1 summarizes the performance results for both evaluations. Note that no healthy beats were annotated for some of the ECG recordings (i.e., 107, 109, 111, etc.) and therefore no healthy QRS detections were viable in these cases.

With this method, QRS-T-P waves were detected in real time for the collected 56 s ECG data with 100% QRS complex and T wave detection rates, and 97.3% P wave detection rate (Figure 4.6). Missed waves were determined according to the ECG state transitions shown in Figure 4.7. Detected signals were used to estimate the Reference Signal as described in Section 4.4 (Figure 4.8).

Table 4.1: QRS detection performance results using MIT-BIH Arrhythmia Database

			Bahoura *et al.*				Bebek *et al.*			
Data Type	Total Beats	Healthy Beats	False Positive	False Negative	False Detection		False Positive	False Negative	False Detection	
100	2273	2237	0	0	0	0.00%	0	0	0	0.00%
101	1865	1859	0	2	2	0.11%	2	0	2	0.11%
102	2187	99	0	0	0	0.00%	0	1	1	1.01%
103	2084	2081	0	1	1	0.05%	1	0	1	0.05%
104	2230	163	10	2	12	0.54%	0	0	0	0.00%
105	2572	2526	27	15	42	1.63%	103	5	108	4.28%
106	2027	1507	6	2	8	0.39%	7	0	7	0.46%
107	2137	0	0	1	1	0.05%				
108	1763	1739	20	29	49	2.78%	10	73	83	4.77%
109	2532	0	0	1	1	0.04%				
111	2124	0	1	0	1	0.05%				
112	2539	2535	2	3	5	0.20%	9	0	9	0.36%
113	1795	1787	0	1	1	0.06%	0	0	0	0.00%
114	1879	1820	4	2	6	0.32%	1	228	229	12.58%
115	1953	1951	0	0	0	0.00%	0	0	0	0.00%
116	2412	2301	4	2	6	0.25%	3	21	24	1.04%
117	1535	1533	0	0	0	0.00%	2	0	2	0.13%
118	2275	0	1	0	1	0.04%				
119	1987	1543	2	1	3	0.15%	0	0	0	0.00%
121	1863	1859	2	2	4	0.21%	1	21	22	1.18%
122	2476	2474	0	0	0	0.00%	0	0	0	0.00%
123	1518	1514	0	0	0	0.00%	1	0	1	0.07%
124	1619	0	1	0	1	0.06%				
200	2601	1742	0	0	0	0.00%	31	2	33	1.89%
201	1963	1623	7	24	31	1.58%	0	1	1	0.06%
202	2136	2060	1	0	1	0.05%	0	2	2	0.10%
203	2982	2528	11	21	32	1.07%	54	57	111	4.39%
205	2656	2570	1	3	4	0.15%	0	3	3	0.12%
207	1862	0	3	5	8	0.43%				
208	2956	1585	2	6	8	0.27%	27	10	37	2.33%
209	3004	2620	0	1	1	0.03%	18	2	20	0.76%
210	2647	2421	2	4	6	0.23%	9	6	15	0.62%
212	2748	922	0	0	0	0.00%	9	0	9	0.98%
213	3251	2639	0	1	1	0.03%	5	0	5	0.19%
214	2262	0	1	2	3	0.13%				
215	3363	3194	0	0	0	0.00%	5	0	5	0.16%
217	2208	244	1	2	3	0.14%	7	0	7	2.87%
219	2154	2082	0	0	0	0.00%	18	0	18	0.86%
220	2048	1952	0	0	0	0.00%	1	0	1	0.05%
221	2427	2030	2	0	2	0.08%	0	1	1	0.05%
222	2484	2060	12	27	39	1.57%	9	266	275	13.35%
223	2605	2028	0	1	1	0.04%	2	0	2	0.10%
228	2053	1687	11	23	34	1.66%	25	8	33	1.96%
230	2256	2253	0	0	0	0.00%	14	1	15	0.67%
231	1886	314	0	0	0	0.00%	0	0	0	0.00%
232	1780	0	1	0	1	0.06%				
233	3079	2229	0	0	0	0.00%	34	1	35	1.57%
234	2753	2699	0	0	0	0.00%	0	0	0	0.00%
Total	109 809	75 010	135	184	319	0.29%	408	709	1117	1.49%

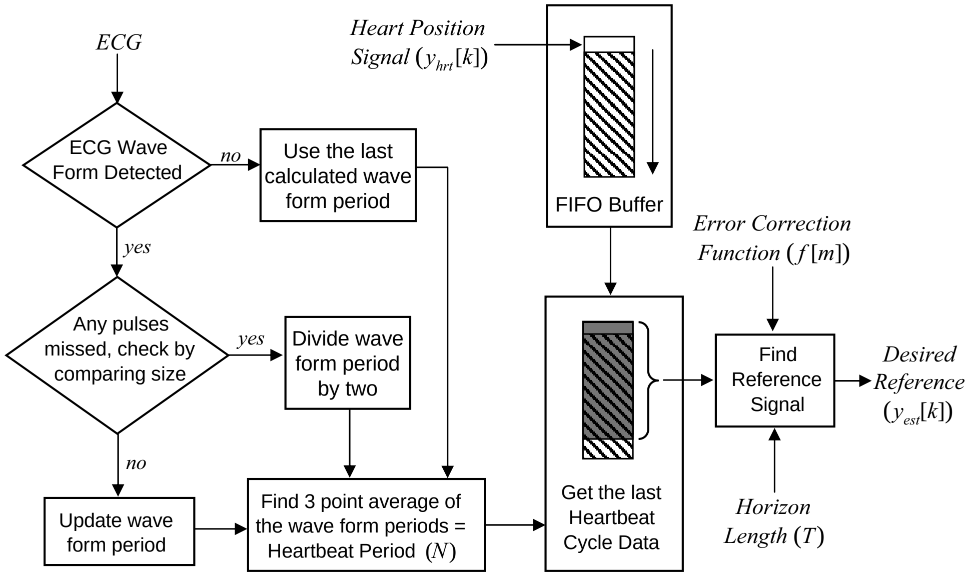

Figure 4.8: Simplified finite state model of the Reference Signal Estimation algorithm using ECG. Detected ECG Wave forms were used in the estimation of *Reference*, with the buffered *Past Heart Position Data*.

4.4 Reference Signal Estimation Using Biological Signals

Although the position offset between the previous and current beating cycles can be eliminated gradually using the technique given in Section 4.1, the error due to changes in heartbeat period remains. Because heartbeat is a quasiperiodic motion with small period variations in every beating cycle, these period changes could result in large offsets in the estimated signal, and can cause jumps during the tracking.

As mentioned earlier in the Section 4.2, ECG signal is very suitable for period-to-period synchronization. In this reference signal estimation scheme, rather than using a constant heartbeat period, a variable period that was calculated using ECG was used. QRS, P, and T waves were used as check points for detecting heartbeat period. In Figure 4.8, the block diagram for reference signal estimation using ECG is illustrated.

Here, past heart position data were stored on the fly into a FIFO buffer which

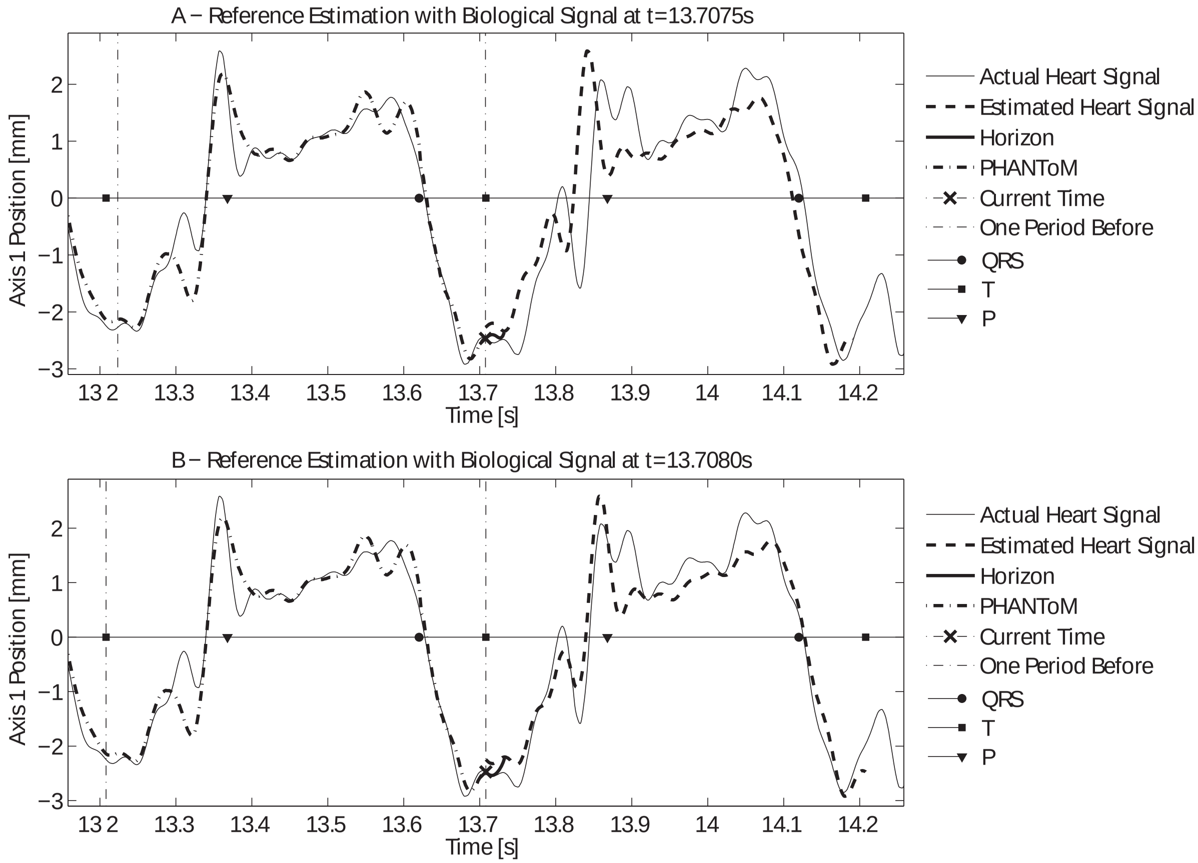

Figure 4.9: Reference Estimation with Biological Signal. (**A**) *Just before T Wave was detected:* Estimated Heart Signal did not fit well with the Actual Heart Signal. T Wave detection was shown with ■ markers. (**B**) *T Wave has been detected:* Heart Period and Estimated Signal were adjusted. Observe that the beginning of the previous heartbeat period marker [·–·–·](t≈13.22 s) was shifted back in time (t≈13.21 s) as a result of the increase in the heartbeat period. Accordingly, Estimated Heart Signal was changed to adjust with the new period. RMS estimation error was decreased from 0.887 mm to 0.456 mm with the shift.

was 1300 elements long (i.e. 650 ms of data; also note that average heartbeat period is about 500 ms long). The most recently stored part of the heart position buffer, in the length of updated heartbeat period using ECG, was used in the estimation.

The current heartbeat period was calculated by averaging the periods of the three ECG wave forms. The period was updated continuously as new wave forms were detected. If detection of any ECG wave form was missed, the period of the missed signal was doubled to compensate for the missing signal. Some upper and lower period boundaries were imposed in order to eliminate any misses by the detection algorithm.

In Figure 4.9 the estimated signals just before and after the detection of a new wave form are shown. In Figure 4.9(B), observe that after the T wave was detected, the past heartbeat period time mark was shifted back in time as a result of the increase in the heartbeat period. In the example shown with Figures 4.9(A) and 4.9(B), RMS estimation error for one heartbeat period ahead decreased from 0.887 mm to 0.456 mm after the shift. With the use of ECG in ARMC algorithm, heartbeat period in the estimation of reference signal can be adjusted online.

4.5 Control Problem

Having the estimated trajectory of the next cycle in hand, the following control problem arises: Tracking of heart motion where there is some knowledge of the future motion. Then, this optimal tracking problem can be stated as follows.

Suppose the dynamics of the robotic surgical manipulator is given by an n-dimensional linear system having state equations

$$x[k+1] = \mathbf{\Phi} x[k] + \mathbf{\Gamma} u[k] \tag{4.4}$$

$$y[k] = \mathbf{H} x[k] \ . \tag{4.5}$$

Here, if the dimensions of $\mathbf{\Phi}$, $\mathbf{\Gamma}$, and $\mathbf{H}$ are $n{\times}n$, $n{\times}m$ and $l{\times}n$ respectively; then $x[k] \in \mathbb{R}^n$ denotes the system state at time k where $x[k_0]$ is given for some time k_0 such that $k_0{\leq}k$; $u[k] \in \mathbb{R}^m$ denotes system control at time k; and the $y[k] \in \mathbb{R}^l$ denotes the system output at time k where l entries of y are linearly independent, or equivalently, the matrix $\mathbf{H}$ has rank l. Suppose we are also given an l-vector $y_{est}[k]$ for all k in the range $k_0{\leq}k{\leq}k_0{+}T$ for some times k_0 and T. The optimal tracking problem is then to find the optimal control u for the system (4.4)-(4.5), such that the output y tracks the signal y_{est}, minimizing the index (4.6)

$$J[k] = \sum_{k=k_0}^{k_0+T} \Big((x[k] - x_{est}[k])^T \mathbf{Q} (x[k] - x_{est}[k]) + u^T[k] \mathbf{R} u[k] \Big) \tag{4.6}$$

$$x_{est} = \mathbf{L} y_{est} \tag{4.7}$$

where $\mathbf{Q}$ is a non-negative definite symmetric matrix and $\mathbf{R}$ is a positive definite symmetric matrix, and, $\mathbf{L}$ and $\mathbf{Q}$ are

$$\mathbf{L} = \mathbf{H}^T (\mathbf{H}\mathbf{H}^T)^{-1} \tag{4.8}$$

$$\mathbf{Q} = \big(\mathbf{I} - \mathbf{L}\mathbf{H}\big)^T \mathbf{Q}_1 \big(\mathbf{I} - \mathbf{L}\mathbf{H}\big) + \mathbf{H}^T \mathbf{Q}_2 \mathbf{H}. \tag{4.9}$$

where $\mathbf{Q_1}$ and $\mathbf{Q_2}$ are non-negative definite symmetric matrices.

4.6 Receding Horizon Model Predictive Control

Solution to the control problem given in Section 4.5 was derived using the method given in [32]. An optimal tracking system can be derived using regulator theory. Such controller consist of a standard optimal feedback regulator involving the backwards solution of a Riccati equation, and an external signal (feedforward) that results from the backwards solution of a linear differential equation. Unmeasurable states can be replaced by state estimates, under observability of $\mathbf{\Phi}$ and $\mathbf{H}$ (Appendix A.1). Next, optimal feedback regulator and optimal tracking gain calculations will be described separately even though they depend on many of the same parameters, and solution to the control problem will be given.

Optimal Feedback Regulator

To better explain the optimal tracking problem, first the optimal control (or linear quadratic regulation) will be explained. An optimal regulator can be seen as an optimal tracking controller where the desired trajectory is zero. Performance index can be defined as

$$J[k] = \sum_{k=k_0}^{k_0+T} (x^T[k+1]\mathbf{Q}x[k+1] + u^T[k]\mathbf{R}u[k]) \tag{4.10}$$

This equation takes the form of a quadratic in the control effort and in the state vector of the system. The idea behind the optimal controller is to find a control effort that will minimize a cost index equation. Then using the principles of optimality (4.10) can be transformed into (4.11). The goal for this type of control is to minimize (4.11) with respect to the control $u[k]$.

$$J^*[k] = \min_{u[k]} \left(x^T[k+1]\mathbf{Q}x[k+1] + u^T[k]\mathbf{R}u[k] + J^*[k+1] \right) \tag{4.11}$$

$J^*[k]$ is the optimal index at time k. $\mathbf{Q} \in \mathbb{R}^{n\times n}$ and $\mathbf{R} \in \mathbb{R}^{m\times m}$ are matrix weighting parameters. By altering the ratio between $\mathbf{Q}$ and $\mathbf{R}$, the emphasis of the optimization problem is shifted. Using a higher $\mathbf{Q}$ to $\mathbf{R}$ ratio will accentuate the state and hence regulate more quickly. Using a lower $\mathbf{Q}$ to $\mathbf{R}$ ratio penalizes higher control values, so the regulation is slower but uses a smaller control effort. The $\mathbf{Q}$ and $\mathbf{R}$ matrices should be positive semi-definite and positive definite, respectively.

Often for simplicity, the matrices are created as multiples of the identity matrix. For systems with many states and multiple inputs, this simplifies the tuning process to two parameters. However, it is possible to weight more heavily different indices of each matrix in an attempt to penalize particular states or inputs.

Attempting to minimize $y - y_{est}$ is equal to constrain $\mathbf{H}x$. If $\mathbf{H}$ has rank r, this imposes r constraints on x. By generalizing the performance index, $n-r$ further constraints can be aimed for x without creating conflict of objectives. Then, formation of the $\mathbf{Q}$ matrix is given below.

$$\mathbf{Q} = \underline{\mathbf{H}}^T \mathbf{Q}_1 \underline{\mathbf{H}} + \mathbf{H}^T \mathbf{Q}_2 \mathbf{H} \tag{4.12}$$

So, the optimal index can also be written as

$$J^*[k] = \min_{u[k]} \left(\underline{y}^T[k] \mathbf{Q}_1 \underline{y}[k] + (y[k] - y_{est}[k])^T \mathbf{Q}_2 (y[k] - y_{est}[k]) + u^T[k] \mathbf{R} u[k] + J^*[k+1] \right) \tag{4.13}$$

where $\mathbf{Q}_1 \in \mathbb{R}^{n \times n}$ and $\mathbf{Q}_2 \in \mathbb{R}^{p \times p}$ are nonnegative definite symmetric matrices and $\underline{y}$ is defined as

$$\begin{aligned} \underline{y}[k] &= \underline{\mathbf{H}} x[k] \quad \left(\text{Note that : } \; \mathbf{H}\underline{y}[k] = 0 \right) \\ \mathbf{L} &= \mathbf{H}^T (\mathbf{H}\mathbf{H}^T)^{-1} \\ \underline{\mathbf{H}} &= \mathbf{I} - \mathbf{L}\mathbf{H}. \end{aligned} \tag{4.14}$$

For any regulation problem the actual control equation takes the form

$$u[k] = \mathbf{K}[k] x[k]. \tag{4.15}$$

The optimal index equation can be written in terms of a quadratic of the state and the next optimal index by substituting in the control equation.

As it was stated before, this representation is discrete so the state-space equation is a difference equation. Which means, $x[k+1]$ can be written in terms of $x[k]$ and $u[k]$. By also making this substitution, the cost equation (4.11) can now be written completely in terms of the current state, $x[k]$, and the next cost index, $J^*[k+1]$. Note that the $u[k]$ term is again eliminated through the control equation.

$$J^*[k] = (\mathbf{\Phi}x[k]+\mathbf{\Gamma}\mathbf{K}[k]x[k])^T\mathbf{Q}(\mathbf{\Phi}x[k]+\mathbf{\Gamma}\mathbf{K}[k]x[k])+(\mathbf{K}[k]x[k])^T\mathbf{R}(\mathbf{K}[k]x[k])+J^*[k+1] \tag{4.16}$$

In an attempt to solve (4.16), (4.17) is assumed to be a solution.

$$J^*[k] = x^T[k]\mathbf{P}[k]x[k] \tag{4.17}$$

Upon substituting in (4.17), nearly every term of (4.16) is a quadratic in terms of the current value of the state. By repeating the two substitutions used to create (4.16), the $J^*[k+1]$ term can be written in terms of the current state as

$$\begin{aligned} J^*[k+1] &= x^T[k+1]\mathbf{P}[k+1]x[k+1] \\ &= \big(\mathbf{\Phi}x[k]+\mathbf{\Gamma}u[k]\big)^T\mathbf{P}[k+1]\big(\mathbf{\Phi}x[k]+\mathbf{\Gamma}u[k]\big) \\ &= \big(\mathbf{\Phi}x[k]+\mathbf{\Gamma}\mathbf{K}x[k]\big)^T\mathbf{P}[k+1]\big(\mathbf{\Phi}x[k]+\mathbf{\Gamma}\mathbf{K}x[k]\big). \end{aligned} \tag{4.18}$$

When eliminating the state from both sides of the equation, it can be seen that $\mathbf{P}[k]$ is actually a solution to a difference matrix Riccatti equation. This Riccatti equation can be solved by backwards iteration where the final value is $\mathbf{P}[T] = \mathbf{0}$. All the parameters in (4.16) are known except $\mathbf{K}$. It is necessary to solve algebraically for this gain in order to solve numerically the Riccatti equation.

The optimal gain $\mathbf{K}$ is solved for by taking the derivative of $J^*[k]$ with respect to the control effort, $u[k]$, and setting it equal to zero. In order to take the derivative of the $J^*[k+1]$ term, it is replaced by $x^T[k+1]\mathbf{P}[k+1]x[k+1]$ and then subsequently the $x[k+1]$ is exchanged with the state equation. Solving for $u[k]$ then produces (4.19).

$$u[k] = -\Big(\mathbf{R} + \mathbf{\Gamma}^T\big(\mathbf{Q} + \mathbf{P}[k+1]\big)\mathbf{\Gamma}\Big)^{-1}\Big(\mathbf{\Gamma}^T\big(\mathbf{Q} + \mathbf{P}[k+1]\big)\mathbf{\Phi}\Big)x[k] \tag{4.19}$$

$$\mathbf{K}[k] = -\Big(\mathbf{R} + \mathbf{\Gamma}^T\big(\mathbf{Q} + \mathbf{P}[k+1]\big)\mathbf{\Gamma}\Big)^{-1}\Big(\mathbf{\Gamma}^T\big(\mathbf{Q} + \mathbf{P}[k+1]\big)\mathbf{\Phi}\Big) \tag{4.20}$$

This derivation shows the optimal gain as a function of time. The Riccatti equation is now

$$\begin{aligned}\mathbf{P}[k] = \mathbf{\Phi}^T\Big\{&\mathbf{Q} + \mathbf{P}[k+1] - \\ &\big(\mathbf{Q} + \mathbf{P}[k+1]\big)\mathbf{\Gamma}\Big[\mathbf{R} + \mathbf{\Gamma}^T\big(\mathbf{Q} + \mathbf{P}[k+1]\big)\mathbf{\Gamma}\Big]^{-1}\mathbf{\Gamma}^T\big(\mathbf{Q} + \mathbf{P}[k+1]\big)\Big\}\mathbf{\Phi}\end{aligned} \tag{4.21}$$

This Riccatti equation is dependent only on the system model and the weighting matrices $\mathbf{Q}$ and $\mathbf{R}$. This equation is independent of the system states, the system output and the control values. This means that the gain is based only on static matrices and iterative parameters. Therefore the gains can be solved before control is exercised on the plant using backwards iteration. The iteration is backwards in the sense that the starting point of the iteration is some horizon into the future, $k = k_0 + T$, and the calculation occurs backwards in time to the present, $k = k_0$.

For simplification during the implementation phase, the $\mathbf{Q}$ weighting matrix will be combined with $\mathbf{P}[k]$ to form a new Riccatti parameter, $\mathbf{S}[k]$, which is defined by the (4.22). The final condition for $\mathbf{S}[T]$ is equal to $\mathbf{Q}$. Either $\mathbf{P}[k]$ (4.21) or $\mathbf{S}[k]$ (4.23) can be used to determine $\mathbf{K}[k]$ in the iteration loop. But, since $\mathbf{S}[k]$ will be used in the calculation of the overall control term, $\mathbf{S}[k]$ is used in the iteration process.

$$\mathbf{S}[k] = \mathbf{P}[k] + \mathbf{Q} \tag{4.22}$$

$$\mathbf{S}[k] = \mathbf{\Phi}^T\Big(\mathbf{S}[k+1] - \mathbf{S}[k+1]\mathbf{\Gamma}\big(\mathbf{R} + \mathbf{\Gamma}^T\mathbf{S}[k+1]\mathbf{\Gamma}\big)^{-1}\mathbf{\Gamma}^T\mathbf{S}[k+1]\Big)\mathbf{\Phi} + \mathbf{Q} \tag{4.23}$$

Accordingly, $\mathbf{K}[k]$ (Equation 4.20) can be written as a function $\mathbf{S}[k]$.

$$\mathbf{K}[k] = -\Big(\mathbf{R} + \mathbf{\Gamma}^T\mathbf{S}[k+1]\mathbf{\Gamma}\Big)^{-1}\Big(\mathbf{\Gamma}^T\mathbf{S}[k+1]\mathbf{\Phi}\Big) \tag{4.24}$$

Optimal Tracking

An auxiliary system is defined for the estimated signal such that it possesses the same states as the plant. The relationship between this estimated state and the estimated output can be described with a difference equation and an output equation.

$$\begin{aligned} x_{est}[k+1] &= \mathbf{F}x_{est}[k] \\ y_{est}[k] &= \mathbf{G}x_{est}[k] \end{aligned} \tag{4.25}$$

For tracking purposes, the cost index should attempt to minimize the error between the newly defined desired state and actual system state. The equation would hence take the form

$$J^*[k] = \min_{u[k]}\Big(\big(x[k+1] - x_{est}[k+1]\big)^T\mathbf{Q}\big(x[k+1] - x_{est}[k+1]\big) + u^T[k]\mathbf{R}u[k] + J^*[k+1]\Big) \tag{4.26}$$

This form can be forced into the original form (4.11) by creating a new state vector and carefully choosing the weighting parameter $\mathbf{Q}$.

A new state vector is defined that augments the current state vector with the states of the auxiliary system. The new state vector now looks like

$$\widetilde{x} = \begin{bmatrix} x \\ x_{est} \end{bmatrix}. \tag{4.27}$$

By choosing $\mathbf{Q}$ as seen below, the cost index equation can attempt to regulate $x - x_{est}$ and mimic the form of the regulator problem which already has a solution.

Note that the subscripts are dropped for simplification. The matrix $\mathbf{Q}$ is originally an $n \times n$ matrix where n is the order of the system. The augmented state is now a $2n \times 1$ vector and hence $\widetilde{\mathbf{Q}}$ is a $2n \times 2n$ matrix.

$$(x - x_{est})^T \mathbf{Q}(x - x_{est}) = x^T \mathbf{Q} x - x^T \mathbf{Q} x_{est} - x_{est}^T \mathbf{Q} x + x_{est}^T \mathbf{Q} x_{est} \tag{4.28}$$

$$\widetilde{\mathbf{Q}} = \begin{bmatrix} \widetilde{q}_{11} & \widetilde{q}_{21} \\ \widetilde{q}_{12} & \widetilde{q}_{22} \end{bmatrix} \tag{4.29}$$

$$\begin{bmatrix} x^T & x_{est}^T \end{bmatrix} \widetilde{\mathbf{Q}} \begin{bmatrix} x \\ x_{est} \end{bmatrix} = x^T \widetilde{q}_{11} x + x^T \widetilde{q}_{21} x_{est} + x_{est}^T \widetilde{q}_{12} x + x_{est}^T \widetilde{q}_{22} x_{est} \tag{4.30}$$

Comparing (4.28) and (4.30), $\widetilde{\mathbf{Q}}$ can be deduced as

$$\widetilde{\mathbf{Q}} = \begin{bmatrix} \mathbf{Q} & -\mathbf{Q} \\ -\mathbf{Q} & \mathbf{Q} \end{bmatrix} \tag{4.31}$$

Since the state has been augmented, it will be necessary to define a new state equation. Using (4.25), the below augmented state-space is obtained.

$$\widetilde{x}[k+1] = \widetilde{\mathbf{\Phi}} \widetilde{x}[k] + \widetilde{\mathbf{\Gamma}} u[k] \tag{4.32}$$

$$\widetilde{\mathbf{\Phi}} = \begin{bmatrix} \Phi & \mathbf{0} \\ \mathbf{0} & \mathbf{F} \end{bmatrix} \quad and \quad \widetilde{\mathbf{\Gamma}} = \begin{bmatrix} \mathbf{\Gamma} \\ \mathbf{0} \end{bmatrix} \tag{4.33}$$

At this point the tracking problem can be treated as the regulator problem. The control effort equation will also retain the form of $u[k] = \widetilde{\mathbf{K}}[k]\widetilde{x}[k]$, where $\widetilde{x}[k]$ is the augmented state. The gain $\widetilde{\mathbf{K}}[k]$ can be written as seen below.

$$\widetilde{\mathbf{K}}[k] = -\Big(\widetilde{\mathbf{\Gamma}}^T \big(\widetilde{\mathbf{P}}[k+1] + \widetilde{\mathbf{Q}}\big) \widetilde{\mathbf{\Gamma}} + \mathbf{R}\Big)^{-1} \widetilde{\mathbf{\Gamma}}^T \big(\widetilde{\mathbf{P}}[k+1] + \widetilde{\mathbf{Q}}\big) \widetilde{\mathbf{\Phi}} \tag{4.34}$$

The $\widetilde{\mathbf{P}}[k]$ is the Riccatti equation parameter. For simplification the $\widetilde{\mathbf{Q}}$ weighting matrix will be combined with $\widetilde{\mathbf{P}}[k]$ to form a new Riccatti parameter which is defined by the equation below.

$$\widetilde{\mathbf{S}}[k] = \widetilde{\mathbf{P}}[k] + \widetilde{\mathbf{Q}} \tag{4.35}$$

$$\widetilde{\mathbf{S}}[k] = \widetilde{\Phi}^T\Big(\widetilde{\mathbf{S}}[k+1] - \widetilde{\mathbf{S}}[k+1]\widetilde{\mathbf{\Gamma}}\big(\mathbf{R} + \widetilde{\mathbf{\Gamma}}^T\widetilde{\mathbf{S}}[k+1]\widetilde{\mathbf{\Gamma}}\big)^{-1}\widetilde{\mathbf{\Gamma}}^T\widetilde{\mathbf{S}}[k+1]\Big)\widetilde{\mathbf{\Phi}} + \widetilde{\mathbf{Q}} \tag{4.36}$$

The control effort equation can be broken down into block form using 4 terms to make up the Riccatti parameter and expanding each of the state-space terms.

$$\widetilde{\mathbf{S}}[k] = \begin{bmatrix} \mathbf{S}_{11} & \mathbf{S}_{12} \\ \mathbf{S}_{21} & \mathbf{S}_{22} \end{bmatrix} \tag{4.37}$$

Note that in (4.37) *all of the matrix blocks within* $\widetilde{\mathbf{S}}$ *are functions of* k *but have been written only with subscripts. Also,* $\mathbf{S_{xx}}$ *are all functions of* $k+1$ *for* (4.38), (4.39), (4.40), (4.41), and (4.42).

Then,

$$\widetilde{\mathbf{K}}[k] = -(\widetilde{\mathbf{\Gamma}}^T\widetilde{\mathbf{S}}[k+1]\widetilde{\mathbf{\Gamma}} + \mathbf{R})^{-1}\widetilde{\mathbf{\Gamma}}^T\widetilde{\mathbf{S}}[k+1]\widetilde{\mathbf{\Phi}}$$

$$\widetilde{\mathbf{K}}[k] = \tag{4.38}$$
$$-\left[\begin{bmatrix} \mathbf{\Gamma}^T & \mathbf{0} \end{bmatrix}\begin{bmatrix} \mathbf{S}_{11} & \mathbf{S}_{12} \\ \mathbf{S}_{21} & \mathbf{S}_{22} \end{bmatrix}\begin{bmatrix} \mathbf{\Gamma} \\ \mathbf{0} \end{bmatrix} + \mathbf{R}\right]^{-1}\begin{bmatrix} \mathbf{\Gamma}^T & \mathbf{0} \end{bmatrix}\begin{bmatrix} \mathbf{S}_{11} & \mathbf{S}_{12} \\ \mathbf{S}_{21} & \mathbf{S}_{22} \end{bmatrix}\begin{bmatrix} \mathbf{\Phi} & \mathbf{0} \\ \mathbf{0} & \mathbf{F} \end{bmatrix}$$

By multiplying out the matrices, (4.38) is simplified into the equation below.

$$\widetilde{\mathbf{K}}[k] = -(\mathbf{\Gamma}^T\mathbf{S}_{11}\mathbf{\Gamma} + \mathbf{R})^{-1}\begin{bmatrix} \mathbf{\Gamma}^T\mathbf{S}_{11}\mathbf{\Phi} & \mathbf{\Gamma}^T\mathbf{S}_{12}\mathbf{F} \end{bmatrix} \tag{4.39}$$

So, the control effort is,

$$u[k] = \widetilde{\mathbf{K}}[k]\widetilde{x}[k] = -\left(\mathbf{\Gamma}^T\mathbf{S}_{11}\mathbf{\Gamma} + \mathbf{R}\right)^{-1} \begin{bmatrix} \mathbf{\Gamma}^T\mathbf{S}_{11}\mathbf{\Phi} & \mathbf{\Gamma}^T\mathbf{S}_{12}\mathbf{F} \end{bmatrix} \begin{bmatrix} x \\ x_{est} \end{bmatrix} \tag{4.40}$$

$$u[k] = -\left(\mathbf{\Gamma}^T\mathbf{S}_{11}\mathbf{\Gamma} + \mathbf{R}\right)^{-1}\mathbf{\Gamma}^T\left(\mathbf{S}_{11}\mathbf{\Phi}x + \mathbf{S}_{12}\mathbf{F}x_{est}\right) \tag{4.41}$$

$\mathbf{S}_{11}$ and $\mathbf{S}_{12}$ need to be calculated in order to find the optimal gains. As was done for the gain matrix in (4.39), the Riccati equation can also be expanded and simplified. The results of this simplification can be seen below.

$$\widetilde{\mathbf{S}}[k] = \begin{bmatrix} \mathbf{\Phi}^T(\mathbf{S}_{11} - \mathbf{S}_{11}\mathbf{\Gamma}[\mathbf{\Gamma}^T\mathbf{S}_{11}\mathbf{\Gamma} + \mathbf{R}]^{-1}\mathbf{\Gamma}^T\mathbf{S}_{11})\mathbf{\Phi} & \mathbf{\Phi}^T(\mathbf{S}_{12} - \mathbf{S}_{11}\mathbf{\Gamma}[\mathbf{\Gamma}^T\mathbf{S}_{11}\mathbf{\Gamma} + \mathbf{R}]^{-1}\mathbf{\Gamma}^T\mathbf{S}_{12})\mathbf{F} \\ \mathbf{F}^T(\mathbf{S}_{21} - \mathbf{S}_{11}\mathbf{\Gamma}[\mathbf{\Gamma}^T\mathbf{S}_{11}\mathbf{\Gamma} + \mathbf{R}]^{-1}\mathbf{\Gamma}^T\mathbf{S}_{21})\mathbf{\Phi} & \mathbf{F}^T(\mathbf{S}_{22} - \mathbf{S}_{21}\mathbf{\Gamma}[\mathbf{\Gamma}^T\mathbf{S}_{11}\mathbf{\Gamma} + \mathbf{R}]^{-1}\mathbf{\Gamma}^T\mathbf{S}_{21})\mathbf{F} \end{bmatrix} + \widetilde{\mathbf{Q}} \tag{4.42}$$

By examining index (1,1) of the matrix in (4.42), a quick substitution back to $\mathbf{P}$ using (4.22) makes the equation identical to the optimal control Riccati equation, which was calculated earlier [(4.21) and (4.23)]. So, $\mathbf{S}_{11}$ is defined as,

$$\mathbf{S}_{11}[k] \triangleq \mathbf{S}[k] \tag{4.43}$$

However, the gain matrix $\widetilde{\mathbf{K}}$ is still dependent on $\mathbf{S}_{12}$ and $\mathbf{F}$, which have not been defined or derived.

Fortunately, both of these unknown parameters can be eliminated with a single substitution. A new parameter $\mathbf{M}$ is defined as,

$$\mathbf{M}[k] \triangleq \mathbf{S}_{12}[k]x_{est}[k] \tag{4.44}$$

So that using (4.25) and (4.44), the control term (4.41) can be written as,

$$u[k] = -\Big(\mathbf{\Gamma}^T\mathbf{S}[k+1]\mathbf{\Gamma} + \mathbf{R}\Big)^{-1}\mathbf{\Gamma}^T\Big(\mathbf{S}[k+1]\mathbf{\Phi}x[k] + \mathbf{M}[k+1]\Big) \tag{4.45}$$

A simple multiplication of x_{est} will accomplish the task of obtaining the $\mathbf{M}$ term within the $\mathbf{S}_{12}$ equation.

$$\begin{aligned}
\mathbf{S}_{12}[k] = \mathbf{\Phi}^T\Big(&\mathbf{S}_{12}[k+1] - \\
&\mathbf{S}_{11}[k+1]\mathbf{\Gamma}\big(\mathbf{\Gamma}^T\mathbf{S}_{11}[k+1]\mathbf{\Gamma}+\mathbf{R}\big)^{-1}\mathbf{\Gamma}^T\mathbf{S}_{12}[k+1]\Big)\mathbf{F} - \mathbf{Q} &\quad (4.46)\\
\mathbf{S}_{12}[k]x_{est}[k] = \mathbf{\Phi}^T\Big(&\mathbf{S}_{12}[k+1]\mathbf{F}x_{est}[k] - \\
&\mathbf{S}_{11}[k+1]\mathbf{\Gamma}\big(\mathbf{\Gamma}^T\mathbf{S}_{11}[k+1]\mathbf{\Gamma}+\mathbf{R}\big)^{-1}\mathbf{\Gamma}^T\mathbf{S}_{12}[k+1]\mathbf{F}x_{est}[k]\Big) - \mathbf{Q}x_{est}[k] &\quad (4.47)\\
\mathbf{M}[k] = \mathbf{\Phi}^T\Big(&\mathbf{M}[k+1] - \\
&\mathbf{S}_{11}[k+1]\mathbf{\Gamma}\big(\mathbf{\Gamma}^T\mathbf{S}_{11}[k+1]\mathbf{\Gamma}+\mathbf{R}\big)^{-1}\mathbf{\Gamma}^T\mathbf{M}[k+1]\Big) - \mathbf{Q}x_{est}[k] &\quad (4.48)
\end{aligned}$$

The only unknown parameter of (4.48) at this point is the relationship between the desired state and desired output. This relationship can be obtained by taking a pseudo-inverse of the output equation (4.5).

$$\begin{aligned}
x &= \mathbf{L}y \\
\mathbf{L} &= \mathbf{H}^T(\mathbf{H}\mathbf{H}^T)^{-1} &\quad (4.49)\\
x_{est} &= \mathbf{L}y_{est} &\quad (4.50)
\end{aligned}$$

With the replacement of the derived unknowns ($\mathbf{S}_{11}[k] = \mathbf{S}[k]$, $x_{est} = \mathbf{L}y_{est}$), introduced parameter $\mathbf{M}$ can be written as,

$$\mathbf{M}[k] = \mathbf{\Phi}^T\Big(\mathbf{M}[k+1] - \mathbf{S}[k+1]\mathbf{\Gamma}\big(\mathbf{\Gamma}^T\mathbf{S}[k+1]\mathbf{\Gamma}+\mathbf{R}\big)^{-1}\mathbf{\Gamma}^T\mathbf{M}[k+1]\Big) - \mathbf{QL}y_{est}[k] \tag{4.51}$$

More simplification in the iteration process could be achieved by using some offline calculated parameters. First expanding $\mathbf{\Phi}$ and collecting $\mathbf{M}$, second separating some middle terms inside a curly parenthesis and taking transpose of it will result in,

$$\mathbf{M}[k] = \Big(\mathbf{\Phi}^T - \mathbf{\Phi}^T\mathbf{S}[k+1]\mathbf{\Gamma}\big(\mathbf{\Gamma}^T\mathbf{S}[k+1]\mathbf{\Gamma} + \mathbf{R}\big)^{-1}\mathbf{\Gamma}^T\Big)\mathbf{M}[k+1] - \mathbf{QL}y_{est}[k]$$
$$\mathbf{M}[k] = \Big(\mathbf{\Phi}^T - \Big\{\big(\mathbf{\Gamma}^T\mathbf{S}[k+1]\mathbf{\Gamma} + \mathbf{R}\big)^{-1}\mathbf{\Gamma}^T\mathbf{S}[k+1]\mathbf{\Phi}\Big\}^T\mathbf{\Gamma}^T\Big)\mathbf{M}[k+1] - \mathbf{QL}y_{est}[k]$$

where, $\mathbf{S}$ and $\mathbf{R}$ are symmetric matrices. Clearly, the terms inside the curly parenthesis are equal to $\mathbf{K}[k]$ defined in (4.24), finally $\mathbf{M}[k]$ is,

$$\mathbf{M}[k] = \Big(\mathbf{\Phi}^T + \mathbf{K}^T[k]\mathbf{\Gamma}^T\Big)\mathbf{M}[k+1] - \mathbf{QL}y_{est}[k] \tag{4.52}$$

Using (4.52), $\mathbf{M}$ can now be calculated iteratively in the same way as the feedback Riccatti equation using the final condition $\mathbf{M}[T] = \mathbf{0}$.

Then, the solution to the control problem defined in Section 4.5 can be summarized as

$$u[k] = -\Big(\mathbf{\Gamma}^T\mathbf{S}[k+1]\mathbf{\Gamma} + \mathbf{R}\Big)^{-1}\mathbf{\Gamma}^T\Big(\mathbf{S}[k+1]\mathbf{\Phi}x[k] + \mathbf{M}[k+1]\Big) \tag{4.53}$$

where $\mathbf{S}$ and $\mathbf{M}$ are given by the iterative equations

$$\mathbf{S}[k] = \mathbf{\Phi}^T\Big(\mathbf{S}[k+1] - \mathbf{S}[k+1]\mathbf{\Gamma}(\mathbf{\Gamma}^T\mathbf{S}[k+1]\mathbf{\Gamma} + \mathbf{R})^{-1}\mathbf{\Gamma}^T\mathbf{S}[k+1]\Big)\mathbf{\Phi} + \mathbf{Q} \tag{4.54}$$

$$\mathbf{M}[k] = \Big(\mathbf{\Phi}^T + \mathbf{K}^T[k]\mathbf{\Gamma}^T\Big)\mathbf{M}[k+1] - \mathbf{QL}y_{est}[k] \tag{4.55}$$

and $\mathbf{K}$ is

$$\mathbf{K}[k] = -\Big(\mathbf{\Gamma}^T\mathbf{S}[k+1]\mathbf{\Gamma} + \mathbf{R}\Big)^{-1}\mathbf{\Gamma}^T\mathbf{S}[k+1]\mathbf{\Phi}\ . \tag{4.56}$$

The resulting control algorithm is composed of feedback and feedforward parts which are identified, respectively, as follows:

$$u_{fb}[k] = -\Big(\mathbf{\Gamma}^T\mathbf{S}[k+1]\mathbf{\Gamma} + \mathbf{R}\Big)^{-1}\mathbf{\Gamma}^T\,\mathbf{S}[k+1]\mathbf{\Phi}x[k] \tag{4.57}$$
$$u_{ff}[k] = -\Big(\mathbf{\Gamma}^T\mathbf{S}[k+1]\mathbf{\Gamma} + \mathbf{R}\Big)^{-1}\mathbf{\Gamma}^T\,\mathbf{M}[k+1] \tag{4.58}$$

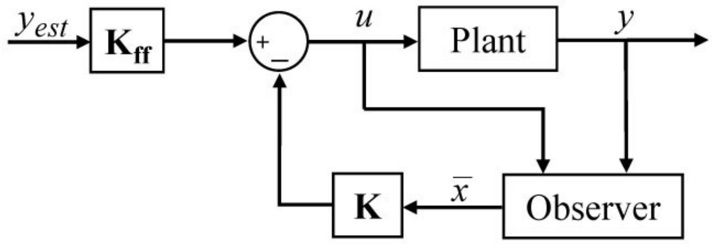

Figure 4.10: Coarse Block Diagram of MPC

such that

$$u[k] = u_{fb}[k] + u_{ff}[k] \ . \tag{4.59}$$

Parameters $\mathbf{S}$ and $\mathbf{M}$ are calculated iteratively backwards with final conditions $\mathbf{S}[T] = \mathbf{Q}$ and $\mathbf{M}[T] = 0$. The iterations are carried out for *horizon*, T, times. Every iteration corresponds to one control cycle set of gains. In effect, calculating T iterations is like calculating time varying gains up to T steps ahead even though only the gain for the current time is used. This type of control is also known as Receding Horizon Control [32], and in this framework, we call the control defined in (4.53) as the Receding Horizon Model Predictive Control (RHMPC). With every new control cycle, a new point on the desired signal is used and an old point is dropped in the gain calculation. The calculation is then repeated at every control cycle. The prediction horizon recedes as time progresses such that the furthermost point ahead of the horizon is considered to be moving one step for every control cycle.

The block diagram for this controller is shown in Figure 4.10 which is similar to that of the Pole-Placement Control algorithm (Figure A.3). The difference between two is the calculation of the gains. In RHMPC the optimal gains are calculated for a receding horizon at every control step, where in optimal control the gains are calculated once at the start. This is what separates RHMPC from optimal control.

Chapter 5

Simulation and Experimental Results

Simulations and experiments were carried out for the estimation algorithms with Receding Horizon Model Predictive Controllers as presented in the previous chapter.

In order to find a baseline performance of the estimation algorithms, a RHMPC with known future reference signal was also tested. Knowing the future reference signal for the RHMPC algorithm provides close to perfect tracking. However, using the future reference signal in heart tracking is not feasible as this makes the algorithm acasual. In this case, it was used to show the base line performance.

The horizon value, T, is one of the parameters that can be used to tune the algorithm. Even though tuned intuitively, the horizon does make a difference in the results whenever altered. A longer horizon generally results in a more accurate feedforward term, primarily because of greater foresight into the future and more iterations to calculate gains. As the horizon increases the tracking error decays exponentially. On the other hand, parameter calculations take longer. Therefore, a horizon must be chosen such that the gains can be iteratively calculated within one cycle of the control loop.

This RHMPC can handle time-varying systems and weighting matrices. For the

Table 5.1: Parameters used with the Receding Horizon Model Predictive Controller of the Test Bed System. Higher $\mathbf{Q}$ to $\mathbf{R}$ ratio is selected to accentuate the state and hence regulate more quickly.

	Axis 1	**Axis 2**	**Axis 3**
$\mathbf{Q}_1$	$5 \cdot 10^{-16} \cdot \mathbf{I}_{4\times4}$	$5 \cdot 10^{-16} \cdot \mathbf{I}_{4\times4}$	$5 \cdot 10^{-16} \cdot \mathbf{I}_{4\times4}$
$\mathbf{Q}_2$	50	30	30
$\mathbf{R}$	0.003	0.05	0.05

applications used herein, constant weighting matrices, $\mathbf{Q}_1, \mathbf{Q}_2$, and $\mathbf{R}$ (Table 5.1), and a constant horizon value, T, were used along with constant state-space models. The only true time-varying gain matrix within the algorithm was $\mathbf{M}$, which was calculated from the heartbeat data. As a result, feedforward control term (4.58) was time-varying, and $\mathbf{M}$ was calculated iteratively on the fly every control cycle.

Feedback term (4.57) was not dependent on any time-varying values. Consequently, calculated gains were constant for a given horizon. Once the horizon value was set, there was no need to calculate the feedback gains in every control cycle.

Another parameter that can be used to tune the algorithm is *the error correction function order*, p of (4.2). Here, p plays a good role in the performance of the algorithm along with the *horizon value*, T. For the optimum error/performance ratio, a 6^{th} order polynomial error correction function and a horizon value of 50 samples were selected. The experimental results of the tuning are shown in Figure 5.1.

Although, using the past heart cycle as an estimate of future reference signals would cause large errors in extended estimates, it was not a deterministic issue in this approach, since the horizon used in the RHMPC algorithm (25 ms) was relatively short compared to the heartbeat period ($\approx$ 500 ms).

The computation scheme of the feedback and the feedforward terms, and the control effort, using the derived equations, are as follows.

Offline **Step 1.** Calculate: $\mathbf{L}$ and $\underline{\mathbf{H}}$ (4.14)

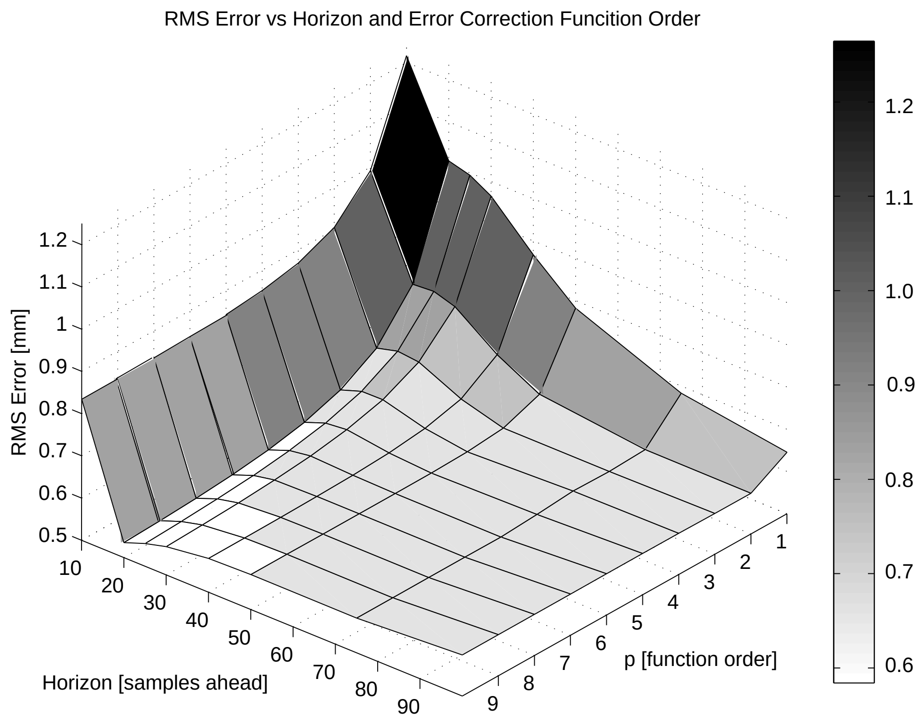

Figure 5.1: Parameter tuning for reference signal estimation: The error correction function order, p, and the horizon value, T, are tuned to get minimum RMS position error.

	Step 2.	Calculate: $\mathbf{Q}$ (4.12)
	Step 3.	Initialize: $\mathbf{P}[T] = 0$, $\mathbf{S}[T] = \mathbf{Q}$, $\mathbf{M}[T] = 0$
	Step 4.	Backwards iterate Feedback Optimal Parameters:
		$\mathbf{S}[k]$, $\mathbf{K}[k]$ for $k = T, \ldots, 1$ [(4.54), (4.56)]
Online	**Step 1.**	Generate $y_{est}[k+m]$ for $m = 0, \ldots, T$ (4.3)
	Step 2.	Backwards iterate Feedforward Optimal Parameters:
		$\mathbf{M}[k]$ for $k = T, \ldots, 1$ (4.55)
	Step 3.	Calculate: u (4.53)
	Step 4.	Goto **Online Step 1** for next k

The robot was made to follow the combined motion of heartbeat and breathing as described in Chapter 3. Separating the respiratory motion enabled better heart motion estimation. In terms of control performance, controlling the respiratory motion separately did not affect the heart tracking accuracy when the results of the combined motion tracking were compared with the pure heartbeat motion tracking results. This validates our earlier observation that heartbeat motion tracking will be the bottleneck in motion tracking and the breathing motion can be easily tracked using a pure feedback controller.

5.1 Test Bed System

In order to develop and test the algorithms, a hardware test bed system, PHANToM Premium 1.5A, was used and modeled. In Figure 5.2 the degrees of freedom and the zero configuration of the manipulator are shown. In modeling, experimental transfer function models for the three principle axes were determined. The produced mathematical models were tested for controllability and observability. It was found that all three axes were uncontrollable and unobservable. This would cause poor conditioning of the state space matrices, hence instability and poor control.

Reduced realizations were obtained using Schur balanced model reduction [44]. With this reduction, the weakly controllable eigenvalues are eliminated to produce a new system. New system models were better conditioned, as well as fully controllable and observable. For detailed derivation of the mathematical modeling of the PHANToM robot, see [45] (axes transfer functions and their frequency response plots are given in Appendix B). Also, the friction forces acting on the joints were modeled experimentally according to Coulomb friction model.

The dynamic equations for the phantom are in the form:

$$\mathbf{M}_p(\theta)\ddot{\theta} + \mathbf{C}_p(\dot{\theta}, \theta)\dot{\theta} + \mathbf{N}_p(\theta) = \tau \tag{5.1}$$

where $\theta = [\theta_1\ \theta_2\ \theta_3]^T \in \mathbb{R}^3$, $\mathbf{M}_p$ is the inertia matrix, $\mathbf{C}_p$ is the Coriolis matrix of the manipulator, $\mathbf{N}_p$ includes the gravitational and other forces−such as friction−that acts on the joints, and τ is the vector of actuator torques. The nonlinearities of the system were overcome by adding the torque that was required against the gravitational effects, $\mathbf{N}_p$, and Coriolis and centrifugal forces, $\mathbf{C}_p(\dot{\theta}, \theta)\dot{\theta}$ according to the derived dynamics. The added $\mathbf{C}_p(\dot{\theta}, \theta)\dot{\theta}$ term was considerably smaller than the applied torque, which is due to the quadratic dependence of this term on the joint velocities.

The PHANToM robot possesses characteristics similar to an actual surgery robot. Its lightweight links, low inertia design and low friction actuation system allows sufficient motion and speed abilities for tracking the heartbeat signal. In the experimental setup, the control algorithms were executed on a PC equipped with a 2.33 GHz Dual-Core Intel Xeon 5140 processor running MATLAB xPC Target v3.3 real-time kernel with a sampling time of 0.5 ms. PHANToM Premium does not come with a built-in homing option. In order to improve the accuracy of the experiments, before every experiment, the robot was brought to a selected home position, in this case the zero configuration of the manipulator (Figure 5.2-*Right*), where the tracking was started.

In order to attain pure heartbeat and respiratory motion data from the raw data, two lowpass filters are used as shown in Figure 3.1. Second and tenth order Chebyshev Type II IIR filters with cutoff frequencies at 26 Hz and 1 Hz were used, respectively. The second order filter was used to remove high frequency components (above 26 Hz) of the data. The RMS error in between the filtered position and the measured position is 0.528 mm when the filtering was performed online.

In the experiments, prerecorded heart motion signal and ECG signal were used. Overall, three sets of experiments were conducted. The first set of the experiments was conducted using offline filtered heartbeat and breathing motion data which were re-sampled using the raw heart position data from 257 Hz to 2 kHz by cubic interpolation. Zero group delay was introduced since the data was processed offline. The second set of the experiments was conducted using raw heart position data sampled

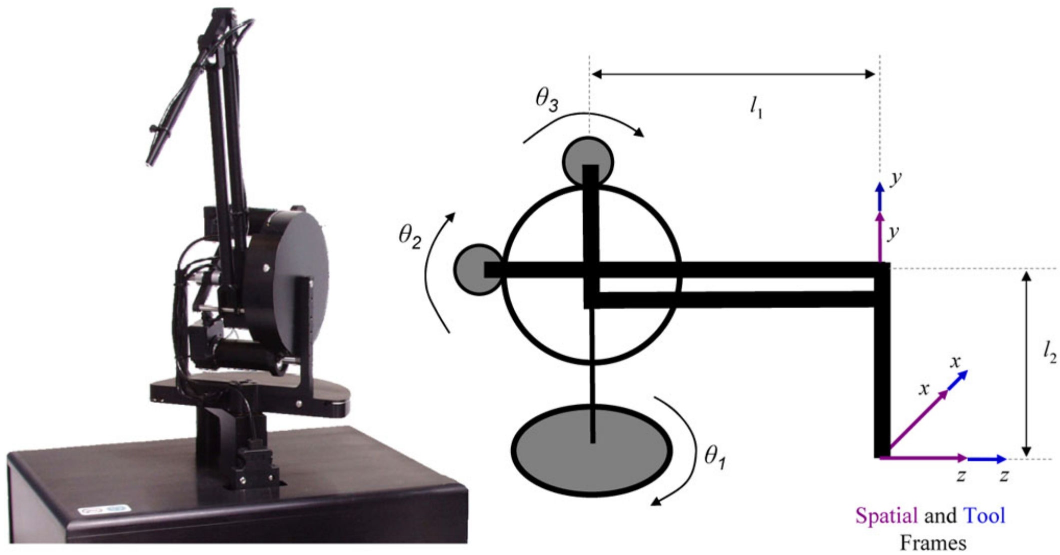

Figure 5.2: *Left*: PHANToM Premium 1.5A. *Right*: PHANToM's zero configuration.

at 257 Hz. Filtering operations were performed online to attain pure heartbeat and breathing motions. The filtered data were extrapolated online to be used with the control algorithms that run at 2 kHz. The third set of experiments was conducted using re-sampled raw heart position data from 257 Hz to 2 kHz. Similar to the second set, filtering operations were performed online to attain pure heartbeat and breathing motions to be used in the control algorithms.

5.2 Experimental Results

In both simulations and experiments, the same methods and reference data were used. Some slight differences in parameters were observed due to the mathematical modeling of the robot. To validate the algorithms effectiveness, first 10 s of the 56-s long data was used to tune the control parameters. Then, the experiments were carried out using the 56-s long heart data.

Matrix weighting parameters of the optimal index were tuned to minimize RMS tracking error. Parameters were selected in order to accentuate the states and hence regulate more quickly, with higher control efforts. Tuning was performed to avoid the high frequency resonances so that no vibration would be reflected to the structure.

For each case, experiments on PHANToM robot were repeated 10 times. It was noted that the deviations between the trials are very small. Among these results, the maximum values for the *End-effector RMS and Maximum Position Errors* in 3D and *RMS Control Effort* are summarized in Tables 5.2, 5.3 and 5.4 to project the worst cases.

Results of Receding Horizon Model Predictive Control with Reference Signal Estimation using ECG signal for each axis are shown in Figures 5.3, 5.4, and 5.5. Low frequency respiratory motion is noticeable at the Figures 5.3-A, 5.4-A, and 5.5-A. All three axes of the PHANToM demonstrated similar performance. It is believed that the maximum error values are affected from the noise in the data collected by sonomicrometric sensor. Although high-frequency parts of the raw data were filtered out, relatively low "high frequency" components stayed intact. It is unlikely that the POI on the heart is capable of moving 5 mm in a few milliseconds. The measured data has velocity peaks that are over 13 times faster than the maximum LAD velocity measurements reported by Shechter *et al.* [46]. Heavy filtering should have been performed to delete the high frequency motions, but they were kept, as currently we do not have an independent set of sensor measurements (such as from a vision sensor) that would validate this conjecture. This also gives a conservative measurement of the performance of the system.

5.3 Discussion of the Results

The parameters were tuned using the first 10 s of the data and validated with the 56 s data. There was less improvement in the RMS error when the 56 s data was used (see the underlined elements in Table 6.1). This is because the heartbeat period variability was larger in the first 10 s segment of the data. The mean of the heartbeat

Table 5.2: End-effector Simulation and Experimental Results: *Summary of the end-effector RMS position error, max position error (in parenthesis) and RMS control effort values for the control algorithms used with 10- and 56-s data. Heartbeat and breathing motions were filtered offline. Some of the experimental results are underlined to point out the effect of biological signal on the estimation. There was a noticeable improvement with 56-s data because the heartbeat period change was larger in the first 10-s segment of the data.*

End-effector Tracking Results	RMS Position Error [mm] (Max Position Error) [mm]				RMS Control Effort [Nmm]			
	10 s		56 s		10 s		56 s	
	Simulation	PHANToM	Simulation	PHANToM	Simulation	PHANToM	Simulation	PHANToM
Receding Horizon MPC with Exact Reference Information	0.302 (1.539)	0.284 (1.945)	0.295 (1.732)	0.277 (2.066)	14.4	48.6	14.8	46.9
Receding Horizon MPC with Reference Signal Estimation	0.718 (2.828)	<u>0.909</u> (4.394)	0.726 (3.826)	<u>0.906</u> (5.958)	18.5	74.8	17.6	66.5
Receding Horizon MPC with Reference Signal Estimation using ECG Signal	0.524 (2.761)	<u>0.669</u> (4.308)	0.533 (3.066)	<u>0.682</u> (4.921)	16.5	56.9	16.3	55.9

Table 5.3: End-effector Simulation and Experimental Results: *Summary of the end-effector RMS position error, max position error (in parenthesis) and RMS control effort values for the control algorithms used with 10- and 56-s data. Heartbeat and breathing motions were filtered online from the prerecorded 256.9 Hz motion data. Some of the experimental results are underlined to point out the effect of biological signal on the estimation. There was a noticeable improvement with 56-s data because the heartbeat period change was larger in the first 10-s segment of the data.*

End-effector Tracking Results	RMS Position Error [mm] (Max Position Error) [mm]				RMS Control Effort [Nmm]			
	10 s		56 s		10 s		56 s	
	Simulation	PHANToM	Simulation	PHANToM	Simulation	PHANToM	Simulation	PHANToM
Receding Horizon MPC with Exact Reference Information	0.282 (1.448)	0.385 (3.705)	0.280 (1.801)	0.375 (3.714)	31.8	57.9	31.5	54.7
Receding Horizon MPC with Reference Signal Estimation	0.644 (2.966)	<u>0.821</u> (4.730)	0.660 (4.290)	<u>0.832</u> (6.431)	36.4	74.0	36.6	71.6
Receding Horizon MPC with Reference Signal Estimation using ECG Signal	0.502 (2.930)	<u>0.709</u> (4.959)	0.520 (3.833)	<u>0.726</u> (5.825)	34.7	69.1	35.6	70.2

Table 5.4: End-effector Simulation and Experimental Results: *Summary of the end-effector RMS position error, max position error (in parenthesis) and RMS control effort values for the control algorithms used with 10- and 56-s data. Heartbeat and breathing motions were filtered online from the interpolated 2055.5 Hz motion data. Some of the experimental results are underlined to point out the effect of biological signal on the estimation. There was a noticeable improvement with 56-s data because the heartbeat period change was larger in the first 10-s segment of the data.*

End-effector Tracking Results	RMS Position Error [mm] (Max Position Error) [mm]				RMS Control Effort [Nmm]			
	10 s		56 s		10 s		56 s	
	Simulation	PHANToM	Simulation	PHANToM	Simulation	PHANToM	Simulation	PHANToM
Receding Horizon MPC with Exact Reference Information	0.276 (1.267)	0.372 (3.661)	0.275 (1.610)	0.362 (3.683)	17.1	59.5	17.1	56.0
Receding Horizon MPC with Reference Signal Estimation	0.640 (2.811)	<u>0.815</u> (4.473)	0.656 (3.208)	<u>0.825</u> (6.239)	22.5	69.7	21.6	64.8
Receding Horizon MPC with Reference Signal Estimation using ECG Signal	0.491 (2.748)	<u>0.669</u> (4.453)	0.503 (2.896)	<u>0.681</u> (5.569)	19.4	61.8	19.5	59.8

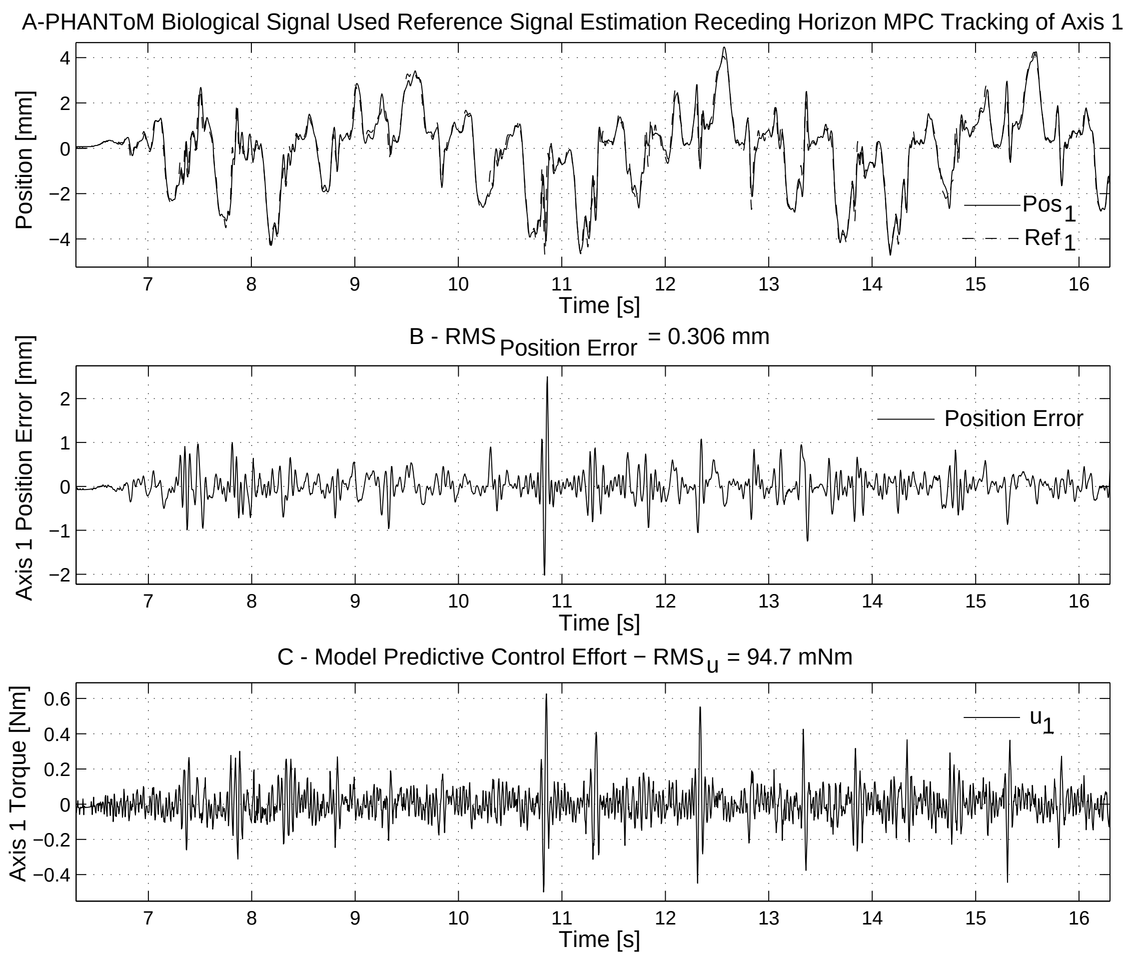

Figure 5.3: PHANToM 1^{st} axis results for Receding Horizon MPC with Reference Estimation using ECG Signal. **A**-Reference and Position, **B**-Position Error, and **C**-Control Effort signals are shown.

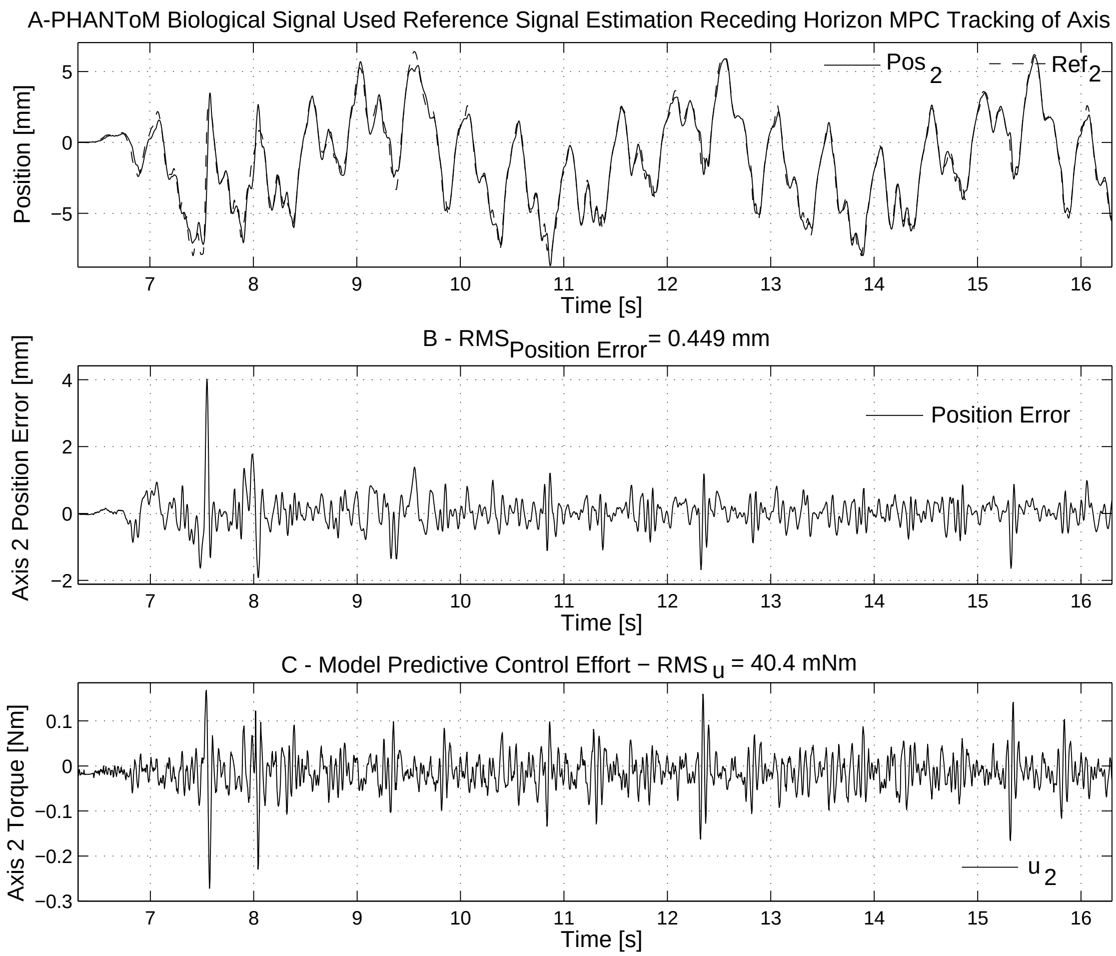

Figure 5.4: PHANToM 2^{nd} axis results for Receding Horizon MPC with Reference Estimation using ECG Signal. **A**-Reference and Position, **B**-Position Error, and **C**-Control Effort signals are shown.

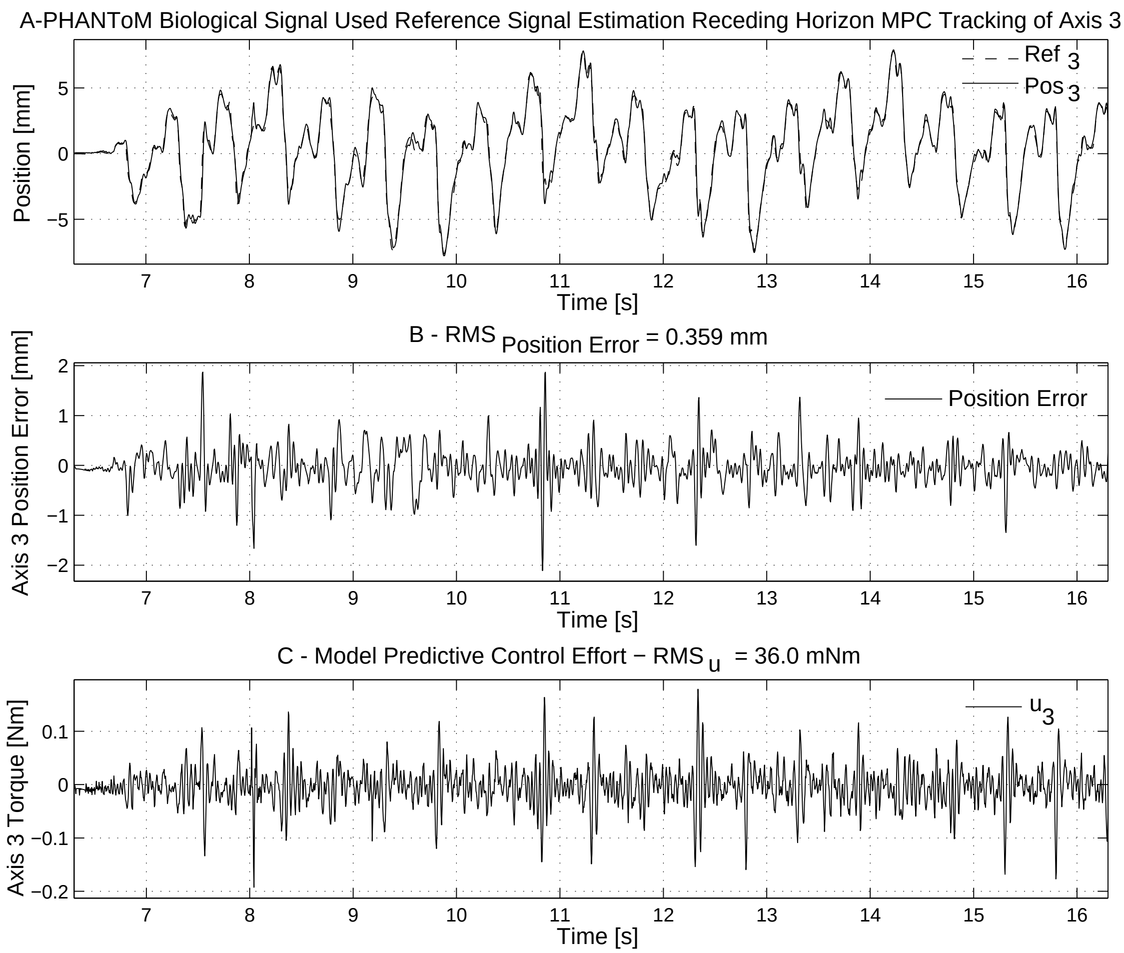

Figure 5.5: PHANToM 3^{rd} axis results for Receding Horizon MPC with Reference Estimation using ECG Signal. **A**-Reference and Position, **B**-Position Error, and **C**-Control Effort signals are shown.

period change was 9.3 μs for the first 10 s segment of the data and 1.6 μs for the overall data. As a result, the effect of the biological signal on the signal estimation, therefore on the tracking error, was more pronounced in the first 10 s of the data.

If we compare the results of the algorithms with each other, as expected, the RHMPC with Reference Signal Estimation Using Biological Signals algorithm outperformed the RHMPC with Reference Signal Estimation algorithm. Results proved that by using ECG signal in the motion estimation, heart position tracking was not only improved but also became more robust. The system was more responsive to sudden changes in the heart motion with the addition of ECG signal, accordingly the variance of the error distribution decreased by half. One-way ANOVA was used to test the statistical significance of the results and they were found to be significantly different ($F(1, 38) = 6809,\ p < 0.001$). These tracking results are 2.5 times better than the best results in literature that is reported by Ginhoux *et al.* [24]. Comparing the results of the predictive algorithms with the baseline performance results shows that there is still room for improving the estimation algorithm. It is important to note that the results also need to be validated *in vivo*, which was the case in [24].

Three different sets of experiments were conducted in order to test the effects of filtering and the sensor sampling. Filtering effects (i.e. group delay) were minimized by using low order filters. Although small increases in the RMS errors were noticed, online filtering of the raw data was successful. The experiment results given in Tables 5.3 and 5.4 were prepared to demonstrate the performance difference of the system with different sensor sampling rate. The decrease in the RMS errors in all control algorithms demonstrates the performance improvement of the robotic system with higher sensor sampling rates. This shows the importance of the sensor system in the robotic assisted beating heart surgery.

Chapter 6

Three Dimensional Heart Position Measurement: Whisker Sensor Design

This thesis aims to develop telerobotic tools to actively track and cancel the relative motion between the surgical instruments and the heart by Active Relative Motion Canceling (ARMC) algorithms, which will allow coronary artery bypass graft (CABG) surgeries to be performed on a stabilized view of the beating heart with the technical convenience of on-pump procedures.

In this chapter, design and characterization of a novel whisker-like sensor that is capable of measuring the position in three dimensions (3D) are discussed.

The whisker sensor is a flexible, high precision, high bandwidth contact sensor designed for measuring biological motion of soft tissue for medical robotics applications. Low stiffness of the sensor prevents damage on the tissue during its contact. Two different designs are described: one for measuring large displacements and the other for small displacements. Simulation and measurement results from prototype of both designs are reported.

Physiological motions are measured and actively compensated during robotic-assisted medical interventions to improve the accuracy of the surgery [18–20, 23, 24, 47, 48]. The sensors for measuring the physiological motion of the target tissue is a critical component of the overall robotic system. In this thesis a whisker-like three-dimensional, high precision, high bandwidth, flexible contact position sensor is proposed for measuring the physiological motion of the body in medical robotics applications. The proposed highly sensitive sensor equipped with micro strain gauges comes out from the tip of a manipulator and touches the tissue or skin surface. It can be in continuous contact with the point of interest, in contrast to other available sensors for measuring biological motion. Its high precision and high resolution enables the robotic system to actively compensate for the relative motion between the surgical site and the surgical instruments.

6.1 System Concept and Use of Sensors

In robotic tele-surgery conventional surgical tools are replaced with robotic instruments which are under direct control of the surgeon through teleoperation. During off-pump CABG surgery, the robot arm and the robotic surgical instruments track the heart and breathing motion, which are the main sources of the physiological motions observed. The relative motion between the surgical site and the surgical instruments is canceled. As a result, the surgeon operates on the heart as if it were stationary, while the robotic system actively compensates for the relative motion of the heart. Measurement of heart motion with high precision and high confidence is required for precise motion canceling performance. Also, redundant sensing systems are desirable for safety reasons.

Earlier studies in canceling beating motion with robotic-assisted tools used vision based and ultrasound based sensory systems to measure heart motion. Nakamura *et al.* [18] tracked heart motion with a 4-DOF robot using a vision system. The tracking error due to the camera feedback system was relatively large (error in the order of few millimeters in the normal direction) to perform beating heart surgery. Thakral *et al.* [19] used a laser range finder system to measure one-dimensional motion of a rat's heart. Groeger *et al.* [20] used a two-camera computer vision system to measure local motion of heart and performed analysis of measured trajectories, and Koransky *et al.* [21] studied the stabilization of coronary artery motion afforded by passive cardiac stabilizers using three-dimensional digital sonomicrometry. Hoff *et al.* [49] measured the beating heart motion in three dimensions using two 2-axis accelerometers, showing that acceleration measurements can reveal patterns that may be an indication of heart circulation failure. Ortmaier *et al.* [23] and Ginhoux *et al.* [24] also used camera systems to measure motion of the heart surface for their estimation algorithms. Cavusoglu *et al.* [50] used a sonomicrometric system to collect heart motion data from an adult porcine and showed the feasibility of a robotic system performing off-pump coronary artery bypass grafting surgery. Vitrani *et al.* [51] used ultrasound-based visual imaging to guide a surgical instrument within the heart during surgery. Bader *et al.* [52] estimated a portion of organ surface motion using a pulsating membrane model with a stereo vision system. The model was used to estimate the periodic organ motion when the camera view is occluded. Noce *et al.* [53] simulated a method that characterizes heart surface texture to detect heart motion with recorded sequences by a monocular vision system.

The experimental results indicate that vision sensors were not satisfactory for tracking in beating heart surgery. Vision systems have problems with noise and occlusions. Noise can be reduced by using fluorescent markers, but the occlusion problem remains significant, and is an important setback, especially during surgical manipulations. Although some research was directed towards estimating heart motion when the image was occluded [23, 52], a sensor that provides persistent position information is necessary for satisfactory tracking, i.e., a continuous contacting position sensor. Also the resolution of a vision system is restricted, depending on the camera quality and distance to the point of interest. Vision sensors can provide high precision measurements in tangential directions, but their precision is low in the normal direction.

Inertial sensors are not suitable for stand-alone use in position measurements, due to drift problems. Laser proximity sensors are limited to one dimensional measurement and cannot provide any information about tangential motion of the heart surface. Cagneau *et al.* [47] used a force sensor equipped robot designed for minimally invasive surgery in [54] to compensate for physiological motions in surgical tasks involving tissue contact. However the proposed force feedback controller did not perform effective motion compensation.

A sensor that is in continuous contact with tissue is necessary for satisfactory tracking. The continuous contact sensors used in measuring the heart motion in the current literature are limited to sonomicrometer. A sonomicrometric position sensor has been the sensor of choice in the earlier studies of this research, but obtaining precise position measurements is essential in closed loop control for tracking the beating heart. Although sonomicrometric sensors are very accurate, they contain noise from ultrasound echoes. Also, they are more prone to error in calibration between the base sensors and the robotic manipulator coordinate frame.

The whisker sensor that is introduced in this study is a high sensitivity, flexible, three-dimensional position sensor equipped with micro strain gauges. Because of the sensor's resemblance to projecting hairs or bristles, which come out from the tip of the surgical manipulator and touch the heart surface, the sensor is called a whisker sensor. Sensors for different scopes were developed within the general whisker sensor description given above. Berkelman *et al.* [55] designed a miniature force sensor with strain gauges to measure forces in three dimensions at the tip of a microsurgical instrument. Two sets of crossed beams are used as the elastic elements of the force sensor. Scholz and Rahn [56] used an actuated whisker sensor to determine the contacted object profiles for underwater vehicles. This whisker sensor predicted contact point based on the measured hub forces and torques with planar elastica model. Solomon and Hartmann [57] used artificial whiskers to sense the profile of three-dimensional objects. They used an array of flexible steel wires fixed to bases equipped with four strain gauges to measure the two orthogonal components of the base moment. From the rate of change of moment, they calculated the radial contact distance and constructed the detected object's profile.

The next section focuses on the mechanical design of the proposed whisker sensor.

6.2 Whisker Sensor Design

The scope of this study is to create a miniature whisker sensor to measure the position of point of interest on the tissue or skin during medical interventions. Physically a whisker sensor is a long thin, and flexible extension used to detect the surrounding objects as well as their position, orientation and profiles. Design limitations include size constraints to make the tool usable in minimally invasive operations. The resolution of the sensor needs to be in the range of 50 μm in order to track the beating heart using the control algorithm described in Chapter 3.2. In this section two whisker sensor designs are proposed to be used in two different scenarios.

Design 1 employs a linear position sensor connected to two flexible cantilever beams that are attached orthogonally with a ridged joint. The one dimensional linear motion along the normal dimension of the tip is measured with the linear position sensor and the two dimensional lateral motion of the tip is measured with strain gauge sensors placed on the beams by separating the motion into its two orthogonal components (Figure 6.1). These kind of beam designs are used in flexure joint

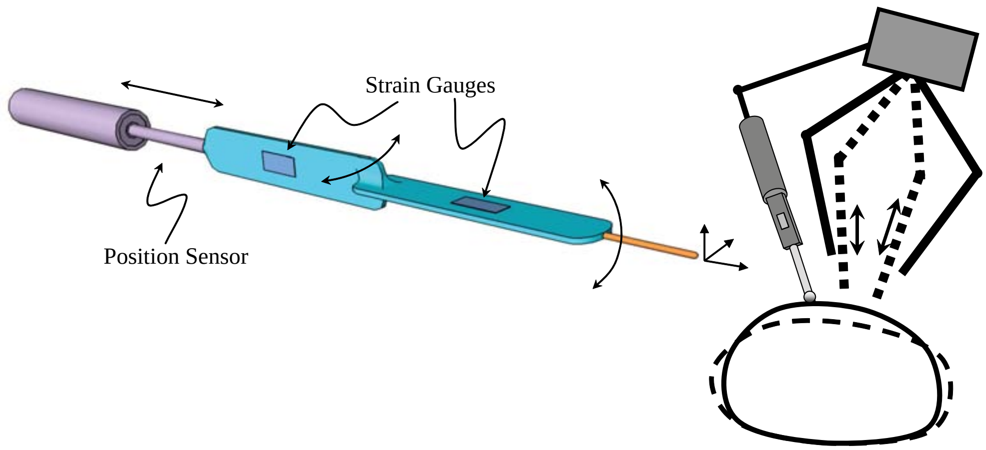

Figure 6.1: Whisker Sensor Design 1. *Left*: One linear position sensor and two orthogonally placed flexure beams with strain gauges are used to measure the three-dimensional position of the sensor tip. *Right*: Sensor is attached to the manipulator base to provide continuous contact even when the surgical tools are not in close proximity, and to measure the heart position.

mechanisms [58]. The design shown in Figure 6.1 can be attached to the robotic manipulator base to provide continuous contact. Even though the surgical tools are not in close proximity to the heart the sensor is capable of measuring the biological motion. The operation range of the sensor is adjusted to fit the heart motion, 12 mm peak to peak max displacement [50].

Design 2 employs a cross shaped flexible structure at the back of the linear sensor, which allows the lateral motion on the tip to be measured by the strain in the legs of the cross structure (Figure 6.2). A similar cross-shaped structure design was used by Berkelman [55] to measure force/torque values of the sensor tip. One major difference is the higher stiffness of their design, which was intended for force sensing. In the second design, a smaller linear position sensor with a spring loaded coil is used since a smaller operation range of 5 mm in each direction is aimed. Cross shaped whisker sensor design is manufactured in relatively smaller dimensions and it is planned to be used with the system in a slightly different way as a result of its smaller size. The sensor will be attached to the surgical tool to measure the displacement between heart

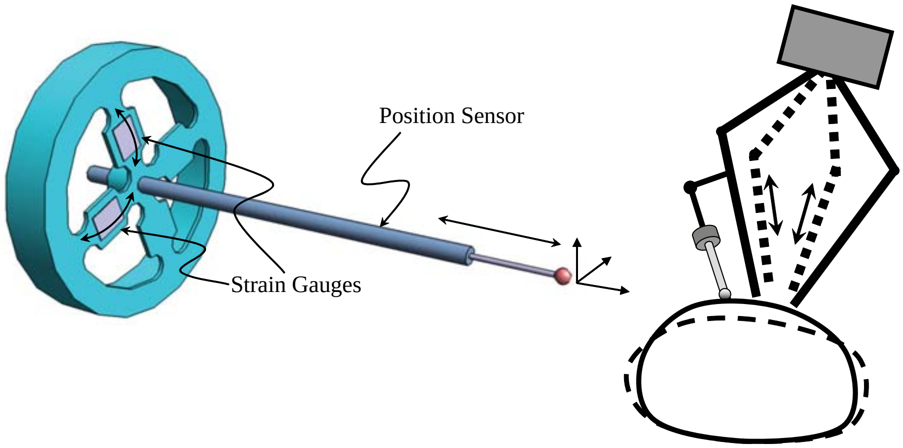

Figure 6.2: Whisker Sensor Design 2. *Left*: One linear position sensor and a cross (×) shaped flexible structure with strain gauges are used to measure the three-dimensional position of the sensor tip. *Right*: Sensor is attached to the robot arm to measure the displacement between the heart and the surgical tools.

and surgical tools. This will bring more dexterity to the system, since the sensor base moves with the surgical tool.

Both of the proposed whisker sensor designs use a one axis linear position sensing element (i.e., a Linear Variable Displacement Transducer) and a two axes flexure strain gauge position sensor. The reason for using linear position sensors to measure the motion in the normal direction of the sensor is to provide low stiffness. The positions in the lateral axes are to be measured with strain gauges attached to flexure beams. Due to both designs' technological similarities, the same data acquisition system and similar models can be used to calculate the position of the sensor tip with respect to the sensor base. As mentioned earlier, similar geometrical designs are used in flexural joint mechanism designs [58]. Flexural joints are preferred because of the absence of friction and backlash. A drawback of the flexural elements is their limited deflection, which needs to be taken in to consideration.

Note that, due to the constraints of minimally invasive surgery, both of these designs will have to be fitted inside a narrow cylindrical volume. The sensor design shown in Figure 6.1 is relatively bigger in size with respect to the one shown in

Figure 6.2 since the linear transducer needs to support the flexure beams holding the strain sensors. This necessity for support requires a structurally stronger therefore bigger linear sensor. However, smaller linear sensors can be used in the design shown in Figure 6.2.

Equipment

As mentioned earlier, both designs require a one axis contactless linear position sensing element, and a two axes flexure beam strain gauge position sensing element. The following equipment were used to build prototype sensors.

Linear Position Sensor

MicroStrain 24 mm stroke Subminiature Differential Variable Reluctance Transducer (DVRT−or half bridge LVDT) was used for the measuring the displacement in the normal direction in Design 1. The sensor casing is 4.77 mm in diameter and sensor length is 132 mm at its maximum stroke. Resolution of the transducer is 5.7 μm with $\pm$ 1 μm repeatability.

MicroStrain 9 mm stroke Micro gauging DVRT with internal spring and bearings was used to measure the displacement in the normal direction in Design 2. Sensor casing is 1.80 mm in diameter and sensor's uncoiled length is 61 mm. Resolution of the transducer is 4.5 μm with $\pm$ 1 μm repeatability. Both sensors' response bandwidth is 7 kHz.

Strain Gauges

Kyowa KFG-5-120-C1-11L1M2R type strain gauges with nominal resistance value, $R_G = 119.6 \pm 0.4\ \Omega$ and gauge factor, $GF = 2.11 \pm 0.4$ are used with Design 1. Strain gauges are bonded with Instant Krazy Glue (Elmer's & Toagosei Company).

In Design 2 Micron Instruments SS-060-033-500PU-S4, semiconductor type strain

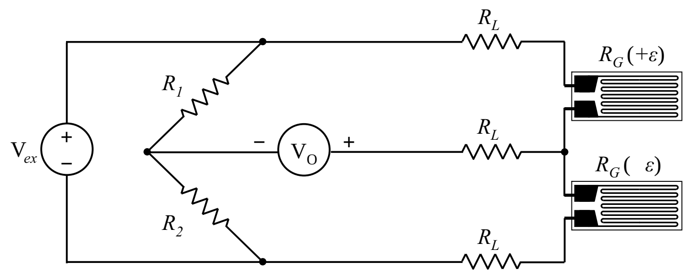

Figure 6.3: Half Wheatstone Bridge Circuit: R_1 and R_2 are bridge completion resistors, R_L is the lead resistance and R_G is the nominal resistance of the strain gauges. V_{ex} is the excitation voltage and V_O is the measured output.

gauges with nominal resistance value, $R_G = 540 \pm 50\ \Omega$ and gauge factor, $GF = 140 \pm 10$ are used. Strain gauges are bonded with Vishay Micro-measurement M-Bond 600 Adhesive Kit (M-Line Accessories Measurement Group) [59, 60].

Signal Conditioning Equipment

National Instruments PCI-6023E 12-Bit Multifunction DAQ Board, SCXI-1121 4-Channel Isolation Amplifier and SCXI-1321 Offset-Null and Shunt-Calibration Terminal Block were used to acquire strain gauge and LVDT measurements.

SCXI-1121 module has 4 channel input with internal half-bridge completion. Module was configured for a voltage excitation, V_{ex}, of 3.333 V. Input gains were adjusted to 1000 for Kyowa strain gauges and 10 for Micron Instruments strain gauges.

Strain Calculations

In order to minimize the effect of temperature changes and increase the sensitivity of the circuit, half-bridge configurations are used to measure strains. Strain, ε, for the half-bridge configuration given in Figure 6.3 is

$$\varepsilon = \frac{-2 \cdot (V_O - V_{O_{unstd}})}{GF \cdot V_{ex}} \cdot \left(1 + \frac{R_L}{R_G}\right) , \tag{6.1}$$

where V_O is the measured output when the beam is deflected (strained), $V_{O_{unstd}}$ is the initial, unstrained measurement and V_{ex} is the excitation voltage [61]. $V_{O_{unstd}}$ is adjusted to 0 V by offset nulling beforehand. Offset nulling circuitry is used to rebalance the bridge; it also eliminates the effects of lead resistance.

If R_G, R_L, GF and V_{ex} values are substituted into (6.1), the final strain equations for the sensor designs are

$$Design\ 1: \quad \varepsilon = -0.2905 \cdot V_O, \tag{6.2}$$

$$Design\ 2: \quad \varepsilon = -0.0043 \cdot V_O. \tag{6.3}$$

6.3 Mechanics of the Flexure Beams

Using the strain values calculated in the Section 6.2, the position change of the tip of the sensor, (x_{tip}, y_{tip}), can be found using basic mechanics of materials [62]. The following assumptions are made to model the mechanics:

1. The gravitational effects on the beam are negligible.

2. The deflection of the beam is in the elastic range.

3. The square of the slope of the beam, $\left(\frac{dy}{dx}\right)^2$, is negligible compared to unity, where $y = f(x)$ is the elastic curve.

4. The beam deflection due to shearing stress is negligible (a plane section is assumed to remain plane).

5. Young's modulus, E, and the second moment of the cross sectional area, I, values remain constant for any interval along the beam.

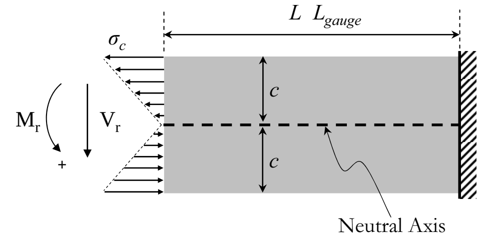

Figure 6.4: Beam section forces and stresses at strain gauge position. σ_c is the normal stress acting on the surface of the transverse cross section. M_r is the resisting moment and V_r is the resiting shear force.

Mechanics of the Cantilever Beam

The motion in the lateral plane of the flexure beams will cause two bending moments, M_x and M_y, in the sensor body. Bending moments can be calculated using the strain values, ε_x and ε_y, measured from the gauges attached on the cantilever beams. The strain and stress relation can be defined for linear elastic action with Hooke's law:

$$\sigma_x = E \cdot \varepsilon_x \tag{6.4}$$

where σ_x is the normal stress on a cross sectional plane and ε_x is the longitudinal strain. The normal stress will be maximum at the surface farthest from the neutral axis ($\sigma_{max} = \sigma_c$ at $y = c$ and c is half of the beam thickness, d). The normal stress at the surface, σ_c (Figure 6.4), can be calculated from the strain measurement of the surface using Hooke's Law as given in (6.4).

For the cantilever beam design, resisting moment at supported end is given as

$$M_r = -\frac{\sigma_c \cdot I}{c} = -\frac{\varepsilon_c \cdot E \cdot I}{c} \ . \tag{6.5}$$

The resisting moment acting at the point of strain gauge can be calculated using

$$M_r(L_{gauge}) = P \cdot L_{gauge} \ , \tag{6.6}$$

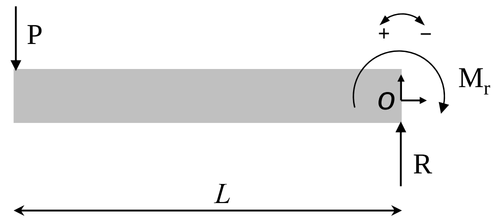

Figure 6.5: Free body diagram of the cantilever beam. R is the reaction force at the supported end, M_r is the resisting moment and P is the bending force.

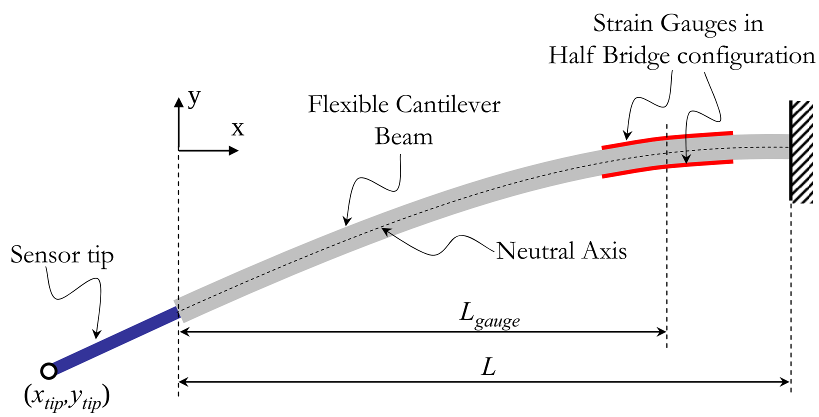

Figure 6.6: Deflected Cantilever Beam

where P is the force acting on the unsupported end of the beam (Figure 6.5). Then, (6.5) can be rewritten as

$$P = -\frac{\varepsilon_c \cdot E \cdot I}{L_{gauge} \cdot c} \ . \tag{6.7}$$

During straight beam loading in an elastic action, the centroidal axis of the beam forms a curve defined as the elastic curve, $y = f(x)$.

In small portions of the beam with constant bending moment, the elastic curve is an arc of circle with radius ρ. Using Hooke's law and geometry radius of curvature of the neutral axis can be derived as

$$\frac{1}{\rho} = \frac{M}{E \cdot I} \tag{6.8}$$

where M is the bending moment. The curvature along the beam can be simplified using assumption 3 as

$$\frac{1}{\rho} = \frac{\frac{d^2y}{dx^2}}{\left[1 + \left(\frac{dy}{dx}\right)^2\right]^{\frac{3}{2}}} = \frac{d^2y}{dx^2} \ . \tag{6.9}$$

Combining (6.8) and (6.9), the differential equation for the elastic curve of the beam is

$$M(x) = E \cdot I \cdot \frac{d^2y}{dx^2} \tag{6.10}$$

where the moment, $M(x)$ is a function of x,

$$M(x) = P \cdot x \quad , \quad 0 \leq x \leq L \ . \tag{6.11}$$

If (6.10) is integrated twice, elastic curve can be derived. The beam's end point deflection, $y = 0$ at $x = L$, and end point slope, $\frac{dy}{dx} = 0$ at $x = L$, can be used as boundary conditions for the integration. Then, (6.10) can be written as

$$E \cdot I \cdot \frac{d^2y}{dx^2} = P \cdot x \quad . \tag{6.12}$$

Integrating twice will result in

$$E \cdot I \cdot y = \frac{P \cdot x^3}{6} + C_1 \cdot x + C_2 \tag{6.13}$$

where

$$C_1 = -\frac{P \cdot L^2}{2} \ , \quad C_2 = \frac{P \cdot L^3}{3}. \tag{6.14}$$

Deflection curve and slope on the beam are given respectively as

$$y = -\frac{\varepsilon}{3 \cdot d \cdot L_{gauge}} \cdot (x^3 - 3 \cdot L^2 \cdot x + 2 \cdot L^3) \tag{6.15}$$

$$\frac{dy}{dx} = -\frac{\varepsilon}{d \cdot L_{gauge}} \cdot (x^2 - L^2) \ . \tag{6.16}$$

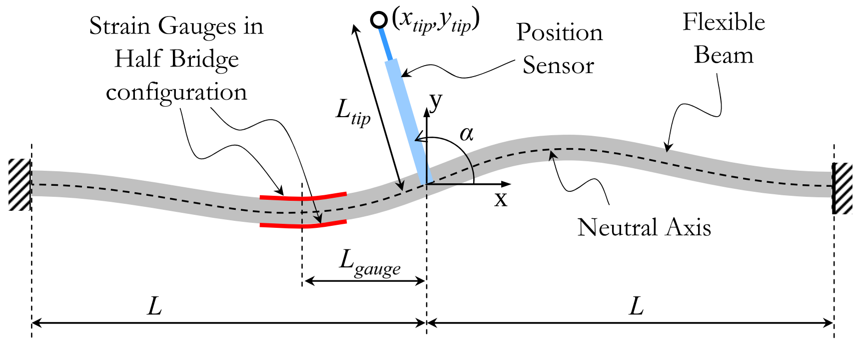

Figure 6.7: Deflected Cross Beam Section

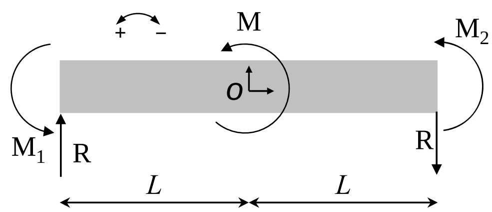

Figure 6.8: Free body diagram of the cross beam section. R is the reaction force at the supported ends, M is the bending moment. M_1 and M_2 are the reaction moments at the supported ends.

Then, the slope of the tangent line at the end point of the cantilever beam ($x = 0$) is

$$\left.\frac{dy}{dx}\right|_{x=0} = \frac{\varepsilon \cdot L^2}{d \cdot L_{gauge}} \ . \tag{6.17}$$

It is assumed that tool tip has high modulus of elasticity (rigid) and its deflection is negligible. Therefore its contact position can be calculated using the following line equation.

$$y_{tip} = \left(\frac{\varepsilon \cdot L^2}{3 \cdot d \cdot L_{gauge}}\right) \cdot (3 \cdot x_{tip} - 2 \cdot L) \tag{6.18}$$

Mechanics of the Cross Beam

Similar derivation methods can be used in this design. Motion of the position sensor tip in the lateral plane would cause two bending moments, M_x and M_y, on the cross flexure structure. Bending moments can be calculated using the strain values, ε_x and

ε_y. Slope between the position sensor and the resting plane of the cross beam can be calculated using the measured strain.

Simplified free body diagram of the cross flexure section is shown in Figure 6.8. A relation between reaction forces and bending moment can be written as

$$R = \frac{3\ M}{4\ L}\ , \tag{6.19}$$

where R is reaction force at the supporting ends. Then, the resisting moment, M_r, acting at the point of the strain gauge is

$$M_r(-L_{gauge}) = \frac{M\ (2L - 3L_{gauge})}{4L}\ . \tag{6.20}$$

Using (6.5) and (6.20), the bending moment can be calculated as

$$M = -\frac{8\ \varepsilon_c EIL}{d(2L - 3L_{gauge})}\ . \tag{6.21}$$

The moment distribution on the beam with respect to position can be derived as

$$M(x) = \frac{M\ (3x + 2L)}{4L}\ , \qquad -L \leq x \leq 0^- \tag{6.22a}$$
$$M(x) = \frac{M\ (3x - 2L)}{4L}\ , \qquad 0^+ \leq x \leq L\ . \tag{6.22b}$$

The beam's end point deflections, $y = 0$ at $x = -L$ and $y = 0$ at $x = L$, and end point slopes, $\frac{dy}{dx} = 0$ at $x = -L$ and $\frac{dy}{dx} = 0$ at $x = L$, can be used as boundary conditions for the integration of the elastic curve equation given below.

$$E \cdot I \cdot \frac{d^2y}{dx^2} = \frac{3Mx}{4L} + \frac{M}{2}\ , \quad -L \leq x \leq 0^- \tag{6.23}$$

Integrating twice will result in

$$E \cdot I \cdot y = \frac{Mx^3}{8L} + \frac{Mx^2}{4} + C_1 x + C_2 \tag{6.24}$$

where

$$C_1 = \frac{ML}{8} \quad , \qquad C_2 = 0 \ . \tag{6.25}$$

Deflection curve and slope of the beam respectively are

$$y = -\frac{\varepsilon \ x \ (x+L)^2}{d(2L - 3L_{gauge})} \cdot \quad , \quad -L \le x \le 0^- \tag{6.26}$$

$$\frac{dy}{dx} = -\frac{\varepsilon \ (x+L) \ (3x+L)}{d(2L - 3L_{gauge})} \quad , \quad -L \le x \le 0^- , \tag{6.27}$$

and the slope of the tangent line at the base of the position sensor ($x = 0$) is

$$\left.\frac{dy}{dx}\right|_{x=0} = -\frac{\varepsilon L^2}{d \ (2L - 3L_{gauge})} \ . \tag{6.28}$$

Therefore, slope of the position sensor is

$$\left.\frac{dy_p}{dx_p}\right|_{x_p=0} = \frac{d \ (2L - 3L_{gauge})}{\varepsilon L^2} = tan(\alpha) \ . \tag{6.29}$$

where

$$\left.\frac{dy_p}{dx_p}\right|_{x_p=0} \cdot \left.\frac{dy}{dx}\right|_{x=0} = -1 \ . \tag{6.30}$$

Then, the angle of the position sensor with respect to the coordinate frame, α (Figure 6.7), is defined as

$$\alpha = \begin{cases} tan^{-1}\left(\frac{d \ (2L - 3L_{gauge})}{\varepsilon L^2}\right), & \varepsilon > 0 \\ tan^{-1}\left(\frac{d \ (2L - 3L_{gauge})}{\varepsilon L^2}\right) + \pi, & \varepsilon < 0 \\ \frac{\pi}{2}, & \varepsilon = 0 \end{cases} \tag{6.31}$$

It is assumed that linear position sensor has high modulus of elasticity (rigid) and its deflection is negligible. Therefore its contact position can be calculated using the following equations:

$$x_{tip} = L_{tip}\ cos(\alpha) \qquad (6.32)$$
$$y_{tip} = L_{tip}\ sin(\alpha)$$

where L_{tip} is the overall length of the position sensor.

Resolution

The estimated ideal resolution of the sensors can be calculated using (6.2), (6.3), (6.18), (6.32) and the resolution of the DAQ system. The calculated resolution of the Design 1 is $(x,\ y,\ z) = (10.1,\ 4.7,\ 5.7)\ \mu m$. The resolution difference in the x and y axes are due to the relative placement of the strain gauges to sensor tip and the length of flexures. Resolution of Design 2 is $(x,\ y,\ z) = (0.9,\ 0.9,\ 4.5)\ \mu m$, note that resolution of x and y axes are same due to symmetry of the design. This resolution estimate is valid for the ideal case and does not include the effects of noise and unmodeled nonlinear effects.

6.4 Finite Element Simulation

Finite Element Model (FEM) analyses were done on the flexure beams to check the derived mathematical models (Figures 6.9, 6.10 and 6.12). Principle stress values (σ_{11}) were analyzed in the Finite Element Analysis (FEA) models. As the maximum stress on the surface of a deflected beam is equivalent to the principle stress value, corresponding strain values are calculated with principle stresses using Hooke's Law.

In this analysis, it was also confirmed that the effect of two-dimensional lateral

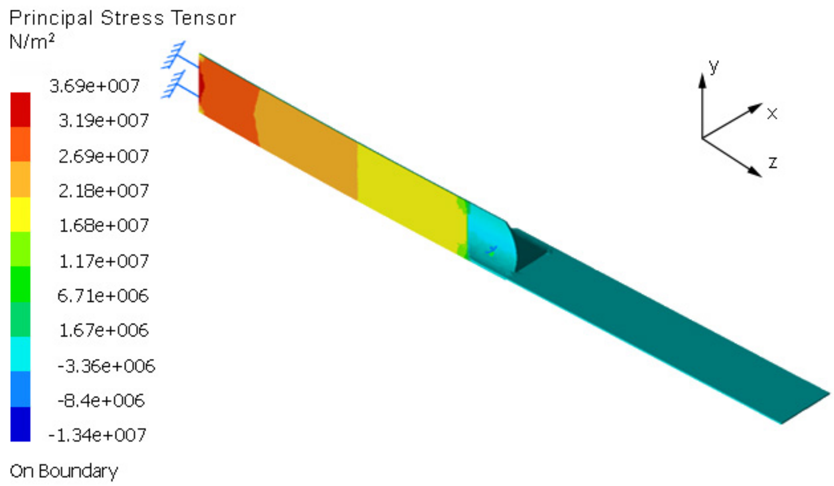

Figure 6.9: FEA principal stress results of the flexure beam for a sensor tip displacement of 6 mm in the x-direction. Stress value at the strain gauge position is $2.60 \cdot 10^7$ N/m^2.

motion on the flexure beams can be separated into its two orthogonal components with the used flexure geometries (cross structured beams and orthogonally fixed cantilever beams). This enabled the use of strain gauges for measuring motion in two dimensions.

Also modal analyses of the sensor designs during free vibration were carried out using the same finite element models. The first ten mode shapes and corresponding natural frequencies of these sensor models are shown in Figures 6.14 and 6.15. These analyses show that the desired working bandwidth of 10 Hz is well below the lowest natural frequencies of the sensor designs.

6.5 Experimental Results with the Prototypes

The prototypes of the designs are shown in Figures 6.11 and 6.13. The flexure parts of the prototypes are tested one axis at a time by measuring displacement of the sensor tip. The calibration of the sensors is done using a three-dimensional linear positioning stage. The calibration setup is depicted in Figure 6.16. Any error in

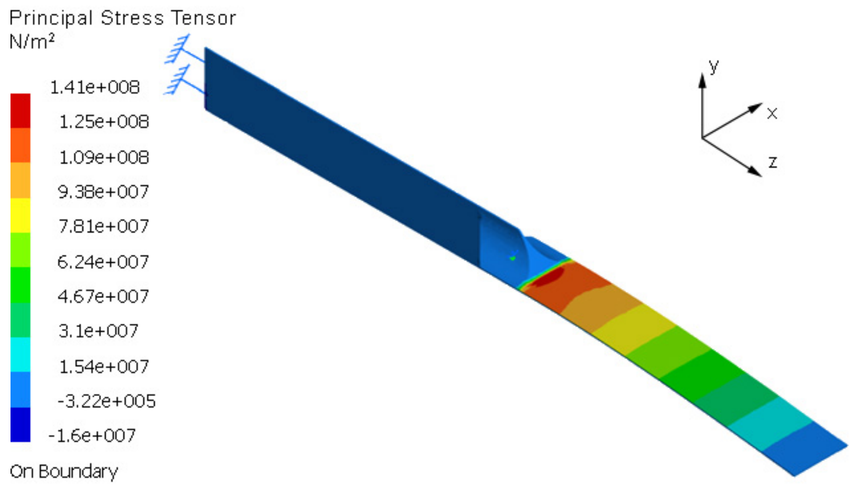

Figure 6.10: FEA principal stress FEA results of the flexure beam for a sensor tip displacement of -6 mm in the y-direction. Stress value at the strain gauge position is $8.84 \cdot 10^7$ N/m^2.

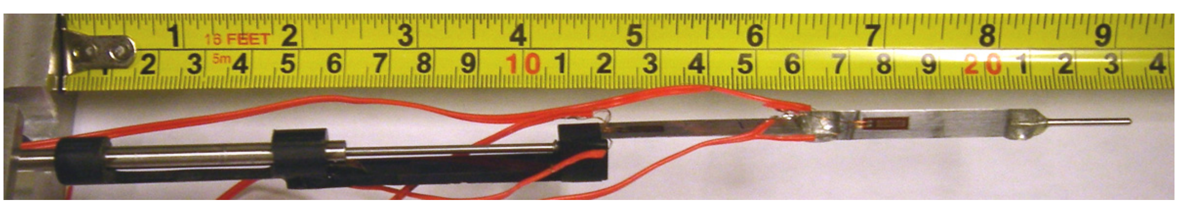

Figure 6.11: Prototype of the Whisker Sensor Design 1: The sensor is shown when the linear stage is fully extended. Overall length of the sensor when the linear stage is fully retracted and extended are 21.3 cm and 23.9 cm, respectively. The largest diameter of the prototype is 12.5 mm.

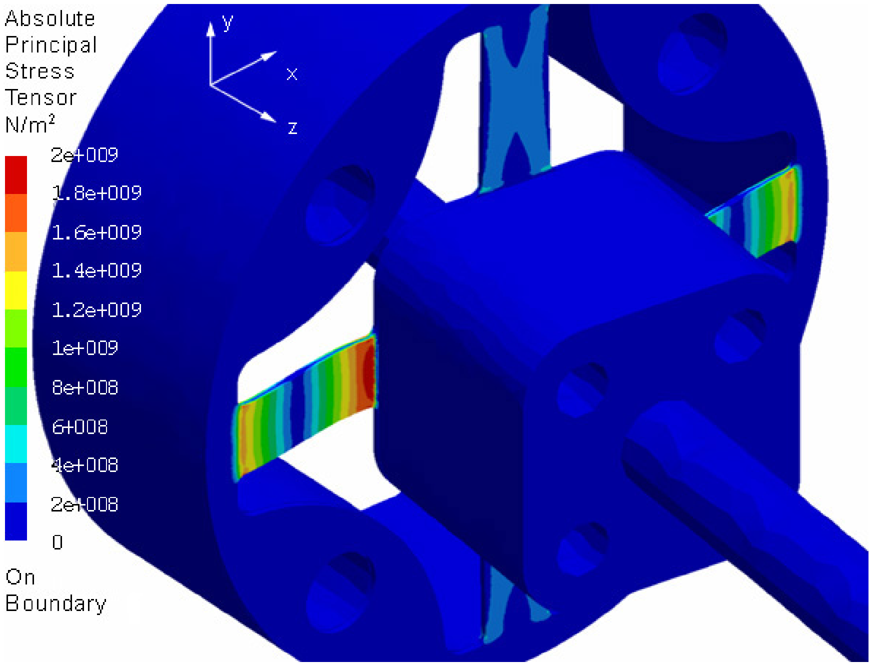

Figure 6.12: FEA principal stress results of the cross flexure structure for a sensor tip displacement of -2.5 mm in the x-direction. Stress value at the strain gauge position is $4.18 \cdot 10^8$ N/m^2.

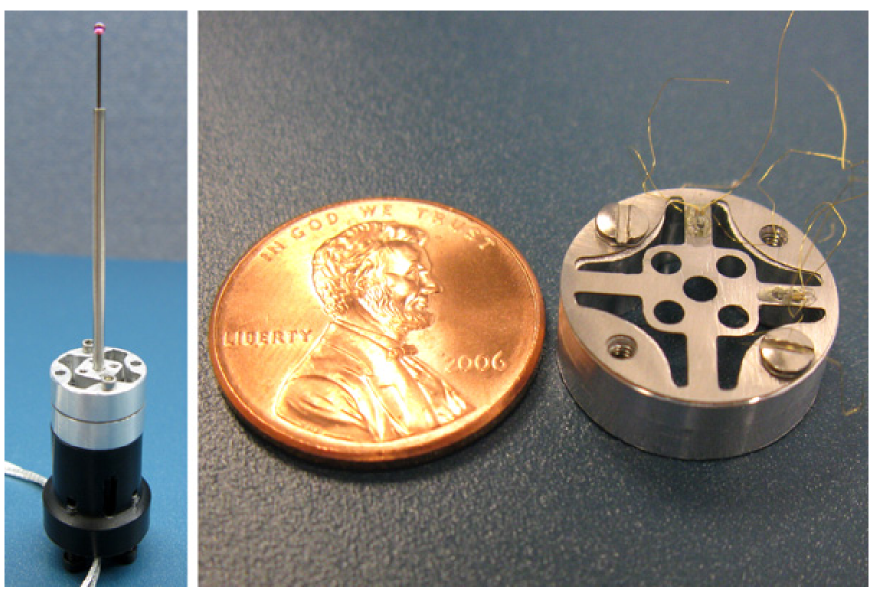

Figure 6.13: Prototype of the Whisker Sensor Design 2: *Left* - Overall length of the sensor when the linear stage is uncoiled is 65.0 mm (as shown here). The largest diameter of the prototype is 15.3 mm. *Right* - Flexure part of the sensor shown next to a cent.

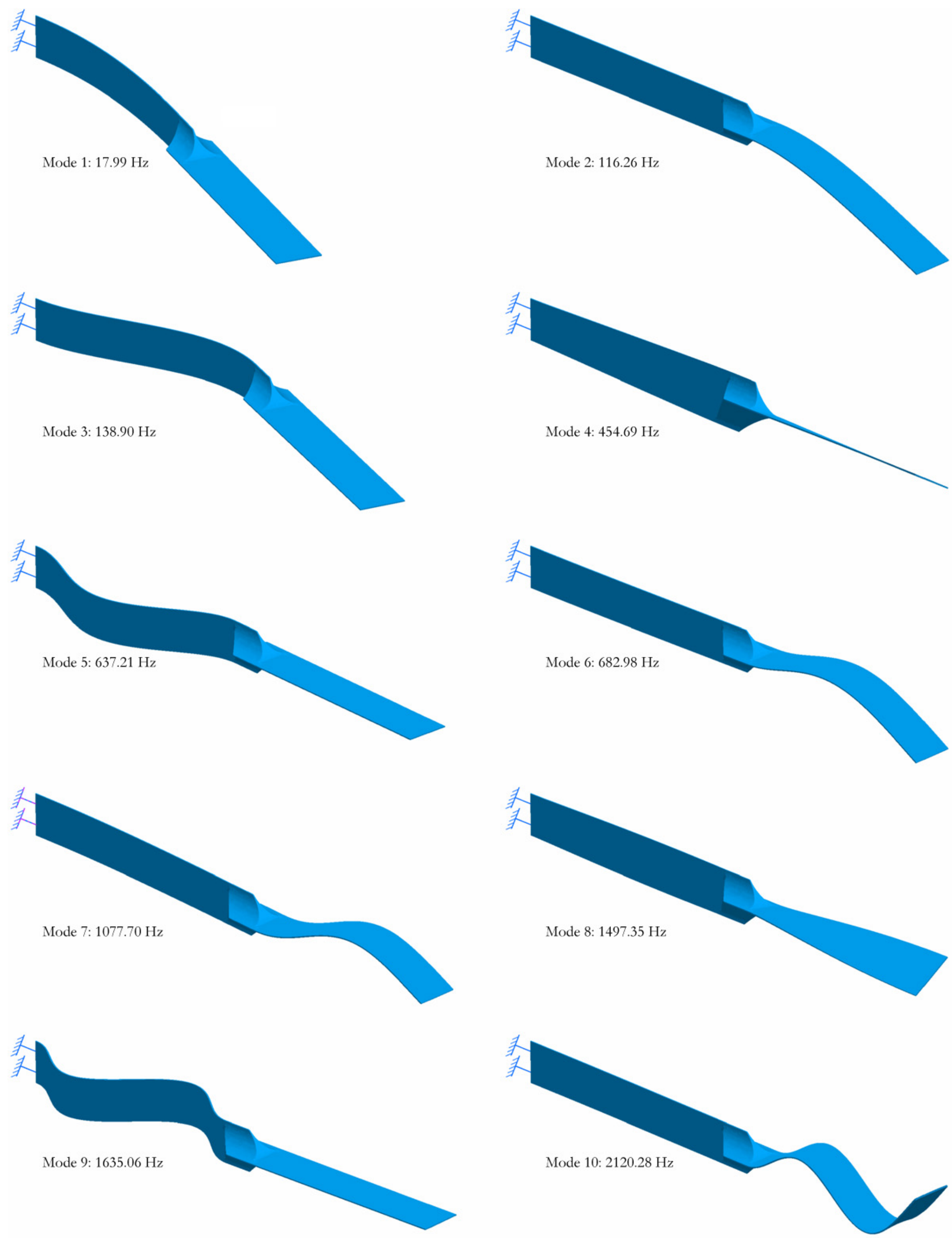

Figure 6.14: First ten mode shapes and corresponding natural frequencies of sensor Design 1.

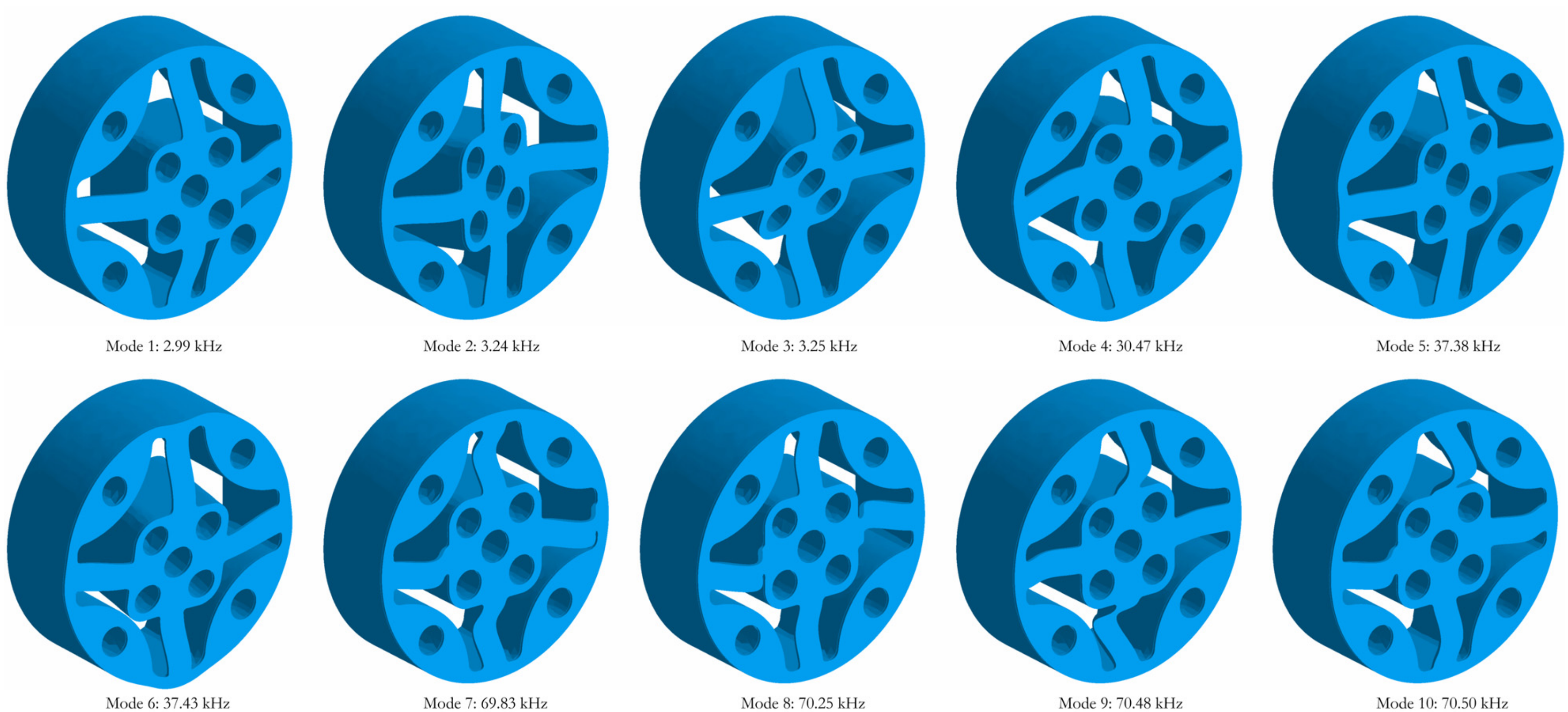

Figure 6.15: First ten mode shapes and corresponding natural frequencies of sensor Design 2.

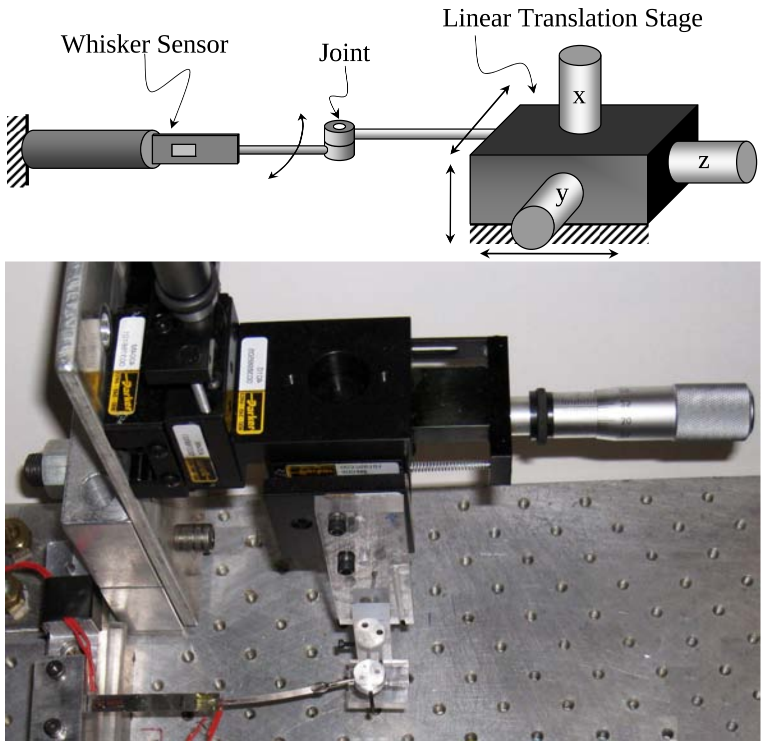

Figure 6.16: Setup for static testing. A three-dimensional linear positioning stage is used to move the sensor tip.

the mathematical model was corrected using the calibration plots created with the collected data, as described below for each prototype.

Simulation and experimental strain and tip bending force measurement results of restrained sensor tip are given in Table 6.1. In simulations, the estimated strain values are computed at a selected sensor tip displacement. For the experimental case, actual strain readings from the prototype sensor at the same tip deflection are reported. Strain values in the FEM analyses report the averaged strain values of the nodes where the actual strain gauges are bonded in the prototypes. If a small strain gauge is used with a relatively longer beam, the gauge is assumed to measure the strain value at the center point of the strain gauge. The measured strain value starts to deviate from the actual strain as the flexure beams get shorter relative to the length of the strain gauge. In the cantilever beam model, measured strain and the actual strain at the center point of the strain gauge can be assumed to be equal. But the

Table 6.1: Strain and tip bending force measurement results for constant sensor tip displacement: *In simulations, the estimated strain and tip bending force values at the selected sensor displacements are calculated. Actual strain gauge readings from the prototype sensors and measured tip force at the same tip displacements are reported for the experiment case.*

	Design 1		Design 2
Tip Displacement	6.0 mm		2.5 mm
Bending Flexure Element	X	Y	X or Y
Strain	m/m		
Mathematical Model	$2.38\ 10^{-4}$	$4.50\ 10^{-4}$	$1.60\ 10^{-3}$
Finite Element Analysis	$1.39\ 10^{-4}$	$4.58\ 10^{-4}$	$1.58\ 10^{-3}$
Experimental Value	$1.71\ 10^{-4}$	$4.49\ 10^{-4}$	$1.21\ 10^{-3}$
Tip Force	mN		
Mathematical Model	48.0	122.9	260.1
Experimental Value	12.2	58.7	694.4

effect of the mentioned centreline assumption can be observed with the experimental and the calculated values of the cross beam prototype. Therefore the averaged strain values of the FEA nodes are tabulated in Table 6.1. The estimates and actual strain values of cantilever beam sensor (Design 1) are closer than the values for the cross beam sensor (Design 2). Also, FEM results are affected by the deflection of sensor elements other than flexures (i.e., flexure joint elements, position sensors).

For tip force measurements, a ATI Nano17, 6-axis F/T sensor with force resolution of $1/80$ N was used [63]. Measured and calculated force values were in the same order for both prototypes. The difference in the mathematical model is due to the estimation of the parameters such as E and I.

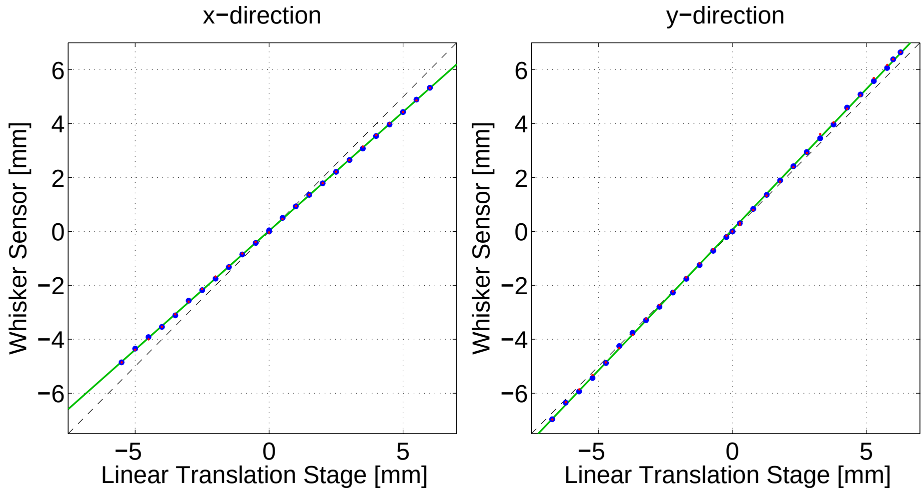

Figure 6.17: Tip position measurement results for the prototype of the Whisker Sensor Design 1. $f(x) = 0.8819x + 0.0249$, $f(y) = 1.0433y + 0.0639$

Prototype of Design 1

Figure 6.17 shows the static calibration data collected from the prototype of the Design 1. These plots show the general behavior of the sensors under predetermined sensor tip displacement. Linear fits to the data show that prototype of Design 1 has almost no nonlinearity. Especially the fit for y-direction data is almost on the theoretical line (i.e. $slope = \pi/4$). As the mechanical structure of the beams gets complicated, the reported results starts to vary for the same element (Table 6.1). For instance, reported results of the cantilever beam that measures the motion in y-direction are similar. This is mainly because of the geometrical simplicity of that element. Also, in the static testing no significant hysteresis is observed for this design.

Dynamic testing of the prototype under harmonic motion was conducted to determine the accurate working bandwidth of the sensors. A LVDT sensor attached to a motor was used to create harmonic motion at constant frequencies. The setup used for dynamic testing is depicted in Figure 6.18. Two dimensional position information collected from the 2 DOF dynamic setup is compared to the sensor's position output. Frequency response of the prototype of Design 1 is shown in Figure 6.20. The

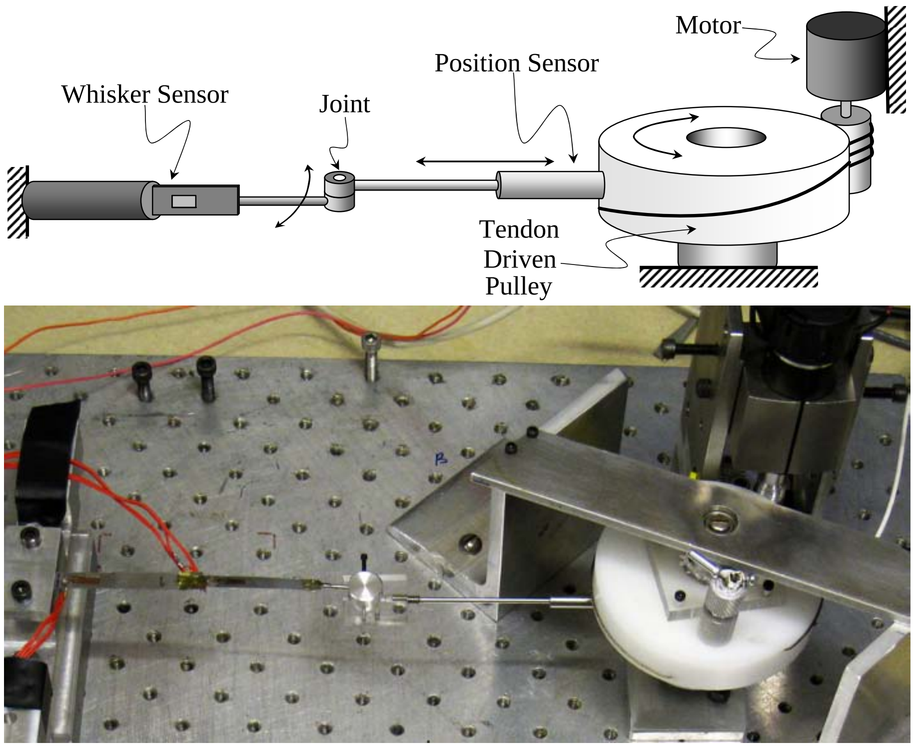

Figure 6.18: Setup for dynamic testing. A tendon driven pulley is actuated with a servo motor to move the sensor tip.

frequency response of the sensor is flat up to a resonance observed around 10 Hz. Phase difference is about 1-2 degrees in the 0.1-12.0 Hz range. Lissajous plots for the cantilever beam prototype under 0.1, 1.0 and 10.0 Hz harmonic motion are shown in Figure 6.19. Coefficient of determination (R^2) values obtained by least squares regression for the dynamic test results are shown in Figure 6.21-A. R^2 values are above 0.968 in the 0.1-10 Hz range for the prototype of Design 1, showing the linearity of the measurements collected by the sensor. Maximum measured percent hysteresis values are shown in Figure 6.21-B. Hysteresis values below 3% are observed for low frequencies, and around 6% hysteresis is observed for high frequencies.

Prototype of Design 2

Figure 6.22 shows the static calibration data collected from the prototype of the Design 2. No significant hysteresis was observed in the static testing of this design

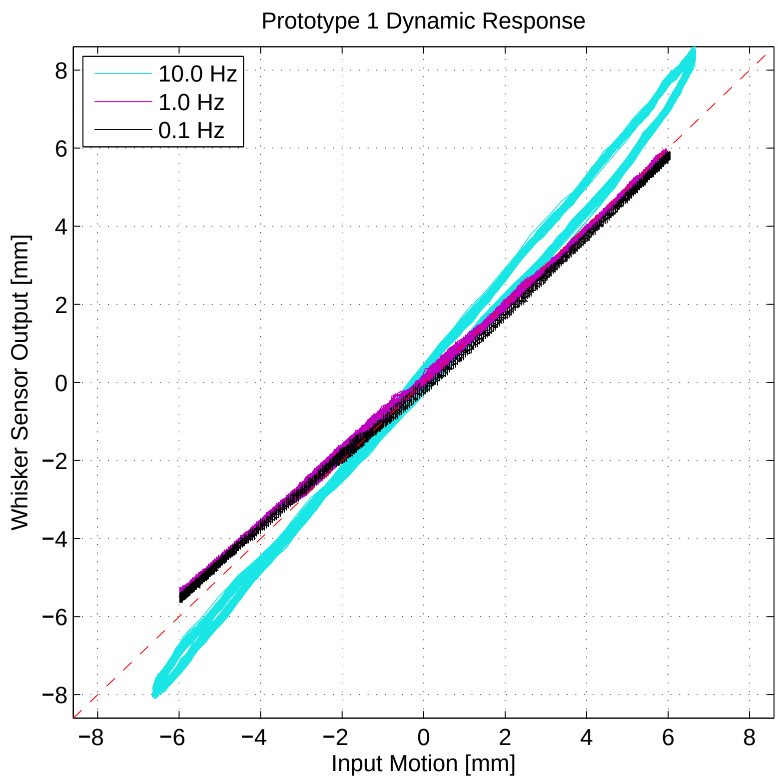

Figure 6.19: Dynamic response data of the cantilever beam prototype under 0.1, 1.0 and 10.0 Hz harmonic motion.

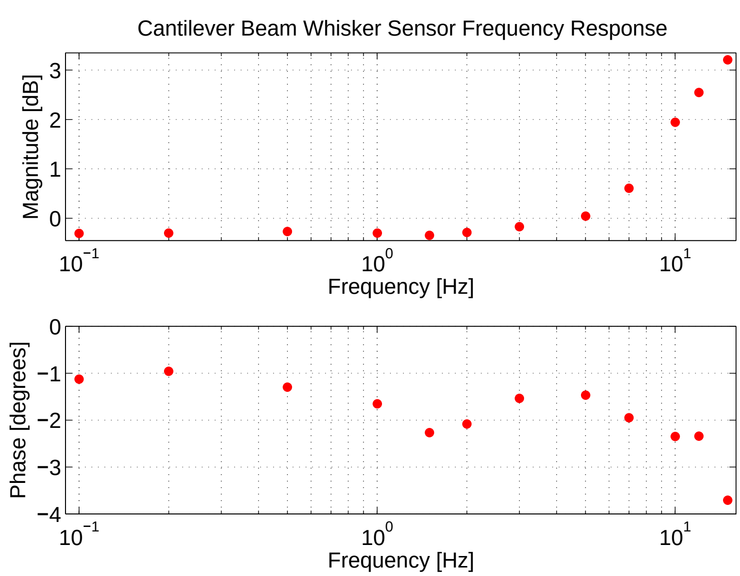

Figure 6.20: Frequency response data of the cantilever beam prototype

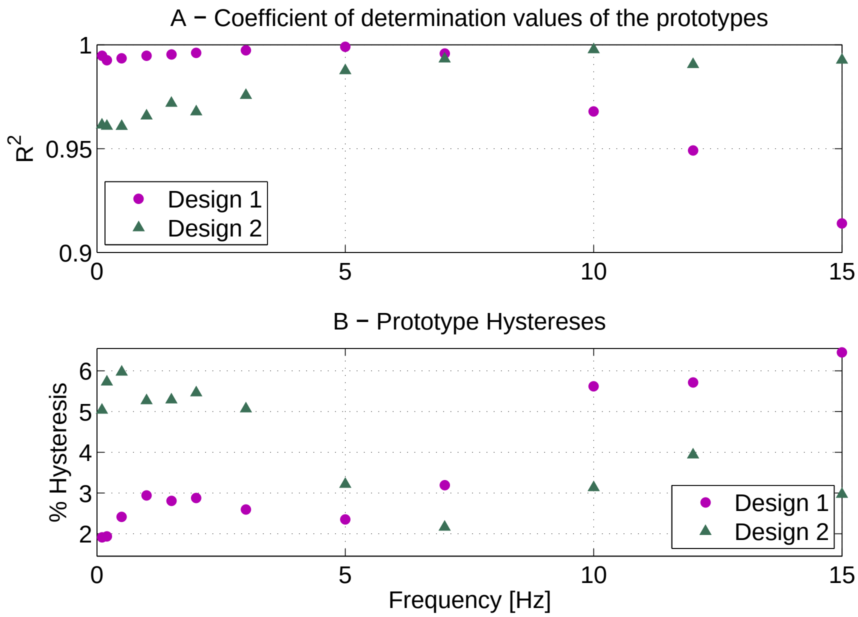

Figure 6.21: A-Coefficient of determination values of the prototypes over the dynamic test bandwidth. B-Maximum measured percent hysteresis values of the prototypes over the dynamic testing bandwidth.

either. Cubic polynomial fits are shown in the plots. The nonlinearity observed in the Figure 6.22 is due to the measurement inaccuracies of the parameters used in (6.31) and (6.32). For subsequent tests, the measurements were corrected using the inverse of the cubic calibration curves. Two axes of the prototype are physically same, and similar response results are observed.

Frequency response of the Design 2 prototype is shown in Figure 6.24. The frequency response of the sensor is flat up to a resonance observed around 10 Hz. Phase difference is about 1-3 degrees in the 0.1-15.0 Hz range. Lissajous plots for the cross beam prototype under 0.1, 1.0 and 10.0 Hz harmonic motion are shown in Figure 6.23. Coefficient of determination (R^2) values are above 0.9608 in the 0.1-10 Hz range for the prototype of Design 2, showing the linearity of the measurements collected by the sensor. Maximum measured hysteresis is around 5% for low frequencies. Smaller hysteresis values, around 3%, are observed for high frequencies.

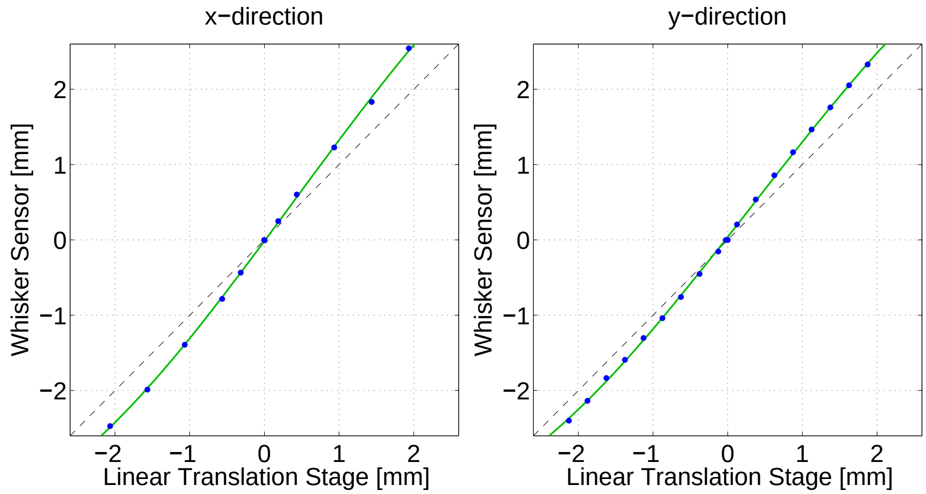

Figure 6.22: Tip position measurement results for the prototype of the Whisker Sensor Design 2. $f(x) = -0.0211x^3 + 0.0245x^2 + 1.3375x - 0.0163$, $f(y) = -0.0197y^3 + 0.0188y^2 + 1.2622y + 0.0388$.

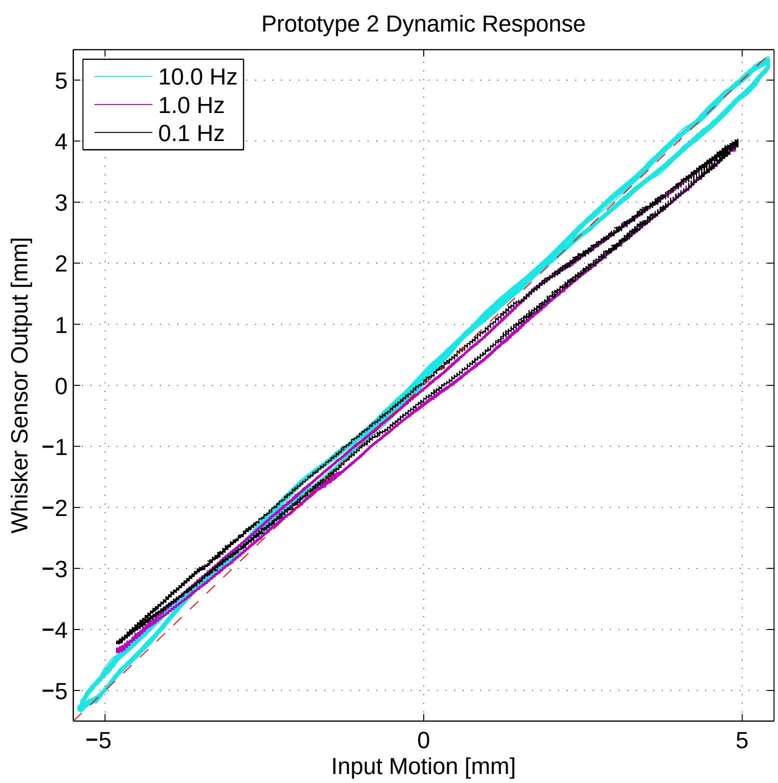

Figure 6.23: Dynamic response data of the cross beam prototype under 0.1, 1.0 and 10.0 Hz harmonic motion.

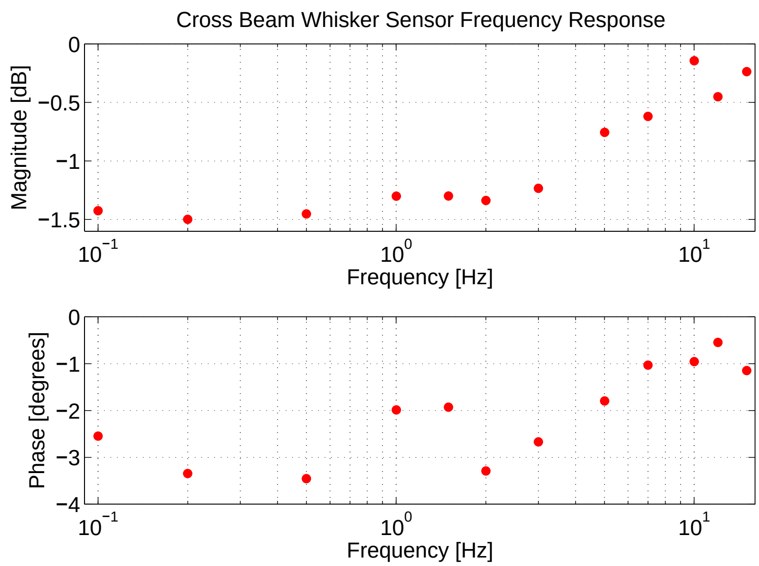

Figure 6.24: Frequency response data of the cross beam prototype

Discussion

In this section, a novel position sensor to measure physiological motion of biological tissue in robotic-assisted minimally invasive surgery is presented. The manufactured prototype showed that use of proposed whisker sensors are promising and able to effectively measure dynamic motion at a bandwidth of 10 Hz.

Similar magnitude responses are observed in both sensor prototypes although their physical properties are different. Start of a resonant peak is visible in the magnitude plots. It is believed that the resonance is caused by the dynamics of the two-degree-of-freedom test setup.

The resolution values reported in Section 6.3 are not homogenous in the three directions. If desired, the flexure beams' dimensions and the position of the strain gauges can be optimized to provide uniform resolution in every direction.

Chapter 7

Sensors in Robotic-Assisted Beating Heart Surgery

Sensing systems, for monitoring biological signals and tracking heart motion are critical components of the overall system. In this application, redundant sensing systems are desirable for safety reasons. Measurement of heart motion with high precision and high confidence is required for precise tracking performance. One of the major focus of this thesis is developing sensing systems and algorithms for fusing the information supplied from the different systems for superior performance.

In this chapter, first, sensors planned to be used with the robotic system other than the whisker sensor are described. Working principles and specifications of sonomicrometric sensor, stereo camera system, accelerometer and laser sensors are given. Then, a preliminary noise characterization for the future sensor system implementation is given. A general statistical fusion method motivated by the geometry of uncertainties for robotic systems with multiple sensors proposed by Nakamura *et al.* [64] is used. A detailed explanation of the method is provided in Appendix C. This sensor fusion method aims to increase the accuracy and reduce the uncertainty by combining redundant sensory information. The described sensors are analyzed within this fusion framework.

7.1 Sonomicrometric Sensor

One of the sensor systems, that is planned to be used, is Digital Ultrasonic Measurement System (*Sonomicrometer*) obtained from Sonometrics Corporation, Canada. Sonomicrometers employ piezoelectric transducers. Scalar intertransducer element distances with no relative or absolute directional orientation can be measured between transmitter and receiver piezoelectric crystal pairs within soft tissue by using sound energy [29]. Ratcliffe *et al.* [28] used a piezoelectric transducer element to broadcast to an array of receivers, and by sequentially changing the broadcasting transducer, they measured the entire set of intertransducer element distances. Switching between the transducers are done at very high speeds therefore during the operation the delay in successive measurements are insignificant compared to the measured biological signal. With the measured scalar distances in hand, trigonometry is sufficient to locate the transducer elements in 3-D space.

In sonometric sensors flight time of a burst of ultrasound is measured. No analog conversion process is involved in these measurements, which eliminates the need to calibrate the systems. Crystal operation frequency of 64 MHz provides resolution of 24 μm in the measurement of intertransducer element distances. The rate at which the circuitry cycles through the transmitters is determined by the cycle time. System allows cycle times between 28 μs and 2044 μs in 16 μs intervals. At the end of each cycle, the measurement data is stored and then the next transmitter is activated. When all of the piezocrystal transmitters are circled, a block of measurement is completed. Considering the transmit time of sound and to allow acoustic energy to dissipate before next cycle optimum cycle time should be around 348 to 444 μs for a distance of 150 mm. If all 6 crystals are operated and cycle time per transreceiver

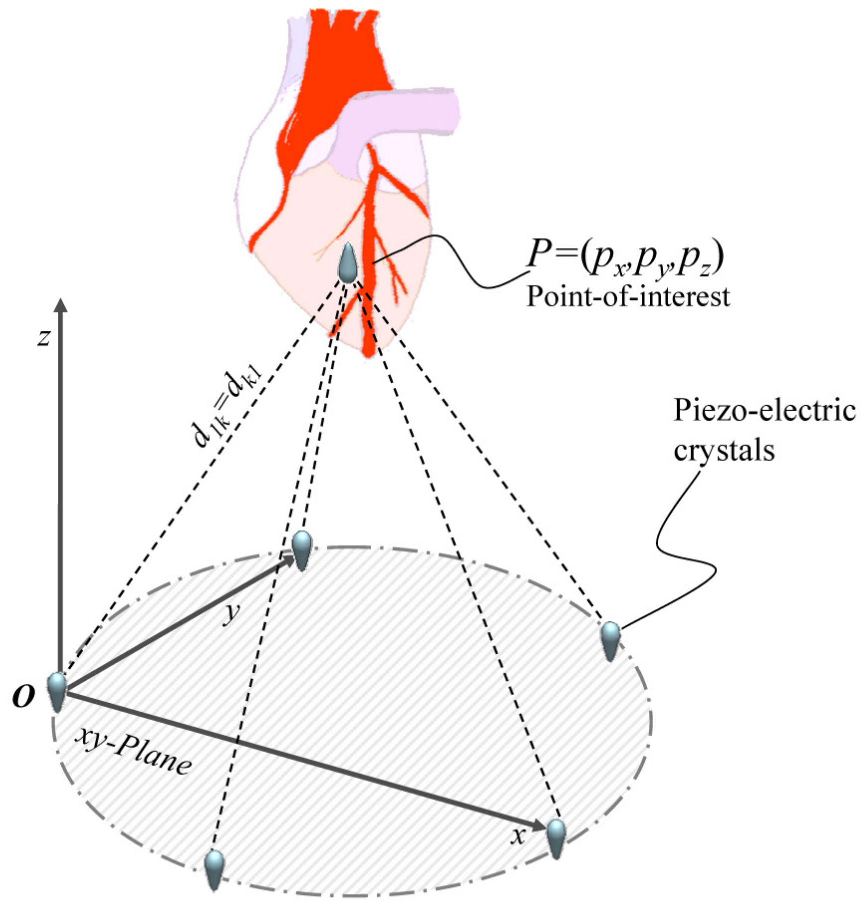

Figure 7.1: Sonomicrometer Sensing Model: Five crystals were mounted to a base to measure the distance of a sixth crystal attached to the heart.

is set to 348 μs, block time would be 2.088 ms giving a total sampling frequency of 478.93 Hz for the sensor system.

In this sensor system, the sensors are assumed to be well calibrated. No errors due to the inaccuracy of the flight time measurements, uniform speed of sound in the medium of measurements and no weak signal reception are assumed. Only possible error is due to the crystal's geometry, which only affects the absolute value of the distance measurements. This error is estimated to be 1.5 mm or less. Absolute accuracy of the sonomicrometry system is 250 μm (approximately $1/4$ wavelength of the ultrasound) [30].

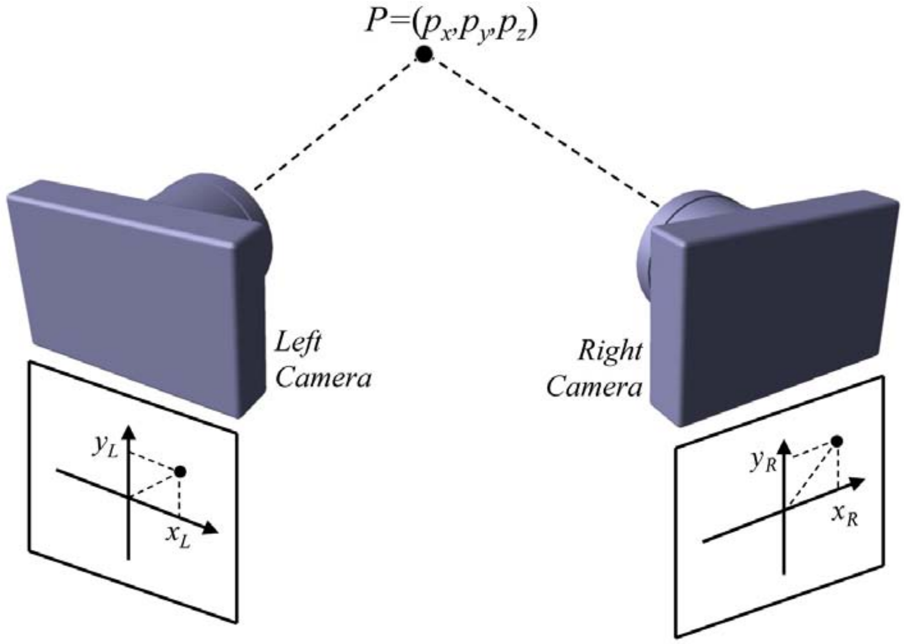

Figure 7.2: Stereo Vision Sensing Model: Position data of a point from two cameras are combined to measure displacement in 3D.

7.2 Multi-Camera Vision System

A vision system can be used to capture the global motion of the heart. Vision systems were widely used in heart tracking by other researchers.

Measurement resolution of a vision system depends on the camera quality and the distance to the point of interest (POI). A small color camera model was selected to be used in the sensing system. Panasonic GP-KX121 series cameras feature 512 Horizontal $\times$ 492 Vertical pixels, 30 frames-per-second. The standard lens has the configuration of 51° field angle (angle of view), F/2.0 max aperture and $\boldsymbol{f}$ =3.7 mm focal length [65]. Assuming a viewing distance of 15 cm, the camera has 0.29 mm/pixel resolution (Figure 7.3).

Two cameras placed about b =3 cm apart with parallel optical axes, providing a stereo image of the area of interest is planned to be used. This configuration is called normal stereo camera system, since the images' coordinate frames lie on the same plane [66]. Position of a point, $P(p_x, p_y, p_z)$, is calculated by the disparity within

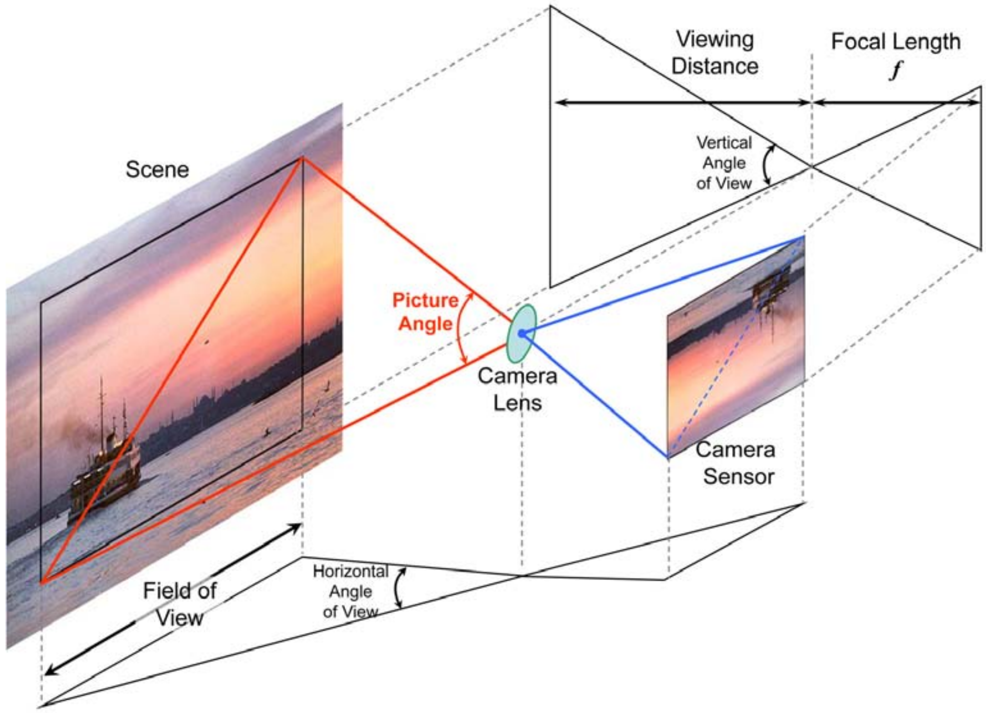

Figure 7.3: Optics of a camera.

stereo image pairs using perspective projection:

$$p_x = \frac{b}{2} \cdot \frac{x_L + x_R}{x_L - x_R}, \quad p_y = \frac{b}{2} \cdot \frac{y_L + y_R}{x_L - x_R}, \quad p_z = \frac{b \cdot \boldsymbol{f}}{x_L - x_R} \tag{7.1}$$

where x_L, y_L and x_R, y_R are the position image of P in the image frames of *Left Camera* and *Right Camera* respectively (Figure 7.2).

7.3 Laser Sensor

A triangulating laser displacement sensors is planned to be used in the sensory system. A laser sensor will give one-dimensional position information of the heart position. Laser sensors are preferred because of their flexible use and high precision measurements.

A laser triangulation sensor uses a transmitter (laser diode) to project a spot of light to the target, and its reflection is focused via an optical lens on a receiver (e.g.

charge coupled device (CCD)). If the target changes its position from the reference point the position of the reflected spot of light on the detector changes as well. The signal conditioning electronics of the laser detects the spot position on the receiving element and provides an output signal proportional to target position. Resolutions down to 0.01% (i.e. 20 μm) of the working range can be achieved [67].

7.4 Accelerometer

The accelerometer that will be used in the sensing system is a three axis low-g, micromachined accelerometers with adjustable measurement ranges between ± 2.5 g to ± 10 g, manufactured by Freescale Semiconductor [68].

Each axis consists of two surface micromachined capacitive sensing cells and a signal conditioner. Sensing cells are mechanical structures made of semiconductor materials using semiconductor processes (masking and etching). It can be modeled as a set of cantilever beams attached to a movable central mass that moves between fixed beams. With acceleration the cantilever beams are deflected. As the beams attached to the central mass move, the distance from them to the fixed beams on one side will increase by the same amount as the distance to the fixed beams on the other side decreases. The change in distance is a measure of acceleration. The heart data described in Section 2.2 has acceleration peaks around 7 g. Therefore the sensor will be used in the 10 g range. The measured RMS noise is 4.7 mV, when the sensitivity of is adjusted to 120 mV/g.

7.5 Sensor Fusion for Robust Measurement of Heart Motion

Extracting accurate and precise position information of the heart from all of the position tracking sensors is an important prerequisite for proper working of the control algorithms. Information from the sensors described in the previous chapter, except for the accelerometer, are going to be fused to acquire high precision position measurement of the point of interest (POI). Although briefly explained in Section 7.4, accelerometer data is not going to be included in the geometrical fusion method because the sensor cannot provide direct position measurements. Accelerometer sensor can be used in correcting the uncertainties from other sensors, such as sonomicrometer, therefore this sensor will be a part of dynamic fusion algorithm (i.e. Kalman filtering)

7.5.1 Whisker Sensor

A continuous contact position sensor is necessary for satisfactory tracking of the POI on the heart. The whisker sensor is a high sensitivity sensor that comes out from the tip of the surgical manipulator and touches the heart surface. Combining two different sensing systems, namely strain gauges and linear position sensor, the tip position of the sensor can be calculated with respect to its base. The position of the sensor's contact point with the tissue, $P(p_x, p_y, p_z)$, can be calculated using the strain measurements, ε_x and ε_y, acquired from the DAQ board, and position information, d_z, acquired from the linear position sensor, $\theta_i = [\varepsilon_x \; \varepsilon_y \; d_z]^T \in \mathbb{R}^3$.

Shape of the uncertainty geometry for the sensor prototype 1 described in Section 6.5 is an ellipsoid (Figure C.1). The most uncertain measurement direction is x-axis ($e_{i,1}$) and the least uncertain measurement direction is y-axis ($e_{i,3}$). For the sensor prototype 2, the uncertainties are equal for x- and y-axis. For this prototype, least uncertain measurement direction is along the z-axis.

7.5.2 Sonomicrometric Sensor

In this sensor frame, the low level measurements are the scalar intertransducer element distances, d_{tr}, where $t = 1, \ldots, k$, $r = 1, \ldots, k$ and $t \neq r$, t is the index number for the transmitter transducer, r is the index number for the receiver transducer, and k is the number of the transducers used in the sonometric sensor setup. The number of available unique scalar measurements using k transducers is ${}_kC_2 = \frac{k(k-1)}{2}$. Unique transducer measurements are represented with d_s where $s = 1, \ldots, \frac{k(k-1)}{2}$. Any three of the transducers that are placed on the base (i.e. other than the transducer placed on the POI) can be used to create a coordinate frame, therefore 3 of the $\frac{k(k-1)}{2}$ scalar measurements are used to form a reference frame. Then the distance from the origin of the sensing frame O-xyz and the POI, $P(p_x, p_y, p_z)$, can be calculated (Figure 7.1). Accordingly the sensory data and the sensory information become $\theta_i = \left[d_1\ d_2\ \ldots\ d_{\frac{k(k-1)}{2}}\right]^T \in \mathbb{R}^{\frac{k(k-1)}{2}-3}$ and $x_i = [p_x\ p_y\ p_z]^T \in \mathbb{R}^3$ respectively.

So in order to satisfy the condition of (C.1), $n(=3) \leq m_i$, order of sensory data space, m_i, should be equal or greater than $n = 3$,

$$(n =)\, 3 \;\leq\; \left(\frac{k(k-1)}{2} - 3\right)(= m_i) \;\;\Rightarrow\;\; k \geq 4\,.$$

Therefore at least four transducers are necessary to represent the sensory information as described in (C.1). The sonomicrometer setup obtained from SonoMetrics Corporation has six channels for piezoelectric crystals. The planned placement of the crystals will be as follows. One of the piezoelectric crystals will be placed on the POI. The remaining crystals will be placed on a fixed base beneath the heart, facing towards the POI. Geometrical placement of the piezoelectric crystals on the base will affect the formation of the uncertainty geometry of the sensor. Therefore, sensors should

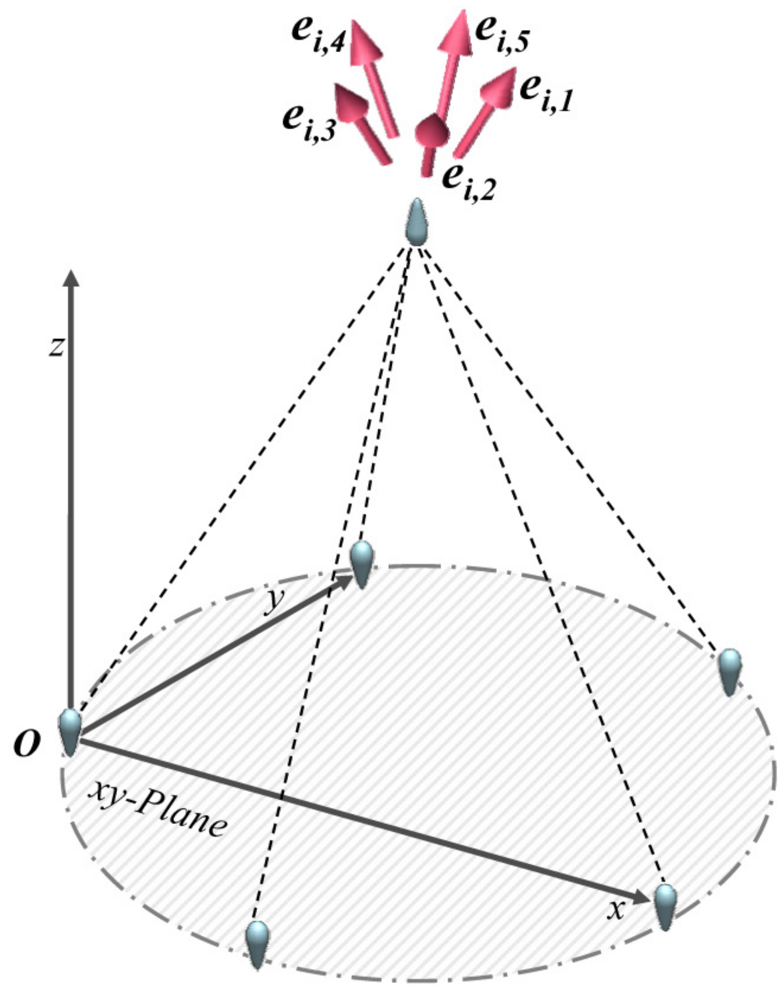

Figure 7.4: Sonomicrometer Sensing Model: Crystal placement and principle variation axes are shown.

be mounted asymmetrically to prevent having homogeneous solutions since solutions depend on geometrical placement. In order to minimize the uncertainty geometry of the sensor, the base crystals should be placed evenly on a circle. Both of these could be satisfied by placing the crystals on a circle slightly shifting them from their original evenly spaced positions. The position information of the fourth crystal (i.e. the crystal attached next to the POI) relative to the origin can be calculated using geometric triangulation method. There are ten possible reference coordinate frame combinations that can be formed from the five base crystals. These ten measurements are combined with least square analysis to minimize the measurement error.

In Figure 7.4 the principle variation axes, $e_{i,k}$ $k = 1, \ldots, 5$, for base crystals are shown. The uncertainty in the direction of these unit vectors are minimum for each crystal. Geometrical fusion of uncertainties according to these principle axes minimizes the uncertainty geometry of the sensor setup. Shape of the uncertainty geometry for the sensor is a spheroid[4].

7.5.3 Multi-Camera Vision System

Vision systems potentially have problems with noise and occlusions. Besides, their resolution are restricted with the image quality. The noise performance can be improved by using fluorescent markers but in stand alone operations the occlusion problem remains to be solved. The fusion algorithm should handle any occlusion problems during tracking. As a simple solution, the data obtained from the vision system can be omitted by the fusion process until the occlusion is over.

A stereo vision system example is shown in Figure 7.2. The position of point of reference P in the absolute coordinates is $x_i = [p_x\ p_y\ p_z]^T \in \mathbb{R}^3$. Here, x_i is to be computed from $\theta_i = [x_R\ y_R\ x_L\ y_L]^T \in \mathbb{R}^4$ where $[x_R\ y_R]^T$ and $[x_L\ y_L]^T$ are the position image of P in the image frames of *Right Camera* and *Left Camera* respectively (Figure 7.2). Therefore, $(n = 3) < (m_i = 4)$ is satisfied.

A similar approach can be followed for the multi-camera vision system. A camera has two principle variation axes, accordingly, each camera has an uncertainty shape of ellipsoid based cylinder (Figure 7.5). The geometry for uncertainty−intersection of the cylinders−is a curved parallelogram solid. The further the cameras are placed with respect to each other in a multi vision system, the more detached will be the principle variation axes. Therefore, resultant shape of the geometric fusion would be minimized.

[4]Spheroid is a quadric surface in three dimensions obtained by rotating an ellipse about one of its principal axes.

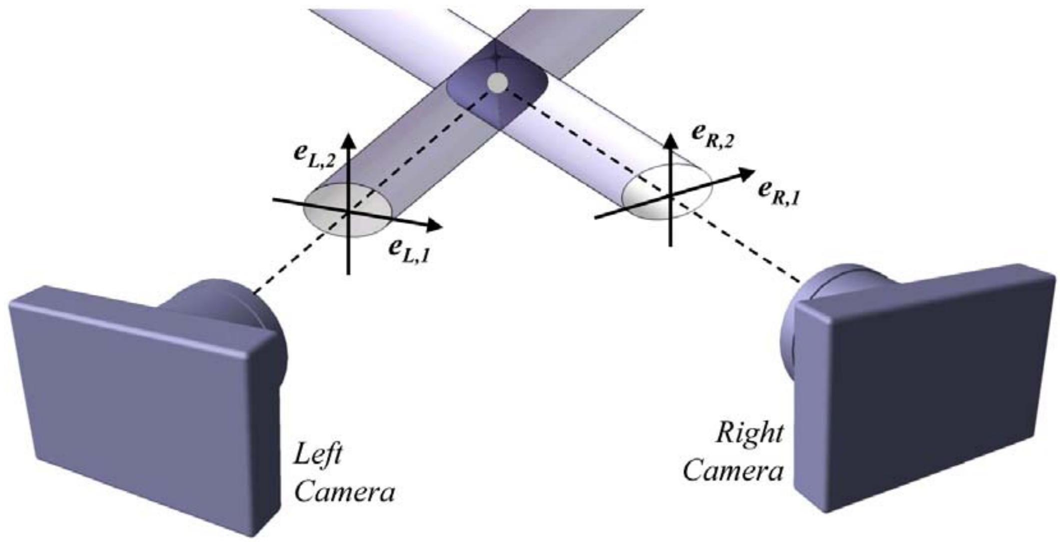

Figure 7.5: Formation of an uncertainty ellipsoid in a Stereo Vision Sensing Model.

7.5.4 Laser Sensor

A laser sensor will give one-dimensional position information of the heart position. It will be possible to compensate for the vision sensor's low precision measurements in the normal direction.

The distance to the point of reference, $x_i = [d_z] \in \mathbb{R}$ is to be computed from $\theta_i = [V_{laser}] \in \mathbb{R}$ where V_{laser} is the measured sensor voltage. Therefore, $(n = 1) \leq (m_i = 1)$ is satisfied.

7.5.5 Sensor Placement for Minimal Uncertainty

The sensors described above should be positioned in a way to minimize uncertainty. Sensor positions and orientations are selected to take advantage of the least uncertain measurements collected by the sensors. In an experimental setup to measure the position of LAD, positioning of the sensors should be as follows.

Sonomicrometric Sensor has the least flexibility due to its physical properties. Base carrying the five fixed crystals will be placed beneath the heart, and the sixth crystal will be sutured next to point of reference. Whisker sensor will approach the heart from the side touching the heart with a narrow angle to the chest. This placement will shrink the measurement uncertainty of the sonomicrometer within frontal plane. Two cameras separated by 3 cm will be placed 15 cm above the heart. The laser sensor will be placed next to the camera pair measuring its distance from the heart. This will enable the reduction of the measurement uncertainty in the normal direction created by the vision system.

Chapter 8

Conclusions

According to the Centers for Disease Control and Prevention (CDC) statistics [1, Table 7], heart disease was the leading cause of mortality with 654,092 deaths in 2004. Improving the treatment for coronary heart disease is a need that should be prioritized and relevant treatment options should be developed in the fields. Robotic-assisted off-pump beating heart surgery with active relative motion canceling will allow bypass graft surgeries to be performed on a stabilized view of the beating heart with the technical convenience of on-pump procedures. This will eliminate the use of cardio-pulmonary bypass machines in on-pump heart surgeries, or the use of passive stabilizers in traditional off-pump beating heart surgeries.

In this study, the use of biological signals in the model-based intelligent Active Relative Motion Canceling (ARMC) algorithm to achieve better motion canceling was presented. The tracking problem was reduced to a reference signal estimation problem with the help of a model predictive controller. The estimated signal was created by using the last heartbeat cycle with cancelation of the position offset. Due to the quasiperiodic nature of the heart motion, heartbeat period could change in time. In order to reduce the error resulting from heart rate variations, ECG wave forms were detected and used to adjust heartbeat period during the tracking. Experimental results showed that using ECG signal in ARMC algorithm improved the reference signal estimation. It is important to note that, for patients with severe rhythm abnormalities, the detection of the ECG waveforms present a challenge for the proposed method.

Biological signals other than ECG that can be used to assist the tracking of heart motion include aortic, atrial and ventricular blood pressures. Similar to the ECG signal, these blood pressures are significant indicators of the heart motion as they can be used to predict when the heart valves will be opening and closing, which in turn helps us determine the distinct phases of the heart cycle. These distinct phases correspond to qualitatively different mechanical properties of the heart tissue, changing the local deformation model. The blood pressure signals also give additional independent information, which can be used in conjunction with ECG signal to improve noise robustness and to reliably detect unexpected rhythm abnormalities and arrhythmias, which will be a challenging part for the realization of the ARMC algorithm.

One of the restrictions faced in this dissertation was the limited prerecorded data. Longer position and ECG data sets from healthy cases as well as cases with heart disease are needed to effectively evaluate the performance of the controllers used. Such evaluations can provide better estimation algorithms especially in cases where the ECG signal is not a sufficient data source due to disease related irregularities or unexpected interruptions during surgery.

Image stabilization in addition to tracking the heart motion with the surgical tools is an important requirement for successful performance of off-pump bypass surgery without passive stabilization. The developed ARMC algorithm can be applied to camera control to achieve image stabilization.

In this study, the controller parameters were selected empirically. To the best of our knowledge, automatic selection of these parameters is still an open problem in the control literature. Although the weighting parameters were well tuned to minimize

RMS error, a more comprehensive study can be conducted to automate the process and find the optimum gains.

This study used prerecorded position data from a sonomicrometer. An important part of this robotic system is the development of sensing systems that will be appropriate to use in a tight control loop for active tracking of the heart. These sensing components will track the heart motion, monitor biological signals, and provide force feedback. Multi sensor fusion with complementary and redundant sensors will be used for superior performance and safety. The whisker sensor introduced here is a high sensitivity contact sensor. The advantage of whisker sensor is that it will directly give the relative motion of the heart with respect to the robotic manipulator.

Merging the sensor data from multiple position sources would increase the accuracy of motion detection and improve tracking results. An analytical formulation for asynchronous fusion of the sensory data without creating any inconsistencies was presented for the planned sensors to be used at an actual system. Adding more mechanical sensors that measure heart motion would improve the measurement precision.

Appendix A

Traditional Controllers

In this Appendix the traditional controllers used for tracking are described. The system to be controlled is characterized by a discrete state-space realization as shown in Equation A.1 and A.2. With the exception of PD control, all controllers and the observers were designed in discrete time using state-space difference equations:

$$x[k+1] = \mathbf{\Phi}x[k] + \mathbf{\Gamma}u[k] \tag{A.1}$$

$$y[k] = \mathbf{H}x[k] \tag{A.2}$$

If the dimensions of $\mathbf{\Phi}$, $\mathbf{\Gamma}$ and $\mathbf{H}$ are $n \times n$, $n \times m$ and $l \times n$, respectively then x is an $n-$vector, u is an $m-$vector and y is an $l-$vector.

For an n^{th} order system with one input, $m = 1$, and one output, $l = 1$, the dimension of x is $n \times 1$.

A.1 Observer Implementation

Controllers were implemented using state-space realizations and utilized state feedback. Only positions and velocities were directly measured. An observer was implemented for each plant model to obtain the full state vector for state feedback.

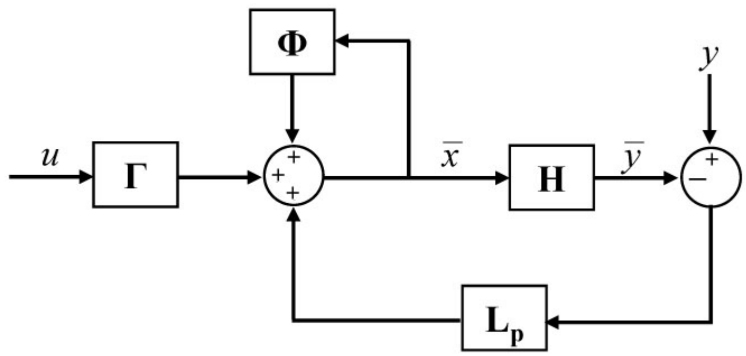

Figure A.1: Observer Block Diagram

The prediction state estimator was implemented [69]. Next cycle's state was calculated based on the current state measurements, the control effort and the error of the observer output. The equation for estimation is

$$\bar{x}[k+1] = \mathbf{\Phi}\bar{x}[k] + \mathbf{\Gamma}u[k] + \mathbf{L_p}(y[k] - \mathbf{H}\bar{x}[k]) \tag{A.3}$$

where $\bar{x}$ is the state estimate and $\mathbf{L_p}$ is the feedback gain matrix that is acquired through Ackerman's formula.

The observer poles were placed to avoid oscillation and in most cases the observer pole values were chosen between 0.5 and 0.9. See Figure A.1 for a discrete block diagram of the observer.

A.2 Position Plus Derivative Control

The only control algorithm implemented in continuous time was position-plus-derivative (PD) control. The control effort, u, was calculated according to Equation A.4:

$$u = k_p(y_{des} - y) - k_d\dot{y} \tag{A.4}$$

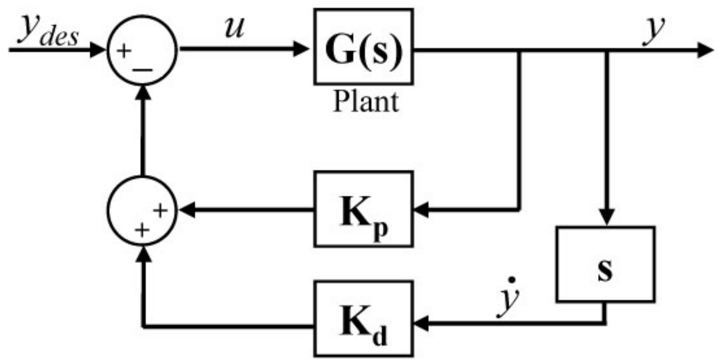

Figure A.2: Continuous PD Control Block Diagram

The output of the system is y and the desired output is y_{des}. The position and derivative gains are notated by k_p and k_d respectively. A continuous block diagram representation can be seen in Figure A.2. The speed was calculated using the state-space plant model. This model is represented using **A**, **B**, and **C** matrices. The **A** and **B** matrices relate the states and the control respectively to the derivative of the states. The **C** matrix relates the state to the system output. Note that all of the systems were strictly proper or forced to be strictly proper and hence did not contain a **D** term.

$$\dot{x} = \mathbf{A}x + \mathbf{B}u \tag{A.5}$$

$$y = \mathbf{C}x \tag{A.6}$$

$$\dot{y} = \mathbf{C}\dot{x} = \mathbf{C}(\mathbf{A}x + \mathbf{B}u) \tag{A.7}$$

By taking a time derivative of the output equation, the output velocity can be related to the state velocity. For a given state and control effort, state derivatives can be calculated from the state equation.

The states maintained their values and meaning through the continuous-to-discrete transformation. It was necessary to obtain the discrete state-space realization from the continuous time state-space realization. In the end the state was calculated using a discrete observer and then the state was used with the continuous state-space model. By obtaining the velocity in this form, the noise that would resulted from the calculation of the first-order approximation is omitted.

The gains for this algorithm were tuned by checking the RMS control and RMS error between the desired and actual position. The process of tuning the gains started by simply increasing the position gain until the buzzing of the system was the primary cause of tracking error. At this point, the derivative gain was set to cancel the buzzing. These two steps were repeated until adequate tracking was obtained and the buzzing was insignificant.

A.3 Pole-Placement Control

PD control can be seen as a variation of pole-placement (PP) control. In general, pole placement has n degrees of freedom to control (where n is the order of the system). In other words, it is possible to move all the poles of the system to any specific locations in the unit circle. PD control, however, is limited to two degrees of freedom. For systems of order $n > 2$, PD is not exercising all the degrees of freedom possible to do control. PD control will often find an acceptable set of poles, but it is likely that the controller is suboptimal.

The pole-placement algorithm used state feedback with the states obtained by the observer. The poles were placed using the discrete plant transfer function and Ackerman's formula.

The feedforward gain of the algorithm was calculated by extracting states that corresponded to the desired trajectory. These desired states were compared to the actual states in feedback. Both of these gains were calculated from the system model.

The pole-placement system block diagram can be seen in Figure A.3. Note that the following derivation was obtained from [69].

Steady-state error occurs with this algorithm for systems of type 0 or the systems

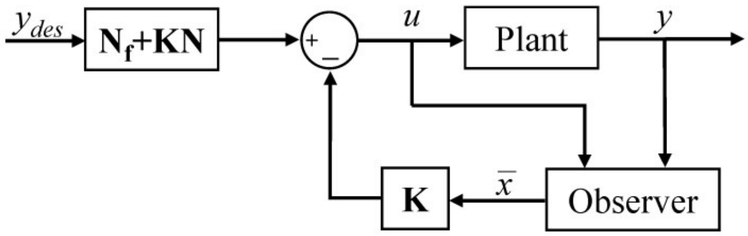

Figure A.3: Pole-Placement Control Block Diagram

that contain no poles at $s = 0$. The type of the system is defined as the number of poles at zero. Therefore, a feedforward steady-state term was added to the basic PP controller. Desired states are achieved by multiplying the desired signal with a vector:

$$\mathbf{N}y_{des} = x_{des} \tag{A.8}$$

The output is determined by the states by:

$$y = \mathbf{H}x. \tag{A.9}$$

For tracking, the desired signal should be identical to the actual signal therefore the desired states should be the same as the actual states. By making a substitution from (A.8) to (A.9), it can be seen that $\mathbf{N}$ is actually a pseudo-inverse of $\mathbf{H}$:

$$y = \mathbf{HN}y_{des} \tag{A.10}$$

$$\mathbf{HN} = \mathbf{I} \tag{A.11}$$

The steady-state term is defined as

$$u_{ss} = \mathbf{N}_f y_{des}. \tag{A.12}$$

When in steady state, the control should be tracking therefore the component from the state feedback will be completely eliminated by the state feedforward portion. This makes the state equation for steady state

$$x_{ss} = \mathbf{\Phi} x_{ss} + \mathbf{\Gamma} u_{ss}. \tag{A.13}$$

By making substitutions into the steady-state equation the following can be derived:

$$(\mathbf{\Phi} - \mathbf{I})\mathbf{N} + \mathbf{\Gamma}\mathbf{N}_f = \mathbf{0}. \tag{A.14}$$

Using (A.14) in conjunction with (A.11), a system of equations is constructed from which $\mathbf{N}$ and $\mathbf{N}_f$ can be obtained.

$$\begin{bmatrix} \mathbf{N} \\ \mathbf{N}_f \end{bmatrix} = \begin{bmatrix} \mathbf{\Phi} - \mathbf{I} & \mathbf{\Gamma} \\ \mathbf{H} & \mathbf{0} \end{bmatrix}^{-1} \begin{bmatrix} \mathbf{0} \\ \mathbf{I} \end{bmatrix} \tag{A.15}$$

Once $\mathbf{N}_f$ and $\mathbf{N}$ have been solved, the feedforward control is simply

$$u_{ff} = \mathbf{N}_f y_{des} + \mathbf{K}\mathbf{N} y_{des} \tag{A.16}$$

$$u_{ff} = (\mathbf{N}_f + \mathbf{K}\mathbf{N}) y_{des} \tag{A.17}$$

$$u_{ff} = \overline{\mathbf{N}} y_{des} \tag{A.18}$$

The matrix $\mathbf{K}$ is the set of feedback gains that are acquired through the Ackerman's formula. The complete control equation takes the form of

$$u = (\mathbf{N}_f + \mathbf{K}\mathbf{N}) y_{des} - \mathbf{K}\overline{x} \tag{A.19}$$

During the selection of the poles, selected controller poles are kept slower than the estimator poles, so that the total system response is dominated by the control poles.

A.4 Experimental Results

The results given in this section are to extend the 1-D results of Rotella [25] to 3-D. The results for the traditional controllers are presented here since this thesis mainly focuses on the design of Receding Horizon MPC. In both simulations and experiments, the same methods and reference data were used. Some slight differences in parameters were observed due to the mathematical modeling of the robot.

In PD control, position and derivative constants are tuned to minimize tracking error. Another factor for tuning was to reduce the buzzing of the actuators which was due to control signals' high frequency behavior. When the tuning was finalized the buzzing was reduced to an insignificant noise.

In PP control, the closed-loop poles were selected to find controller gains. Same goals of tuning were followed as in PD control. In this case, when the tuning was final, although the tracking error was decreased, there was a high disturbing buzzing in the motors. This was due to the high frequency control switching and high frequency oscillation of the actuators during the tracking.

In RHMPC algorithms, weighting parameters of the optimal index were tuned to minimize RMS tracking error. Parameters were selected in order to accentuate the states therefore regulate quicker with higher control efforts. Tuning was performed to avoid the high frequency resonances so that no vibration would be reflected to the structure.

For each algorithm, experiments on PHANToM robot were repeated 10 times. The deviation between the trials were very small. The maximum values for the *End-effector RMS and Maximum Position Errors* in 3-D and *RMS Control Effort* are summarized in Table A.1 to project the worst cases. These results are obtained using the first 10-s segment of the data.

Considering the RMS end-effector error, all of the controllers, that were tested for their performances, performed relatively close. Receding Horizon Model Predic-

Table A.1: End-effector Simulation and Experimental Results: *Summary of the maximum end-effector RMS position error and RMS control effort values for the PD control, PP control and RHMPC algorithms used with the first 10-s segment of the data.*

End-effector Tracking Results	*RMS Position Error*		*RMS Control Effort*	
	Simulation	PHANToM	Simulation	PHANToM
Units	mm		Nmm	
Position Plus Derivative Control	0.443	0.869	104.8	100.7
Pole Placement Control	0.656	0.784	312.3	234.8
Receding Horizon Model Predictive Control with Exact Reference Information	0.276	0.372	17.1	59.5
Receding Horizon Model Predictive Control with Reference Signal Estimation	0.640	0.815	22.5	69.7
Receding Horizon Model Predictive Control with Reference Signal Estimation Using ECG Signal	0.491	0.669	19.4	61.8

Table A.2: End-effector Simulation and Experimental Results: *Summary of the maximum end-effector RMS position error and RMS control effort values for the PD control, and RHMPC algorithms used with the 56-s long heart data. 6.519 grams were attached to the end effector of the PHANToM in order to perturb the model.*

End-effector Tracking Results	*RMS Position Error* (Max Position Error)		%Increase	*RMS Control Effort*		%Increase
	PHANToM	Perturbed		PHANToM	Perturbed	
Units	mm			Nmm		
Position Plus Derivative Control	0.849 (6.089)	0.994 (6.838)	17 (12)	96.6	99.7	3
Receding Horizon MPC with Reference Signal Estimation Using ECG Signal	0.681 (5.569)	0.767 (5.857)	12 (4)	59.8	63.6	5

tive Control with Reference Signal Estimation Using ECG Signal performed better compared to other controllers. Also, when the RMS control efforts are compared, PD and PP controllers performed poorly. The RHMPC controllers could have been pushed more to get less RMS position error. But in that case, with better tracking, relatively low control efforts would have been compromised. Also, as a result of tuning, unwanted noise in the actuators would have been introduced. Even though the RMS position errors are close, the model predictive controllers outperformed the traditional controllers.

When the tuning processes of the controllers are compared, it is seen that tuning the model predictive controller is less demanding, which supports the following statement by Garcia *et al.* [31] that RHMPC is not inherently more or less robust than classical feedback, but it can be adjusted more easily for robustness. The design of feedforward controllers is generally much simpler than that of feedback controllers, such that from a mathematical point of view, it is simpler to optimize an affine function of feedforward controller by searching all stable controllers than it is to optimize a nonlinear function of feedback controller subject to complicated constraints of closed loop stability.

The PHANToM model is perturbed from its original by adding 6.5 grams to PHANToM's end effector. Same controller parameters were used before and after the weight is added. Experiments were done using the 56-s long heart data with the PD controller and Receding Horizon Model Predictive Controller with reference signal estimation using ECG signal. The RMS position error and RMS controller effort results, and their increase percentage after the system was perturbed are tabulated in Table A.2. The position error increase for the RHMPC controller were less than the PD controller. RMS control effort of the RHMPC is less than the PD controller's control efforts, although PD controller's percent control effort increase is less than RHMPC's. These results show that RHMPC with reference signal estimation using

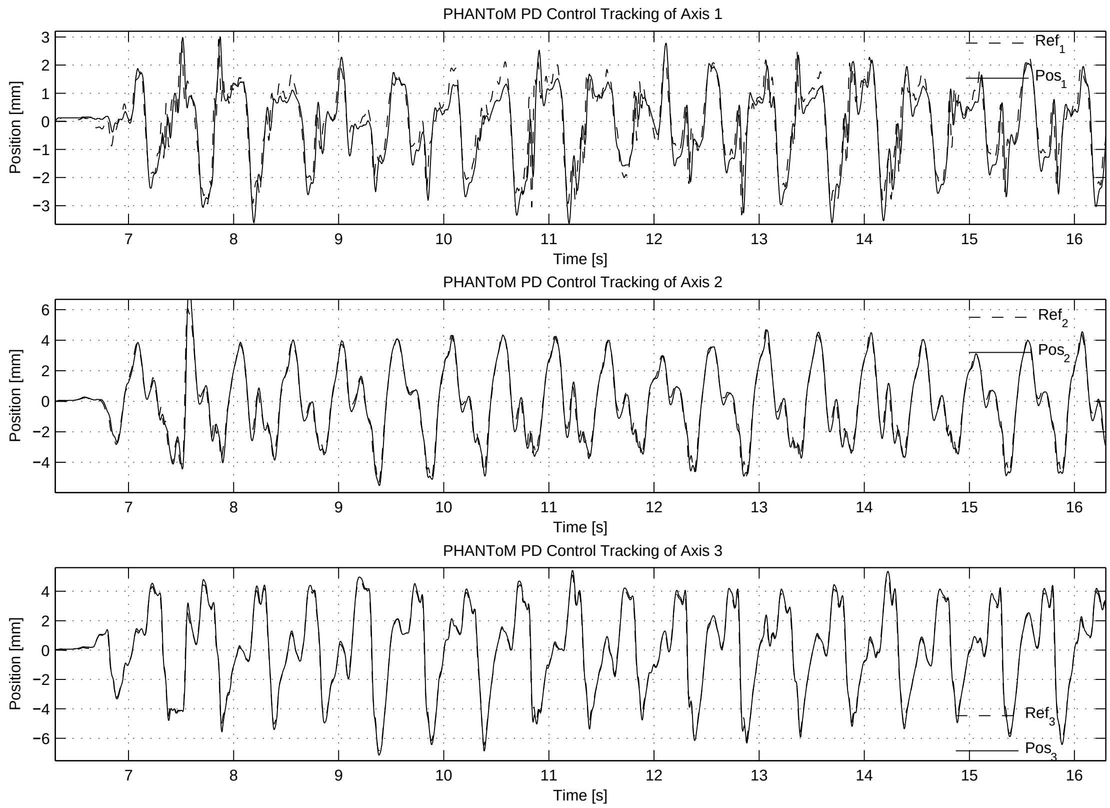

Figure A.4: PHANToM 3-D: Position Plus Derivative (PD) Control Tracking Results. Reference and Position signals of all three axes are shown.

ECG signal is more robust than the PD controller.

High jumps in the position error are due to the noisy data collected by sonometric system. It is unlikely that the POI on the heart is capable of moving 5 mm in a few milliseconds. The measured data has velocity peaks that are over 13 times faster than the maximum LAD velocity measurements reported in [46]. At these high jumps, RHMPC algorithms outperformed traditional controllers, because with the traditional controllers these jumps initiated system oscillations.

PD control and PP control tracking results for 1^{st} axis of PHANToM are shown in Figures A.5 and A.6 respectively. Reference and position plots for all axes are shown in Figures A.4 and A.7.

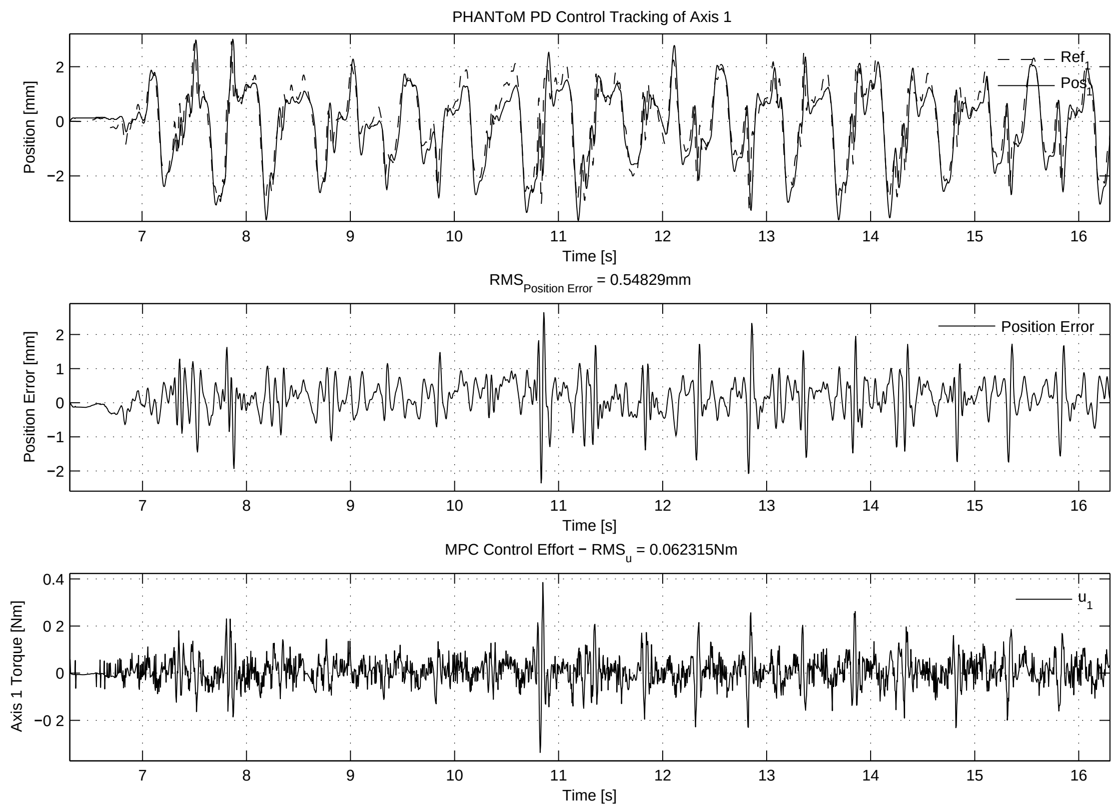

Figure A.5: PHANToM 3-D: Position Plus Derivative (PD) Control Tracking Results. Reference & Position, Position Error and Control Effort signals are shown for the 1^{st} axis.

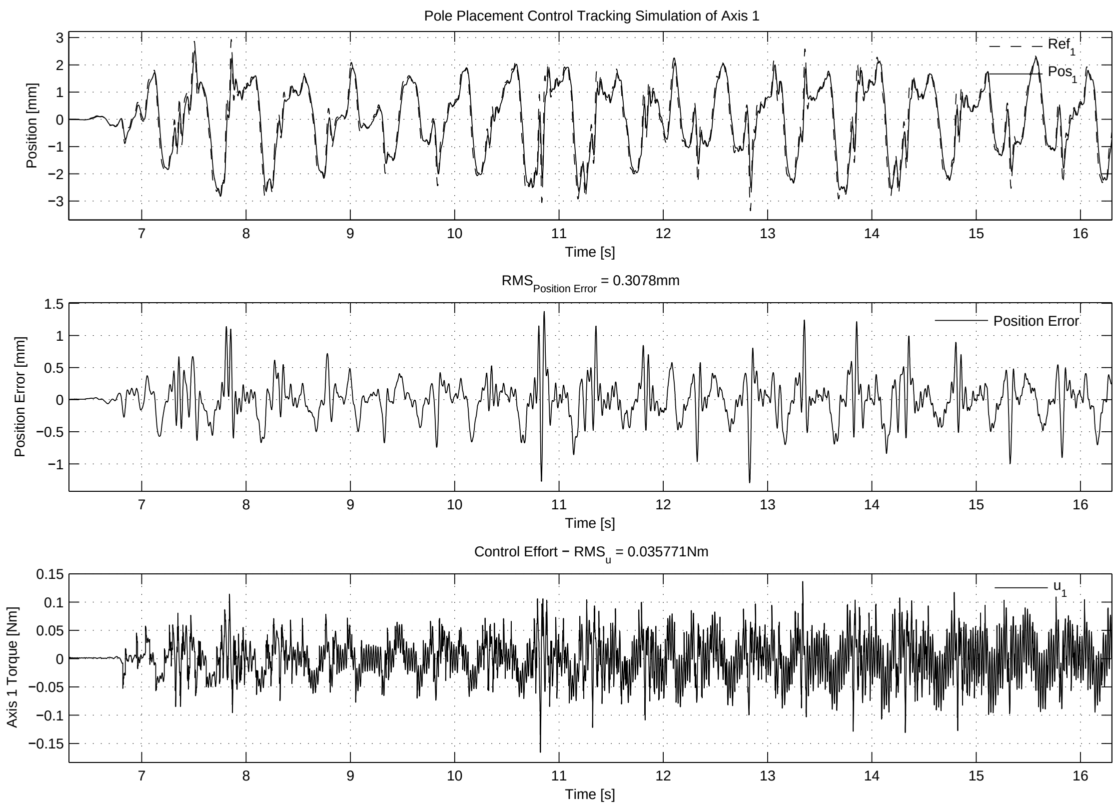

Figure A.6: PHANToM Simulation: Pole Placement (PP) Control Simulation Results. Reference & Position, Position Error and Control Effort signals are shown for the 1^{st} axis.

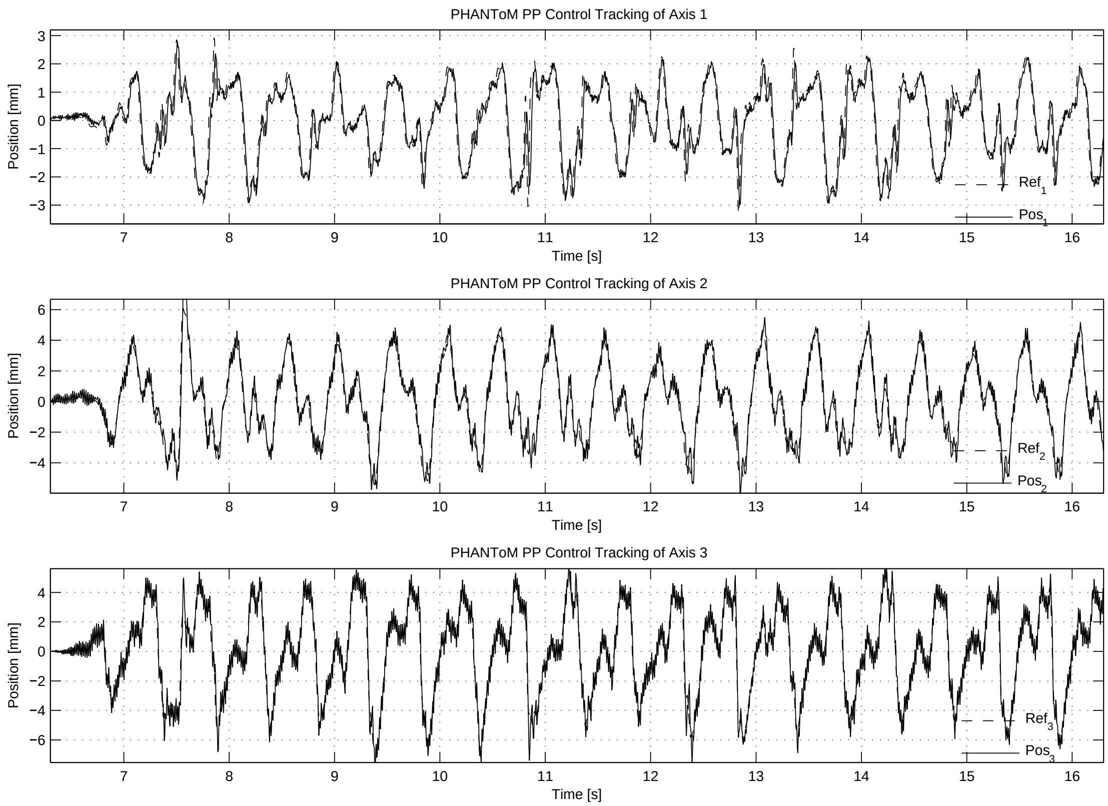

Figure A.7: PHANToM 3-D: Pole Placement (PP) Control Tracking Results. Reference and Position signals of all three axes are shown.

Appendix B

Mathematical Model of the PHANToM Robot

PHANToM Premium 1.5A was used and modeled as a hardware test bed system to develop algorithms. In modeling, experimental transfer function models for the three axes were determined. Transfer functions and their frequency response plots are given in (B.1), (B.2) and (B.3) and Figures B.1, B.3, and B.3 respectively.

Axis 1 Transfer function

$$G_1(s) = \frac{983.6s^4 + 3.037 \cdot 10^4 s^3 + 1.154 \cdot 10^8 s^2 + 1.502 \cdot 10^9 s + 2.402 \cdot 10^{12}}{s^6 + 214s^5 + 3.544 \cdot 10^5 s^4 + 1.036 \cdot 10^7 s^3 + 9.179 \cdot 10^9 s^2} \tag{B.1}$$

Axis 2 Transfer function

$$G_2(s) = \frac{2146s^4 + 2.611 \cdot 10^5 s^3 + 3.777 \cdot 10^8 s^2 + 9.557 \cdot 10^9 s + 9.735 \cdot 10^{12}}{s^6 + 263.7s^5 + 6.486 \cdot 10^5 s^4 + 1.841 \cdot 10^7 s^3 + 2.344 \cdot 10^{10} s^2} \tag{B.2}$$

Axis 3 Transfer function

$$G_3(s) = \frac{4874s^4 + 2.265 \cdot 10^6 s^3 + 2.862 \cdot 10^9 s^2 + 1.455 \cdot 10^{11} s + 9.968 \cdot 10^{13}}{s^6 + 465.8s^5 + 2.136 \cdot 10^6 s^4 + 5.575 \cdot 10^7 s^3 + 9.542 \cdot 10^{10} s^2} \quad \text{(B.3)}$$

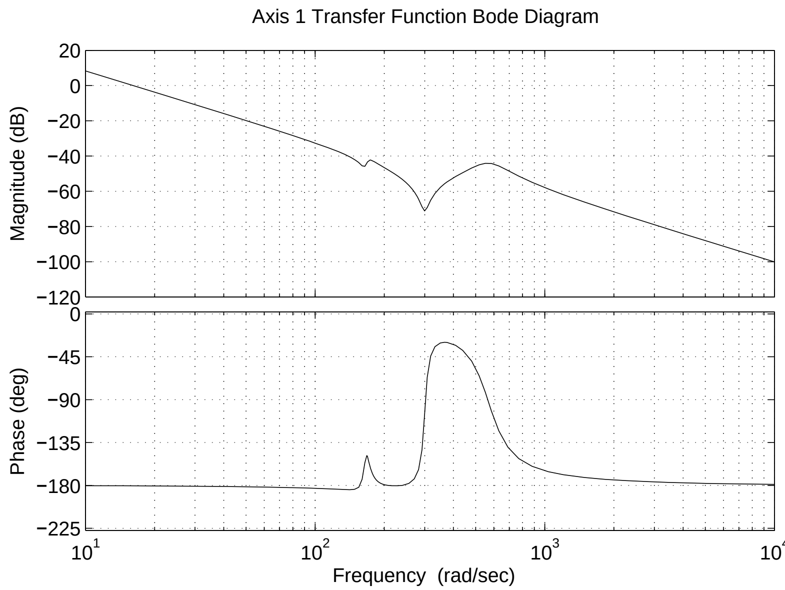

Figure B.1: Frequency Response of Axis 1

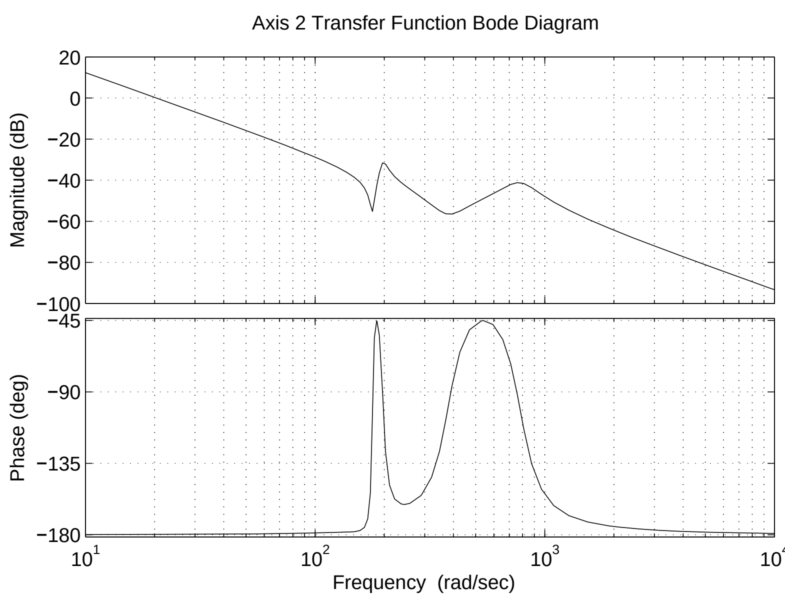

Figure B.2: Frequency Response of Axis 2

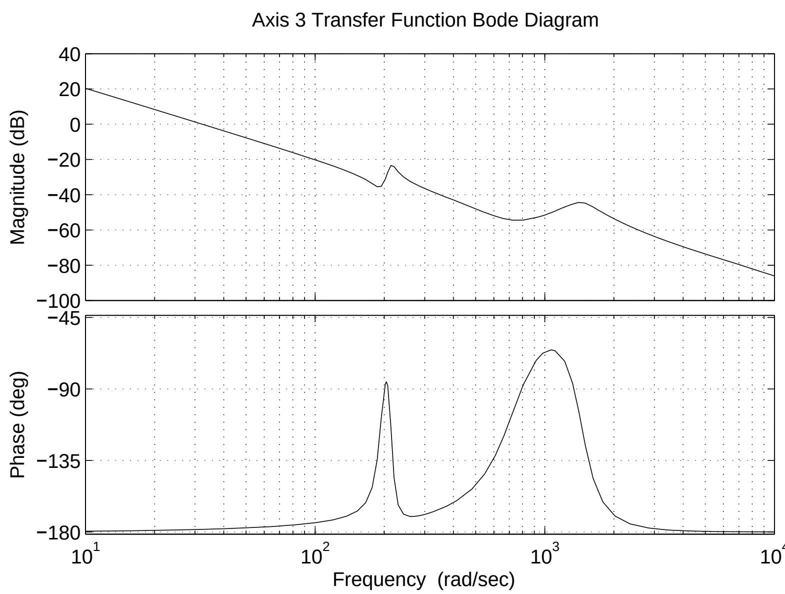

Figure B.3: Frequency Response of Axis 3

Appendix C

Geometrical Fusion Method

The sensor fusion method explained in this appendix was proposed by Nakamura *et al.* [64].

Define $\theta_i \in \mathbb{R}^{m_i}(i = 1, \ldots, p)$ as *sensory data* from the sensor unit i, where a sensory data is the low-level measurements inherent to a specific physical sensor. Here, m_i means the number of the independent measurement and p is the number of the sensor units. Also, $x_i \in \mathbb{R}^n, i = 1, \ldots, p$ is called *sensory information* which is computed from sensory data θ_i. Here n is the dimension of the sensory information. A general representation for x_i is:

$$x_i = f_i(\theta_i) \tag{C.1}$$

where it was assumed that $n \leq m_i$.

Equation (C.1) can be used as a general model of the sensors that would track the point-of-interest (POI) on the heart.

C.1 Uncertainty Ellipsoid

Note that θ_i is defined as low level sensory information whose physical meaning is defined by the inherent structure of a specific sensor.

Adding statistical disturbances to the low level sensory data rather than adding to the processed information, such as coordinate frames, is a more realistic assumption to model the disturbances.

The disturbance or uncertainly included in the sensory data is assumed additive as follows,

$$\theta_i = \underline{\theta_i} + \delta\theta_i \tag{C.2}$$

where $\underline{\theta_i} \in \mathbb{R}^{m_i}(i = 1, \ldots, p)$ is the true (undisturbed) value of the data and $\delta\theta_i \in \mathbb{R}^{m_i}(i = 1, \ldots, p)$ is the disturbance, and assumed Gaussian distribution to $\delta\theta_i$ is,

$$E(\delta\theta_i) = \overline{\delta\theta_i} = 0 \in \mathbb{R}^{m_i} \tag{C.3}$$

$$V(\delta\theta_i) \triangleq E((\delta\theta_i - \overline{\delta\theta_i})(\delta\theta_i - \overline{\delta\theta_i})^T) = \mathbf{Q}_i = diag(\sigma_{i,1}^2, \ldots, \sigma_{i,m_i}^2) \in \mathbb{R}^{m_i \times m_i} \tag{C.4}$$

where $E(*)$ is *expectation* of $*$, and also assume that $\delta\theta_{i,j}$ $(j = 1, \ldots, m_i)$, the j^{th} element of $\delta\theta_i$, is not correlated and $\sigma_{i,j}^2$ is the variance of $\delta\theta_{i,j}$. $\mathbf{Q}_i$ is the covariance matrix of $\delta\theta_i$. Substitute (C.2) into (C.1),

$$x_i = f_i(\underline{\theta_i} + \delta\theta_i). \tag{C.5}$$

If, $\delta\theta_i$ is small enough (C.5) can be approximated by,

$$x_i = f_i(\underline{\theta_i}) + \mathbf{J}_i(\theta_i)\delta\theta_i \tag{C.6}$$

$$\mathbf{J}_i(\theta_i) = \frac{\delta f_i}{\delta\theta_i} \in \mathbb{R}^{n \times m_i} \tag{C.7}$$

where $\mathbf{J}_i(\theta_i)$ is the Jacobian matrix of f_i with respect to θ_i. Then expectation and covariance matrix of x_i become,

$$E(x_i) = \overline{x_i} = f_i(\underline{\theta_i}) \tag{C.8}$$

$$V(x_i) = E\Big((x_i - \overline{x_i})(x_i - \overline{x_i})^T\Big) = \mathbf{J}_i\mathbf{Q}_i\mathbf{J}_i^T \tag{C.9}$$

(C.8) implies that after infinite number of measurements, the average is equal to the true value of x_i. Here, it was assumed that the calibration error is neglected, the focus here is the local errors, assumed as statistical uncertainty.

In (C.9) covariance of x_i is not diagonal anymore. Since jacobian is not diagonal in general. For a full rank $\mathbf{J}_i$, $\mathbf{J}_i\mathbf{Q}_i\mathbf{J}_i^T$ is positive definite since $\mathbf{Q}_i$ is positive definite. Also, $\mathbf{J}_i\mathbf{Q}_i\mathbf{J}_i^T$ is symmetric, and its singular value decomposition can be represented by,

$$\mathbf{J}_i\mathbf{Q}_i\mathbf{J}_i^T = \mathbf{U}_i\mathbf{D}_i\mathbf{U}_i^T \tag{C.10}$$

$$\mathbf{U}_i = [e_{i,1} \cdots e_{i,n}] \in \mathbb{R}^{n\times n}, (e_{i,j})(e_{i,k})^T = \begin{cases} 1 \text{ for}, & j = k \\ 0 \text{ for}, & j \neq k \end{cases} \tag{C.11}$$

$$\mathbf{D}_i = diag\,(d_{i,1}, \ldots, d_{i,n}), \quad d_{i,1} \geq d_{i,2} \geq \ldots \geq d_{i,n} \geq 0 \tag{C.12}$$

where $\mathbf{U}$ is an orthogonal matrix and $d_{i,j}$ $(j = 1, \ldots, n)$ are the singular values of $\mathbf{J}_i\mathbf{Q}_i\mathbf{J}_i^T$. The scalar variance in the direction of unit vector e_i is

$$V\Big((e_{i,j})^T(x_i)\Big) = d_{i,j}. \tag{C.13}$$

Therefore $\sqrt{d_{i,j}}$ represents the uncertainty of x_i in the direction of $e_{i,j}$. So the distribution of variances in all directions form an ellipsoid with $e_{i,j}$ as the principle axes with lengths of $2\sqrt{d_{i,j}}$. A three dimensional case is shown in Figure C.1. The ellipsoid shown is called an “uncertainty ellipsoid.” In parallel to the singular val-

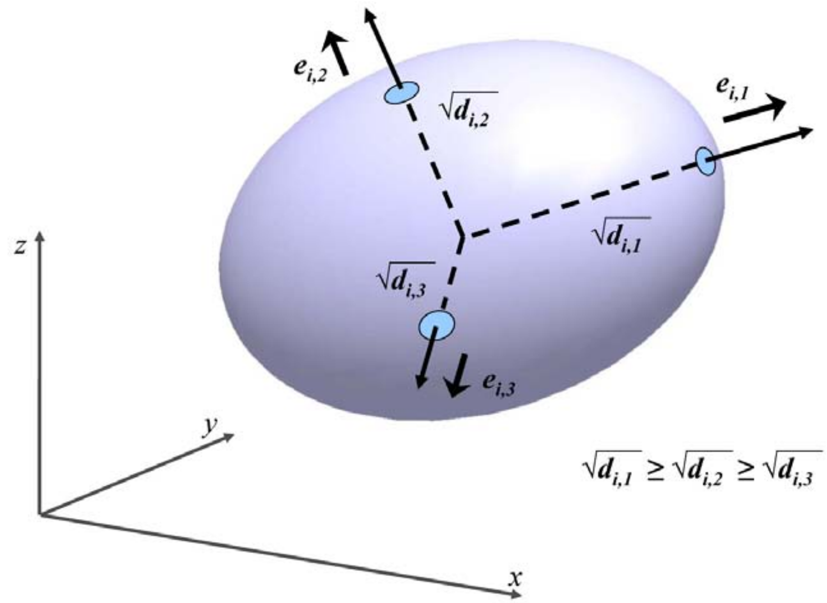

Figure C.1: Uncertainty Ellipsoid.

ues, the most uncertain direction is $e_{i,1}$ with uncertainty $\sqrt{d_{i,1}}$, and $e_{i,3}$ is the least uncertain one with uncertainty $\sqrt{d_{i,3}}$.

C.2 Geometrical Fusion Method

Information from multiple sensors, x_i could be fused to get consensus x with linear combination,

$$x = \sum_{i=1}^{p} \mathbf{W}_i \, x_i \tag{C.14}$$

where $\mathbf{W}_i \in \mathbb{R}^{n \times n}$ is the weighting matrix. The shape of the uncertainty ellipsoid depends on the selection of the weighting matrix. The mean of the x is computed as:

$$E(x) = \sum_{i=1}^{p} \mathbf{W}_i \, E(x_i) = \sum_{i=1}^{p} \mathbf{W}_i \, \overline{x_i} \tag{C.15}$$

Since no calibration error was assumed, $\overline{x_i}$ is equal to $\overline{x}$, so (C.15) becomes,

$$E(x) = \left(\sum_{i=1}^{p} \mathbf{W}_i \right) \overline{x} \tag{C.16}$$

Also from (C.8),

$$E(x) = \overline{x}. \tag{C.17}$$

Therefore weighting should satisfy,

$$\sum_{i=1}^{p} \mathbf{W}_i = \mathbf{I} \tag{C.18}$$

where $\mathbf{I} \in \mathbb{R}^{n \times n}$ is an identity matrix.

Also using (C.6), (C.8), (C.14), and (C.18) and $\overline{x_i} = \overline{x}$, the covariance matrix of x is given by,

$$V(x) = E\Big((x - \overline{x})(x - \overline{x})^T\Big) = \mathbf{W}\mathbf{Q}\mathbf{W}^T \in \mathbb{R}^{n \times n} \tag{C.19}$$

$$\mathbf{W} \triangleq (\mathbf{W_1}\,\mathbf{W_2}\,\ldots\,\mathbf{W_p}) \in \mathbb{R}^{n \times pn} \tag{C.20}$$

$$\mathbf{Q} \triangleq \begin{pmatrix} \mathbf{J}_1\mathbf{Q}_1\mathbf{J}_1^T & \cdots & \mathbf{0} \\ \vdots & \ddots & \vdots \\ \mathbf{0} & \cdots & \mathbf{J}_p\mathbf{Q}_p\mathbf{J}_p^T \end{pmatrix} \in \mathbb{R}^{pn \times pn} \tag{C.21}$$

In the derivation of (C.19) uncertainty of the sensor units, $\delta\theta_i$ and $\delta\theta_j$, are assumed to be uncorrelated.

To get the most accurate and least uncertain sensory information, we should find the weighting matrix, $\mathbf{W}$, that minimizes the uncertainty ellipsoid. Singular value decomposition of the covariance matrix of x is,

$$\begin{aligned} \mathbf{W}\mathbf{Q}\mathbf{W}^T &= \mathbf{U}\mathbf{D}\mathbf{U}^T \\ \mathbf{U} &= [e_1 \cdots e_n] \in \mathbb{R}^{n \times n}, \quad e_j \in \mathbb{R}^n \\ \mathbf{D} &= diag\,(d_1, \ldots, d_n), \quad d_{i,1} \geq d_{i,2} \geq \ldots \geq d_{i,n} > 0 \end{aligned} \tag{C.22}$$

where $2\sqrt{d_{i,j}}$ is the length of the i^{th} longest principle axis of the uncertainty ellipsoid of the fused sensory information, x, and unit vector e_i represents its direction.

The geometric volume calculation of an ellipsoid is as follows

$$
\begin{aligned}
Volume &= \frac{\pi^{\frac{p}{2}}}{\Gamma(1+\frac{p}{2})}\left(\prod_{i=1}^{p} d_i\right)^{\frac{1}{2}} \\
Volume &= \frac{\pi^{\frac{p}{2}}}{\Gamma(1+\frac{p}{2})}\sqrt{det(\mathbf{WQW}^T)}
\end{aligned}
\tag{C.23}
$$

where Gamma function is defined as

$$
\begin{aligned}
\Gamma(\alpha) &= \int_0^\infty e^{-t} t^{\alpha-1} dt \\
\Gamma(1+\frac{p}{2}) &= \int_0^\infty e^{-t} t^{\frac{p}{2}} dt.
\end{aligned}
$$

Hence, minimizing volume is equivalent to minimizing the determinant of covariance matrix,

$$
min(Volume) \equiv min\left(\frac{\pi^{\frac{p}{2}}}{\int_0^\infty e^{-t} t^{\frac{p}{2}} dt}\sqrt{det(\mathbf{WQW}^T)}\right) \equiv min\Big(det\big(\mathbf{WQW}^T\big)\Big).
$$

Then, the minimization problem turns into,

$$
\min\ Z = det\Big(\mathbf{WQW}^T\Big) \quad \text{s.t. } \sum_{i=1}^{p} \mathbf{W}_i = \mathbf{I} \tag{C.24}
$$

This problem can be solved with Lagrange multipliers,

$$
\min\ Z^* = det\Big(\mathbf{WQW}^T\Big) + P \tag{C.25}
$$

$$
P = \sum_{i=1}^{n}\sum_{j=1}^{n} \lambda_{ij}\left(\sum_{k=1}^{p} \mathbf{W}_{k,ij} - \delta_{ij}\right) \tag{C.26}
$$

$$
\delta_{ij} = \begin{cases} 1 \text{ for } & i = j \\ 0 \text{ for } & i \neq j \end{cases} \qquad \mathbf{\Lambda} \triangleq \begin{pmatrix} \lambda_{11} & \cdots & \lambda_{1n} \\ \vdots & \ddots & \vdots \\ \lambda_{n1} & \cdots & \lambda_{nn} \end{pmatrix} \tag{C.27}
$$

where $\mathbf{W}_{k,ij}$ is the (i,j) element of the $\mathbf{W}_k$, λ_{ij} are the Lagrangian multipliers and in order to minimize Z^*, $\left(\sum_{k=1}^{p} \mathbf{W}_{k,ij} - \delta_{ij}\right)$ should be zero. Also $\mathbf{W}$ must satisfy,

$$\frac{\partial Z^*}{\partial \mathbf{W}} = \begin{pmatrix} \frac{\partial Z^*}{\partial \mathbf{W}_1} \\ \vdots \\ \frac{\partial Z^*}{\partial \mathbf{W}_p} \end{pmatrix} = 0 \tag{C.28}$$

Lagrange multipliers are derived as,

$$\mathbf{\Lambda} = -2\ det\Big(\mathbf{WQW}^T\Big)\Big(\mathbf{WQW}^T\Big)^{-1}\left\{\sum_{i=1}^{p}\Big(\mathbf{J}_i\mathbf{Q}_i\mathbf{J}_i^T\Big)^{-1}\right\}^{-1} \tag{C.29}$$

Finally the weighting matrices and the covariance of x are,

$$\mathbf{W}_i = \left\{\sum_{j=1}^{p}\Big(\mathbf{J}_j\mathbf{Q}_j\mathbf{J}_j^T\Big)^{-1}\right\}^{-1}\Big(\mathbf{J}_i\mathbf{Q}_i\mathbf{J}_i^T\Big)^{-1} \tag{C.30}$$

$$V(x) = \left\{\sum_{i=1}^{p}\Big(\mathbf{J}_i\mathbf{Q}_i\mathbf{J}_i^T\Big)^{-1}\right\}^{-1} \tag{C.31}$$

C.3 Computation of Multi Sensor Information Fusion

Assume that x^* is the fusion of $x_1, x_2, \ldots, x_p, x_{p+1}$. In order to find the relation for fusing x and x_{p+1} to get the resultant sensor information x^*, where x is the fusion of $x_1, x_2, \ldots, x_p$ the following derivation is followed.

Define covariance of x_i as $\mathbf{H}_i$, then from (C.31), covariance of x is

$$\mathbf{H} \triangleq V(x) = \left\{\sum_{i=1}^{p}\Big(\mathbf{H}_i\Big)^{-1}\right\}^{-1} \tag{C.32}$$

then (C.30) can be written as,

$$\mathbf{W}_i = \left\{ \sum_{i=1}^{p} \big(\mathbf{H}_i\big)^{-1} \right\}^{-1} \big(\mathbf{H}_i\big)^{-1} = \mathbf{H}\big(\mathbf{H}_i\big)^{-1} \tag{C.33}$$

also, for x^*, (C.14) becomes,

$$\begin{aligned} x^* &= \sum_{i=1}^{p+1} \mathbf{H}^* \big(\mathbf{H}_i\big)^{-1} x_i \\ &= \mathbf{H}^* \sum_{i=1}^{p+1} \big(\mathbf{H}_i\big)^{-1} x_i \\ &= \mathbf{H}^* \big(\mathbf{H}^{-1} x + \mathbf{H}_{p+1}^{-1} x_{p+1}\big) \\ &= \left\{\mathbf{H}^{-1} + \mathbf{H}_{p+1}^{-1}\right\}^{-1} \Big(\mathbf{H}^{-1} x + \mathbf{H}_{p+1}^{-1} x_{p+1}\Big) \\ x^* &= \sum_{i=1}^{p+1} \left\{ \sum_{j=1}^{p+1} \mathbf{H}_j^{-1} \right\}^{-1} \mathbf{H}_i^{-1} x_i \end{aligned} \tag{C.34}$$

(C.34) implies that fusion of x and x_{p+1} is equivalent to fusion of $x_1, x_2, \ldots, x_p$, and x_{p+1}. Also note that, the fusion described here is a geometrical summation of the uncertainty ellipsoids, therefore the order of i does not matter. Hence, the following recursive computation scheme can be used for multi sensor information fusion:

Step 0. Initialize: $x = 0$, $\mathbf{H}^{-1} = 0$

Step 1. $x_a = x$, $\mathbf{H}_a^{-1} = \mathbf{H}^{-1}$

$x_b = x_i$, $\mathbf{H}_b^{-1} = \mathbf{H_i}^{-1}$

Step 2. $x = \left\{\mathbf{H}_a^{-1} + \mathbf{H}_b^{-1}\right\}^{-1} \Big(\mathbf{H}_a^{-1} x_a + \mathbf{H}_b^{-1} x_b\Big)$

$\mathbf{H}^{-1} = \mathbf{H}_a^{-1} + \mathbf{H}_b^{-1}$

Step 3. Go to **Step 1** for next i

In this procedure order of the fused sensors is not important. Best estimate of the x can be obtained using the already fused information x_i at any stage. These properties of the algorithm permits to use sensors with different sampling frequencies. Therefore, the sensor unit with faster response can be fused earlier than the ones with slower response. Change of number of fused sensors does not create any inconsistencies which allows asynchronous fusion computations.

Appendix D

Sonomicrometer Least Squares Equations

For each transducer quartet, the position of the crystal attached on the point of interest (POI) is calculated relative to the three crystals fixed on the base. First crystal on the base is selected as the origin of the coordinate frame. Second crystal forms the x-axis with the crystal at the origin, and the third crystal forms the xy-plane together with the x-axis. Four different coordinate frames, $(\alpha, \beta, \gamma, \delta)$, from five base crystals can be formed:

$$\begin{array}{llll} \alpha_1: \; 1-2-3 & \beta_1: \; 1-3-4 & \gamma_1: \; 2-3-4 & \delta_1: \; 4-5-1 \\ \alpha_2: \; 1-2-4 & \beta_2: \; 1-3-5 & \gamma_2: \; 2-3-5 & \delta_2: \; 4-5-2 \\ \alpha_3: \; 1-2-5 & & & \delta_3: \; 4-5-3 \end{array} \tag{D.1}$$

Let position of the fourth crystal be $P(x,\ y,\ z)$; $\mathbf{x} = \begin{bmatrix} x & y \end{bmatrix}^T$ denote the xy-coordinates with respect to the coordinate frame; and d be the measured distance between two crystals. If $\mathbf{x}$ is known, the distance of the fourth crystal from the base frame, z, can be calculated from raw intertransducer measurements using trigonometry. The position of the forth crystal can be calculated as:

$$\underbrace{\begin{bmatrix} 2x_2 & 2y_2 \\ 2x_3 & 2y_3 \end{bmatrix}}_{\mathbf{A}_1} \underbrace{\begin{bmatrix} x \\ y \end{bmatrix}}_{\mathbf{x}_\alpha} = \underbrace{\begin{bmatrix} d_1^2 - d_2^2 + x_2^2 + y_2^2 \\ d_1^2 - d_3^2 + x_3^2 + y_3^2 \end{bmatrix}}_{\mathbf{b}_1} \tag{D.2}$$

$$z = +\sqrt{d_3^2 - x^2 - y^2} \tag{D.3}$$

Then for n possible measurements, there are n linear equations.

$$\begin{aligned} \mathbf{A}_1\mathbf{x}_1 &= \mathbf{b}_1 \\ \mathbf{A}_2\mathbf{x}_2 &= \mathbf{b}_2 \\ &\vdots \\ \mathbf{A}_n\mathbf{x}_n &= \mathbf{b}_n \end{aligned} \tag{D.4}$$

Similar solutions can be grouped under the same coordinate frame such as:

$$\mathbf{x}_n = \begin{cases} \mathbf{x}_\alpha, & n = 1, 2, 3 \\ \mathbf{x}_\beta, & n = 4, 5 \\ \mathbf{x}_\gamma, & n = 6, 7 \\ \mathbf{x}_\delta, & n = 8, 9, 10 \end{cases}$$

$$\begin{array}{cccc} \mathbf{A}_1\mathbf{x}_\alpha = \mathbf{b}_1 & \mathbf{A}_4\mathbf{x}_\beta = \mathbf{b}_4 & \mathbf{A}_6\mathbf{x}_\gamma = \mathbf{b}_6 & \mathbf{A}_8\mathbf{x}_\delta = \mathbf{b}_8 \\ \mathbf{A}_2\mathbf{x}_\alpha = \mathbf{b}_2 & \mathbf{A}_5\mathbf{x}_\beta = \mathbf{b}_5 & \mathbf{A}_7\mathbf{x}_\gamma = \mathbf{b}_7 & \mathbf{A}_9\mathbf{x}_\delta = \mathbf{b}_9 \\ \mathbf{A}_3\mathbf{x}_\alpha = \mathbf{b}_3 & & & \mathbf{A}_{10}\mathbf{x}_\delta = \mathbf{b}_{10} \end{array} \tag{D.5}$$

Let $\mathbf{g}$ be a homogeneous transformation matrix

$$\mathbf{g} = \begin{bmatrix} \mathbf{R} & \mathbf{p} \\ 0\ 0 & 1 \end{bmatrix} \tag{D.6}$$

where position vector $\mathbf{p}$ describes translations with respect to a reference frame, and orientation matrix $\mathbf{R}$ describes rotations. Then inverse transformation matrix of $\mathbf{g}$ is

$$\mathbf{g}^{-1} = \begin{bmatrix} \mathbf{R}^T & -\mathbf{R}^T\mathbf{p} \\ 0\ 0 & 1 \end{bmatrix} \tag{D.7}$$

Using the transformation matrices, all of the measurements can be expressed under the same coordinate frame.

$$\begin{gathered} \mathbf{g}_{\alpha\beta}\begin{bmatrix} \mathbf{x}_\beta \\ 1 \end{bmatrix} = \begin{bmatrix} \mathbf{x}_\alpha \\ 1 \end{bmatrix} \longrightarrow \begin{bmatrix} \mathbf{x}_\beta \\ 1 \end{bmatrix} = \mathbf{g}_{\alpha\beta}^{-1}\begin{bmatrix} \mathbf{x}_\alpha \\ 1 \end{bmatrix} \\ \mathbf{g}_{\alpha\gamma}\begin{bmatrix} \mathbf{x}_\gamma \\ 1 \end{bmatrix} = \begin{bmatrix} \mathbf{x}_\alpha \\ 1 \end{bmatrix} \longrightarrow \begin{bmatrix} \mathbf{x}_\gamma \\ 1 \end{bmatrix} = \mathbf{g}_{\alpha\gamma}^{-1}\begin{bmatrix} \mathbf{x}_\alpha \\ 1 \end{bmatrix} \\ \mathbf{g}_{\alpha\delta}\begin{bmatrix} \mathbf{x}_\delta \\ 1 \end{bmatrix} = \begin{bmatrix} \mathbf{x}_\alpha \\ 1 \end{bmatrix} \longrightarrow \begin{bmatrix} \mathbf{x}_\delta \\ 1 \end{bmatrix} = \mathbf{g}_{\alpha\delta}^{-1}\begin{bmatrix} \mathbf{x}_\alpha \\ 1 \end{bmatrix} \end{gathered} \tag{D.8}$$

Lets define a truncated transformation matrix $\widetilde{\mathbf{g}}$ and its identity as

$$\widetilde{\mathbf{g}}^{-1} = \begin{bmatrix} \mathbf{R}^T & -\mathbf{R}^T\mathbf{p} \end{bmatrix} \tag{D.9}$$

$$\widetilde{\mathbf{I}} = \begin{bmatrix} 1 & 0 & 0 \\ 0 & 1 & 0 \end{bmatrix} \tag{D.10}$$

$$
\begin{aligned}
\mathbf{A}_n\mathbf{x}_\alpha = \mathbf{b}_n &\longrightarrow \mathbf{A}_n\widetilde{\mathbf{I}}\begin{bmatrix}\mathbf{x}_\alpha\\ 1\end{bmatrix} = \mathbf{b}_n, \qquad && n = 1,2,3\\
\mathbf{A}_n\mathbf{x}_\beta = \mathbf{b}_n &\longrightarrow \mathbf{A}_n\widetilde{\mathbf{g}}_{\alpha\beta}^{-1}\begin{bmatrix}\mathbf{x}_\alpha\\ 1\end{bmatrix} = \mathbf{b}_n, \qquad && n = 4,5\\
\mathbf{A}_n\mathbf{x}_\gamma = \mathbf{b}_6 &\longrightarrow \mathbf{A}_n\widetilde{\mathbf{g}}_{\alpha\gamma}^{-1}\begin{bmatrix}\mathbf{x}_\alpha\\ 1\end{bmatrix} = \mathbf{b}_n, \qquad && n = 6,7\\
\mathbf{A}_n\mathbf{x}_\delta = \mathbf{b}_n &\longrightarrow \mathbf{A}_n\widetilde{\mathbf{g}}_{\alpha\delta}^{-1}\begin{bmatrix}\mathbf{x}_\alpha\\ 1\end{bmatrix} = \mathbf{b}_n, \qquad && n = 8,9,10
\end{aligned}
\tag{D.11}
$$

Then, all equations can be combined into a single linear equation as

$$
\begin{matrix}
\mathbf{A}_1\widetilde{\mathbf{I}}\mathbf{x}_\alpha = \mathbf{b}_1\\
\vdots\\
\mathbf{A}_4\widetilde{\mathbf{g}}_{\alpha\beta}^{-1}\begin{bmatrix}\mathbf{x}_\alpha\\ 1\end{bmatrix} = \mathbf{b}_4\\
\vdots\\
\mathbf{A}_6\widetilde{\mathbf{g}}_{\alpha\gamma}^{-1}\begin{bmatrix}\mathbf{x}_\alpha\\ 1\end{bmatrix} = \mathbf{b}_6\\
\vdots\\
\mathbf{A}_8\widetilde{\mathbf{g}}_{\alpha\delta}^{-1}\begin{bmatrix}\mathbf{x}_\alpha\\ 1\end{bmatrix} = \mathbf{b}_8\\
\vdots\\
\mathbf{A}_{10}\widetilde{\mathbf{g}}_{\alpha\delta}^{-1}\begin{bmatrix}\mathbf{x}_\alpha\\ 1\end{bmatrix} = \mathbf{b}_{10}
\end{matrix}
\equiv
\begin{bmatrix}
\mathbf{A}_1\widetilde{\mathbf{I}}\\
\vdots\\
\mathbf{A}_4\widetilde{\mathbf{g}}_{\alpha\beta}^{-1}\\
\vdots\\
\mathbf{A}_6\widetilde{\mathbf{g}}_{\alpha\gamma}^{-1}\\
\vdots\\
\mathbf{A}_8\widetilde{\mathbf{g}}_{\alpha\delta}^{-1}\\
\vdots\\
\mathbf{A}_{10}\widetilde{\mathbf{g}}_{\alpha\delta}^{-1}
\end{bmatrix}
\begin{bmatrix}x_0\\ y_0\\ 1\end{bmatrix}
=
\begin{bmatrix}\mathbf{b}_1\\ \mathbf{b}_2\\ \vdots\\ \mathbf{b}_{10}\end{bmatrix}
\tag{D.12}
$$

$$
\left(\begin{bmatrix} \mathbf{A}_1\widetilde{\mathbf{I}} \\ \vdots \\ \mathbf{A}_4\widetilde{\mathbf{g}}_{\alpha\beta}^{-1} \\ \vdots \\ \mathbf{A}_6\widetilde{\mathbf{g}}_{\alpha\gamma}^{-1} \\ \vdots \\ \mathbf{A}_8\widetilde{\mathbf{g}}_{\alpha\delta}^{-1} \\ \vdots \\ \mathbf{A}_{10}\widetilde{\mathbf{g}}_{\alpha\delta}^{-1} \end{bmatrix} \widetilde{\mathbf{I}}_1 \begin{bmatrix} x_0 \\ y_0 \end{bmatrix} + \begin{bmatrix} \mathbf{A}_1\widetilde{\mathbf{I}} \\ \vdots \\ \mathbf{A}_4\widetilde{\mathbf{g}}_{\alpha\beta}^{-1} \\ \vdots \\ \mathbf{A}_6\widetilde{\mathbf{g}}_{\alpha\gamma}^{-1} \\ \vdots \\ \mathbf{A}_8\widetilde{\mathbf{g}}_{\alpha\delta}^{-1} \\ \vdots \\ \mathbf{A}_{10}\widetilde{\mathbf{g}}_{\alpha\delta}^{-1} \end{bmatrix} \widetilde{\mathbf{I}}_2 \right) = \begin{bmatrix} \mathbf{b}_1 \\ \mathbf{b}_2 \\ \vdots \\ \mathbf{b}_{10} \end{bmatrix} \tag{D.13}
$$

where

$$
\widetilde{\mathbf{I}}_1 = \begin{bmatrix} 1 & 0 \\ 0 & 1 \\ 0 & 0 \end{bmatrix} \quad \textit{and} \quad \widetilde{\mathbf{I}}_2 = \begin{bmatrix} 0 \\ 0 \\ 1 \end{bmatrix}. \tag{D.14}
$$

$$
\underbrace{\left(\begin{bmatrix} \mathbf{A}_1\widetilde{\mathbf{I}} \\ \vdots \\ \mathbf{A}_4\widetilde{\mathbf{g}}_{\alpha\beta}^{-1} \\ \vdots \\ \mathbf{A}_6\widetilde{\mathbf{g}}_{\alpha\gamma}^{-1} \\ \vdots \\ \mathbf{A}_8\widetilde{\mathbf{g}}_{\alpha\delta}^{-1} \\ \vdots \\ \mathbf{A}_{10}\widetilde{\mathbf{g}}_{\alpha\delta}^{-1} \end{bmatrix} \widetilde{\mathbf{I}}_1 \right)}_{\mathbf{A}} \begin{bmatrix} x_0 \\ y_0 \end{bmatrix} = \underbrace{\begin{bmatrix} \mathbf{b}_1 \\ \vdots \\ \mathbf{b}_4 \\ \vdots \\ \mathbf{b}_6 \\ \vdots \\ \mathbf{b}_8 \\ \vdots \\ \mathbf{b}_{10} \end{bmatrix} - \begin{bmatrix} \mathbf{A}_1\widetilde{\mathbf{I}} \\ \vdots \\ \mathbf{A}_4\widetilde{\mathbf{g}}_{\alpha\beta}^{-1} \\ \vdots \\ \mathbf{A}_6\widetilde{\mathbf{g}}_{\alpha\gamma}^{-1} \\ \vdots \\ \mathbf{A}_8\widetilde{\mathbf{g}}_{\alpha\delta}^{-1} \\ \vdots \\ \mathbf{A}_{10}\widetilde{\mathbf{g}}_{\alpha\delta}^{-1} \end{bmatrix} \widetilde{\mathbf{I}}_2}_{\mathbf{b}} \tag{D.15}
$$

Using linear least squares, a solution to $\mathbf{Ax} = \mathbf{b}$ can be found as:

$$\mathbf{x} = (\mathbf{A}^T\mathbf{A})^{-1}\mathbf{A}^T\mathbf{b} \tag{D.16}$$

Related Publications

Journal Articles

O. Bebek and M. C. Cavusoglu, "Intelligent control algorithms for robotic assisted beating heart surgery," *IEEE Transactions on Robotics*, vol. 23, no. 3, pp. 468–480, June 2007.

O. Bebek and M. C. Cavusoglu, "Whisker-like position sensor for measuring physiological motion," *IEEE/ASME Transactions on Mechatronics*, 2007, (Under review).

Conference Papers

O. Bebek and M. C. Cavusoglu, "Predictive control algorithms using biological signals for active relative motion canceling in robotic assisted heart surgery," in *Proc. of the International Conference on Robotics and Automation (ICRA)*, Orlando, FL, USA, May 2006, pp. 237–244.

O. Bebek and M. C. Cavusoglu, "Model based control algorithms for robotic assisted beating heart surgery," in *Proc. of the 28th Annual International Conference of the IEEE Engineering in Medicine and Biology Society (EMBC)*, New York, USA, August-September 2006, pp. 823–828.

O. Bebek and M. C. Cavusoglu, "Whisker sensor design for three dimensional position measurement in robotic assisted beating heart surgery," in *Proc. of the International Conference on Robotics and Automation (ICRA)*, Rome, Italy, April 2007, pp. 225–231.

T. Franke, O. Bebek, and M. C. Cavusoglu, "Improved prediction of heart motion using an adaptive filter for robot assisted beating heart surgery," in *Proc. of the International Conference on Intelligent Robots and Systems (IROS)*, San Diego, CA, USA, October-November 2007, pp. 509–515.

T. Franke, O. Bebek, and M. C. Cavusoglu, "Prediction of heartbeat motion with a generalized adaptive filter," to appear in *Proc. of the International Conference on Robotics and Automation (ICRA)*, Pasadena, CA, USA, May 2008.

Bibliography

[1] "Deaths: Preliminary data for 2004," Centers for Disease Control and Prevention, 2006. [Online]. Available: http://www.cdc.gov/nchs/fastats/heart.htm

[2] M. F. Newman, J. L. Kirchner, B. Phillips-Bute, V. Gaver, H. Grocott, R. H. Jones, *et al.*, "Longitudinal assessment of neurocognitive function after coronary-artery bypass surgery," *New England Journal of Medicine*, vol. 344, no. 6, pp. 395–402, February 2001.

[3] J. D. Puskas, C. E. Wright, R. S. Ronson, W. M. Brown, J. P. Gott, and R. A. Guyton, "Off-pump multi-vessel coronary bypass via sternotomy is safe and effective," *Annals of Thoracic Surgery*, vol. 66, no. 3, pp. 1068–1072, September 1998.

[4] M. Mark B. Ratcliffe, *Personal Communication*, Chief of Surgery, San Francisco VA Medical Center, Professor in Residence.

[5] V. Falk, "Manual control and tracking-a human factor analysis relevant for beating heart surgery," *Annals of Thoracic Surgery*, vol. 74, pp. 624–628, 2002.

[6] "National Heart, Lung and Blood Institute (NHLBI)," National Institutes of Health, 2007. [Online]. Available: http://www.nhlbi.nih.gov/health/dci/Diseases/Cad/

[7] "Heart disease and stroke statistics-2007 Update at-a-Glance," American Heart Association, 2007.

[8] P. J. Hecht, "Coronary artery bypass surgery-Image ID: 657B," Office of NIH History, Historical Resources Image Collections, National Institutes of Health, 1981. [Online]. Available: http://fmp.cit.nih.gov/hi/hipics/pics/657B-PH.jpg

[9] J. K. Kirklin, "Prospects for understanding and eliminating the deleterious effects of cardiopulmonary bypass," *The Annals of Thoracic Surgery*, vol. 51, no. 4, pp. 529–531, July 1991.

[10] "American Heart Association," 2007. [Online]. Available: http://www.americanheart.org

[11] M. Lemma, A. Mangini, A. Redaelli, and F. Acocella, "Do cardiac stabilizers really stabilize? experimental quantitative analysis of mechanical stabilization," *Interactive CardioVascular and Thoracic Surgery*, no. 4, pp. 222–226, March 2005.

[12] K. Sharma, W. S. Newman, M. Weinhous, G. Glosser, and R. Macklis, "Experimental evaluation of a robotic image-directed radiation therapy system," in *Proc. of IEEE International Conference on Robotics and Automation (ICRA)*, vol. 3, San Francisco, CA, USA, April 2000, pp. 2913–2918.

[13] A. Schweikard, G. Glosser, M. Bodduluri, M. Murphy, and J. Adler, "Robotic motion compensation for respiratory movement during radiosurgery," *Computer Aided Surgery*, vol. 5, no. 4, pp. 263–77, 2000.

[14] C. Riviere, A. Thakral, I. I. Iordachita, G. Mitroi, and D. Stoianovici, "Predicting respiratory motion for active canceling during percutaneous needle insertion," in *Proc. of the 23rd Annual International Conference of the IEEE Engineering in Medicine and Biology Society (EMBC)*, Istanbul, Turkey, October 2001, pp. 3477–3480.

[15] A. L. Trejos, S. E. Salcudean, F. Sassani, and S. Lichtenstein, "On the feasibility of a moving support for surgery on the beating heart," in *Proc. of Medical Image Computing and Computer-Assisted Interventions (MICCAI)*, Cambridge, UK, September 1999, pp. 1088–1097.

[16] A. J. Madhani, G. Niemeyer, and J. K. Salisbury, "The black falcon: a teleoperated surgical instrument for minimally invasive surgery," in *Proc. of the IEEE/RSJ International Conference on Intelligent Robots and Systems (IROS)*, vol. 2, Victoria, BC, Canada, October 1998, pp. 936–944.

[17] T. J. Gilhuly, S. E. Salcudean, and S. V. Lichtenstein, "Evaluating optical stabilization of the beating heart," *IEEE Engineering in Medicine and Biology Magazine*, vol. 22, no. 4, pp. 133–140, July-August 2003.

[18] Y. Nakamura, K. Kishi, and H. Kawakami, "Heartbeat synchronization for robotic cardiac surgery," in *Proc. of IEEE International Conference on Robotics and Automation (ICRA)*, vol. 2, Seoul, Korea, May 2001, pp. 2014–2019.

[19] A. Thakral, J. Wallace, D. Tomlin, N. Seth, and N. V. Thakor, "Surgical motion adaptive robotic technology (S.M.A.R.T.): Taking the motion out of physiological motion," in *Proc. of 4th International Conference on Medical Image Computing and Computer-Assisted Intervention (MICCAI)*, Utrecht, The Netherlands, October 2001, pp. 317–325.

[20] M. Groeger, T. Ortmaier, W. Sepp, and G. Hirzinger, "Tracking local motion on the beating heart," in *Proc. of the SPIE Medical Imaging Conference*, vol. 4681 of SPIE, San Diego, CA, USA, February 2002, pp. 233–241.

[21] M. L. Koransky, M. L. Tavana, A. Yamaguchi, and R. Robbins, "Quantification of mechanical stabilization for the performance of offpump coronary artery surgery," in *Proc. of the Meeting of the International Society for Minimally Invasive Cardiac Surgery (ISMICS)*, Munich, Germany, June 2001, (Abstract).

[22] T. Ortmaier, "Motion compensation in minimally invasive robotic surgery," Doctoral Thesis, Technical University of Munich, Germany, April 2003.

[23] T. Ortmaier, M. Groeger, D. H. Boehm, V. Falk, and G. Hirzinger, "Motion estimation in beating heart surgery," *IEEE Transactions on Biomedical Engineering*, vol. 52, no. 10, pp. 1729–1740, October 2005.

[24] R. Ginhoux, J. A. Gangloff, M. F. DeMathelin, L. Soler, J. Leroy, M. M. A. Sanchez, and J. Marescaux, "Active filtering of physiological motion in robotized surgery using predictive control," *IEEE Transactions on Robotics*, vol. 21, no. 1, pp. 67–79, February 2005.

[25] J. Rotella, "Predictive tracking of quasi periodic signals for active relative motion cancellation in robotic assisted coronary artery bypass graft surgery," M.S. Thesis, Case Western Reserve University, Cleveland, OH, USA, August 2004.

[26] L. Cuvillon, J. Gangloff, M. DeMathelin, and A. Forgione, "Toward robotized beating heart TECABG: Assessment of the heart dynamics using high-speed vision," in *Proc. of Medical Image Computing and Computer-Assisted Intervention (MICCAI)*, vol. 2, Palm Springs, USA, October 2005, pp. 551–558.

[27] V. Duindam and S. Sastry, "Geometric motion estimation and control for robotic-assisted beating-heart surgery," in *Proc. of IEEE/RSJ International Conference on Intelligent Robots and Systems (IROS)*, San Diego, CA, USA, October-November 2007, pp. 871–876.

[28] M. B. Ratcliffe, K. B. Gupta, J. T. Streicher, E. B. Savage, D. K. Bogen, and J. L. H. Edmunds, "Use of sonomicrometry and multidimensional scaling to determine the three-dimensional coordinates of multiple cardiac locations: Feasibility and initial implementation," *IEEE Transactions on Biomedical Engineering*, vol. 42, no. 6, pp. 587–598, June 1995.

[29] *Digital Ultrasonic Measurement System Hardware Manual*, 6th ed., Sonometrics Corporation, Ontario, Canada.

[30] G. Kalogeros, *Personal Communication*, Sonometrics Corporation, Ontario, Canada.

[31] C. E. Garcia, D. M. Prett, and M. Morari, "Model predictive control: Theory and practice-a survey," *Automatica*, vol. 25, no. 3, pp. 335–348, 1989.

[32] E. Camacho and C. Bordons, *Model Predictive Control.* Springer, 1999.

[33] B. D. Anderson and J. B. Moore, *Optimal Control Linear Quadratic Methods*. Prentice Hall, 1990.

[34] J. Malmivuo and R. Plonsey, *Bioelectromagnetism - Principles and Applications of Bioelectric and Biomagnetic Fields*. Oxford University Press, New York, 1995.

[35] R. M. Berne and M. N. Levy, *Cardiovascular Physiology*, 8th ed. St. Louis: Mosby Inc, 2001.

[36] R. M. Berne and M. N. Levy, *Principles of Physiology*, 3rd ed. St. Louis: Mosby Inc, 2000.

[37] R. Poli, S. Cagnoni, and G. Valli, "Generic design of optimum linear and non-linear QRS detection," *IEEE Transactions on Biomedical Engineering*, vol. 42, no. 11, pp. 1137–1141, November 1995.

[38] V. X. Afonso, W. J. Tompkins, T. Q. Nguyen, and S. Luo, "ECG beat detection using filter banks," *IEEE Transactions on Biomedical Engineering*, vol. 46, no. 2, pp. 192–201, 1999.

[39] I. Dotsinsky and T. Stoyanov, "Ventricular beat detection in single channel electrocardiograms," *BioMedical Engineering OnLine*, vol. 3, no. 3, 2004.

[40] C. Li, C. Zheng, and C. Tai, "Detection of ECG characteristic points using wavelet transforms," *IEEE Transactions on Biomedical Engineering*, vol. 42, pp. 21–28, 1995.

[41] I. Chirstov, "Real time electrocardiogram QRS detection using combined adaptive threshold," *BioMedical Engineering OnLine*, vol. 3, no. 28, 2004.

[42] M. Bahoura, M. Hassani, and M. Hubin, "DSP implementation of wavelet transform for real wave forms detection and heart rate analysis," *Computer Methods & Programs in Biomedicine*, vol. 52, pp. 35–44, 1997.

[43] *MIT-BIH Arrhythmia Database*, PhysioNet, 1980. [Online]. Available: http://www.physionet.org/physiobank/database/mitdb/

[44] M. G. Safonov and R. Y. Chiang, "A Schur method for balanced-truncation model reduction," *IEEE Transactions on Automatic Control*, vol. 34, no. 7, pp. 729–733, July 1989.

[45] M. C. Cavusoglu, D. Feygin, and F. Tendik, "A critical study of the mechanical and electrical properties of the PHANToM haptic interface and improvement for high performance control," *Presence*, vol. 11, no. 6, pp. 555–568, 2002.

[46] G. Shechter, J. R. Resar, and E. R. McVeigh, "Displacement and velocity of the coronary arteries: Cardiac and respiratory motion," *IEEE Transactions on Medical Imaging*, vol. 25, no. 3, pp. 369–375, March 2006.

[47] B. Cagneau, N. Zemiti, D. Bellot, and G. Morel, "Physiological motion compensation in robotized surgery using force feedback control," in *Proc. of the International Conference on Robotics and Automation (ICRA)*, Rome, Italy, April 2007, pp. 1881–1886.

[48] C. Riviere, J. Gangloff, and M. de Mathelin, "Robotic compensation of biological motion of enhance surgical accuracy," *Proceedings of the IEEE*, vol. 94, no. 9, pp. 1705–1716, September 2006.

[49] L. Hoff, O. J. Elle, M. J. Grimnes, S. Halvorsen, H. J. Alker, and E. Fosse, "Measurements of heart motion using accelerometers," in *Proc. of the Annual International Conference of the Engineering in Medicine and Biology Society (EMBC)*, vol. 3, San Francisco, CA, USA, September 2004, pp. 2049–2051.

[50] M. C. Cavusoglu, J. Rotella, W. S. Newman, S. Choi, J. Ustin, and S. S. Sastry, "Control algorithms for active relative motion cancelling for robotic assisted off-pump coronary artery bypass graft surgery," in *Proc. of the 12th International Conference on Advanced Robotics (ICAR)*, Seattle, WA, USA, July 2005, pp. 431–436.

[51] M.-A. Vitrani, H. Mitterhofer, G. Morel, and N. Bonnet, "Robust ultrasound-based visual servoing for beating heart intracardiac surgery," in *Proc. of the International Conference on Robotics and Automation (ICRA)*, Rome, Italy, April 2007, pp. 3021–3027.

[52] T. Bader, A. Wiedemann, K. Roberts, and U. D. Hanebeck, "Model-based motion estimation of elastic surfaces for minimally invasive cardiac surgery," in *Proc. of the International Conference on Robotics and Automation (ICRA)*, Rome, Italy, April 2007, pp. 2261–2266.

[53] A. Noce, J. Triboulet, and P. Poignet, "Efficient tracking of the heart using texture," in *Proc. of the Annual International Conference of the Engineering in Medicine and Biology Society (EMBC)*, Lyon, France, August 2007, pp. 4480–4483.

[54] N. Zemiti, G. Morel, T. Ortmaier, and N. Bonnet, "Mechatronic design of a new robot for force control in minimally invasive surgery," *IEEE/ASME Transactions on Mechatronics*, vol. 12, no. 2, pp. 143–153, April 2007.

[55] P. J. Berkelman, L. L. Whitcomb, R. H. Taylor, and P. Jensen, "A miniature microsurgical instrument tip force sensor for enhanced force feedback during robot-assisted manipulation," *IEEE Transactions on Robotics and Automation*, vol. 19, no. 5, pp. 917–922, October 2003.

[56] G. R. Sholz and C. D. Rahn, "Profile sensing with an actuated whisker," *IEEE Transactions on Robotics and Automation*, vol. 20, no. 1, pp. 124–127, February 2004.

[57] J. H. Solomon and M. J. Hartmann, "Biomechanics: Robotic whiskers used to sense features," *Nature*, vol. 443, no. 7111, p. 525, October 2006.

[58] M. P. Koster, "Flexural joints in mechanisms," in *Proceedings of the ASME Dynamic Systems and Control Division*, vol. 2, 2000, pp. 855–859.

[59] "Surface preparation for strain gage bonding - application note B-129-8," Vishay Micro-Measurements, Tech. Rep. 11129, Feburary 2005. [Online]. Available: http://www.vishay.com/doc?11129

[60] "Strain gage installations with M-bond 43-B, 600, and 610 adhesive systems - instruction bulletin B-130," Vishay Micro-Measurements, Tech. Rep. 11130, April 2007. [Online]. Available: http://www.vishay.com/doc?11130

[61] "Strain gauge measurement - a tutorial," National Instruments, Tech. Rep. 078, August 1998.

[62] W. F. Riley, L. D. Sturges, and D. H. Morris, *Mechanics of Materials*, 5th ed. New York, USA: John Wiley & Sons Inc., 1999.

[63] *Nano17, 6-axis Force/Torque Sensor*, ATI Industiral Automation, 2008. [Online]. Available: http://www.ati-ia.com/products/ft/ft_models.aspx?id=Nano17

[64] Y. Nakamura and Y. Zu, "Geometrical fusion method for multi-sensor robotic systems," in *Proc. of the IEEE International Conference on Robotics and Automation (ICRA)*, Scottsdale, Arizona, May 1989, pp. 668–673.

[65] *GP-KX121 Series Color Board Camera Data Sheet*, Distributed by Panasonic, Japan, OEM Product/NTSC.

[66] J. K. Kim, M. C. Lee, C. K. Ahn, and C. Y. Kim, "Acquisition of 3-D information using stereo vision system by relative stereo disparity with subpixel resolution," in *Proc. of the IEEE International Symposium on Industrial Electronics*, Pusan, Korea, June 2001, pp. 1671–1676.

[67] *Laser triangulation position sensors-RF60X Series*, RIFTEK, 2008. [Online]. Available: http://www.riftek.com/resource/download/rf603_riftek_eng.pdf

[68] "Three axis, 2.5-10 g low-g micromachined accelerometer," Freescale Semiconductor, Tech. Rep. MMA7261QT, September 2007. [Online]. Available: http://www.freescale.com/files/sensors/doc/data_sheet/MMA7261QT.pdf

[69] G. F. Frankln, J. D. Powell, and M. Workman, *Digital Control of Dynamic Systems*, 3rd ed. Addison Wesley Longman, 1998.